

CHAOS. VI. Direct Abundances in NGC 2403

Noah S. J. Rogers¹ , Evan D. Skillman¹ , Richard W. Pogge^{2,3} , Danielle A. Berg⁴ , John Moustakas⁵ , Kevin V. Croxall⁶ , and Jiayi Sun² 

¹ Minnesota Institute for Astrophysics, University of Minnesota, 116 Church Street SE, Minneapolis, MN 55455, USA; roge0291@umn.edu

² Department of Astronomy, The Ohio State University, 140 W 18th Avenue, Columbus, OH 43210, USA

³ Center for Cosmology & AstroParticle Physics, The Ohio State University, 191 West Woodruff Avenue, Columbus, OH 43210, USA

⁴ Department of Astronomy, University of Texas at Austin, 2515 Speedway, Austin, TX 78712, USA

⁵ Department of Physics & Astronomy, Siena College, 515 Loudon Road, Loudonville, NY 12211, USA

⁶ Expedt Software, 100 W Old Wilson Bridge Road, Suite 216, Worthington, OH 43085, USA

Received 2020 September 25; revised 2021 March 29; accepted 2021 April 7; published 2021 June 29

Abstract

We report the direct abundances for the galaxy NGC 2403 as observed by the CHemical Abundances Of Spirals (CHAOS) project. Using the Multi-Object Double Spectrograph on the Large Binocular Telescope, we observe two fields with H II regions that cover an R_g/R_e range of 0.18–2.31. Thirty-two H II regions contain at least one auroral line detection, and we detect a total of 122 temperature-sensitive auroral lines. Here, for the first time, we use the intrinsic scatter in the T_e – T_e diagrams, added in quadrature to the uncertainty on the measured temperature, to determine the uncertainty on an electron temperature inferred for one ionization zone from a measurement in a different ionization zone. We then use all available temperature data within a H II region to obtain a weighted-average temperature within each ionization zone. We rederive the oxygen abundances of all CHAOS galaxies using this new temperature prioritization method, and we find that the gradients are consistent with the results of a recent study of Berg et al. For NGC 2403, we measure a direct oxygen abundance gradient of $-0.09(\pm 0.03)$ dex/ R_e , with an intrinsic dispersion of $0.037(\pm 0.017)$ dex and a N/O abundance gradient of $-0.17(\pm 0.03)$ dex/ R_e with an intrinsic dispersion of $0.060(\pm 0.018)$ dex. For direct comparison, we use the line intensities from an earlier study of NGC 2403 by Berg et al. and find their recomputed values for the O/H and N/O gradients are consistent with ours.

Unified Astronomy Thesaurus concepts: Chemical abundances (224); Spiral galaxies (1560); Galaxy evolution (594); Interstellar medium (847); H II regions (694)

Supporting material: machine-readable table

1. Introduction

Stellar nucleosynthesis enriches star-forming galaxies with heavy elements, which are incorporated into the next generation of stars. Mapping the distribution of chemical abundances in galaxies gives insight into their stellar and chemical evolution, the yields of stellar nucleosynthesis, and the underlying physics of the interstellar medium (ISM). Beyond their use in individual galaxies, abundances are crucial for studies of the mass–metallicity relation (MZR) for galaxies (e.g., Lequeux et al. 1979; Tremonti et al. 2004) and as input parameters for other galaxy-related studies and models, like those concerning the CO-to-H₂ conversion factor (Sandstrom et al. 2013).

Optical emission lines from H II regions are the primary mechanism for obtaining chemical abundances in nearby spiral galaxies. At the typical temperature of a H II region (on the order of 10⁴ K), the dominant cooling mechanism is the emission from collisionally excited lines in metal ions like O⁺, O²⁺, N⁺, S⁺, and S²⁺. Free electrons excite the outer electrons in these metal ions via collisions. The subsequent radiative de-excitations produce photons that will escape the region without exciting a similar energy level due to the scarcity of these metals relative to H⁺. The ratios of specific forbidden line fluxes from these photons are used to directly calculate the electron temperatures and/or densities within the region. The temperatures and densities are used to calculate the emissivities of various transitions, which are applied in conjunction with the corresponding line fluxes to obtain the relative ionic abundances.

The auroral lines needed for this abundance technique, called the “direct” abundance determination (Dinerstein 1990), are faint, especially in regions of high metallicity/low temperature where emission from collisionally excited fine-structure lines in the IR dominate the cooling. The intrinsic faintness of auroral lines has resulted in a lack of detections and, subsequently, in direct abundance studies with a relatively small number of H II regions (e.g., Berg et al. 2013 and references therein). Other abundance studies have developed calibrators relating the flux of the strongest emission lines to the chemical abundances within a H II region (Pagel et al. 1979; McGaugh 1991; Kobulnicky et al. 1999; Kewley & Dopita 2002; Pettini & Pagel 2004; Bresolin 2007; Marino et al. 2013; Pilyugin & Grebel 2016, and others). However, comparing strong-line calibrators of different origin reveals differences in the inferred abundances. Empirical and theoretical strong-line abundances for the same galaxy produce discrepancies (sometimes sizable, ~ 0.7 dex at the extremes) in abundances, gradients, and dispersions (Kewley & Ellison 2008; Moustakas et al. 2010). Nearby galaxies present the best chance of observing the faint, temperature-sensitive auroral lines necessary for direct abundances. Increasing the sample of direct abundance measurements is necessary to move away from the use of strong-line calibrators in these galaxies, to create more statistically significant direct abundance studies, and to better calibrate empirical strong-line diagnostics for use in more distant galaxies.

Another method to obtain direct abundances involves stacking the spectra of many galaxies of similar stellar mass

(Liang et al. 2007), stellar mass and star formation rate (Andrews & Martini 2013; Brown et al. 2016), or [O II] and [O III] nebular line flux (Curti et al. 2017). The assumption in doing so is that galaxies of similar stellar mass have similar metallicities via the MZR or that galaxies containing similar strong-line emission have comparable O/H abundance. Given the faintness of the auroral lines and the difficulty of observing them at high redshift, stacking spectra allows for increased detections where traditional, single-object spectroscopy may otherwise fail to obtain a direct temperature. This is especially useful for establishing electron temperature trends (Andrews & Martini 2013) and for developing strong-line calibrators (Curti et al. 2017) using a statistically significant sample of galaxies.

Alternatively, Integral Field Unit (IFU) surveys observe the entire disk of a galaxy with many optical fibers. These surveys trade the high sensitivity needed to observe the temperature-sensitive auroral lines for complete spectral coverage of the galaxy. The result is strong-line detections in hundreds or thousands of pixels across the disk of the galaxy, allowing for statistically significant strong-line abundance analyses for many galaxies. For example, the CALIFA and VLT/MUSE IFU surveys have identified a universal oxygen abundance gradient for 306 and 102 low-redshift galaxies, respectively (Sánchez et al. 2014; Sánchez-Menguiano et al. 2018). A spaxel-by-spaxel analysis for 122 galaxies in the CALIFA sample confirms this finding, although the universal gradient is slightly shallower (Sánchez-Menguiano et al. 2016). Additionally, Ho et al. (2019) detected the [N II] $\lambda 5755$ auroral line in 80 H II regions in NGC 1672 using VLT/MUSE, allowing for direct abundance determination in this galaxy. However, the wavelength coverage of IFU surveys often excludes some auroral or nebular emission lines that may be useful in determining temperatures of different ionization zones and direct abundances of different ionic species.

The CHemical Abundance Of Spirals (CHAOS) project has acquired high-resolution observations of H II regions in nearby, face-on spiral galaxies from the Spitzer Infrared Nearby Galaxies Survey (Kennicutt et al. 2003a) to increase the number of temperature-sensitive auroral line detections for use in abundance determinations. For a more detailed description of the CHAOS sample, see Berg et al. (2015). The CHAOS auroral and nebular line observations allow for temperature and abundance determination from multiple ions spanning a wide range of ionization. For example, Berg et al. (2020) used the 180+ H II regions with two or more auroral line detections to find new T_e - T_e relations, a possible explanation for the large intrinsic scatter within some direct abundance gradients, and the presence of a universal N/O gradient at $R_g/R_e < 2.0$. CHAOS has also detected a number of C II recombination lines, resulting in a C/H abundance gradient for NGC 5457 (Skillman et al. 2020). The CHAOS sample, once fully analyzed, can be used to find global trends in the direct abundances of nearby spiral galaxies, derive new ionization correction factors (ICFs) for unobserved ions within H II regions, study the discrepancy between direct and recombination line abundances, and to further address how the scatter in direct abundances is related to the physical processes of the ISM.

Using its large sample of direct abundances from H II regions, the CHAOS project has found significant variations

among the intrinsic dispersions about the galactic oxygen abundance gradients. The magnitude of the dispersion in $\log(O/H)$ can be on the order of 0.1 dex, similar to the scatter Rosolowsky & Simon (2008) observed in the M33 H II regions when using the direct abundance method. Abundance dispersions, or lack thereof, are related to the physical processes within the ISM such as radial mixing, gas infall, or star formation (Roy & Kunth 1995). Thus far, no uniform, statistically significant data set of direct abundances in multiple galaxies has been capable of studying the abundance dispersions and how these are related to ISM properties, location within the spiral galaxy, or galactic properties. IFU studies have detected abundance enhancements in spiral-arm H II regions relative to interarm regions (Ho et al. 2019; Sánchez-Menguiano et al. 2020), though the magnitude of these variations is not well established (see Kreckel et al. 2019). The strong-line methods are used to measure these variations, and these methods produce smaller variations in oxygen abundance relative to the direct method (Arellano-Córdova et al. 2016). CHAOS targets H II regions spanning the disk of each observed galaxy and can detect multiple temperature-sensitive auroral lines within a given region. This combination makes the total CHAOS database optimal for a study of the direct abundance dispersion in spiral galaxies.

NGC 2403 is a nearby (adopted distance of 3.18 Mpc from Tully et al. 2013), intermediate spiral galaxy (SABcd) with an R_{25} of 10.95' and inclination of 63° (de Blok et al. 2008). This galaxy has been the focus of multiple abundance studies, but these studies have used the spectra from a relatively small number of H II regions. For example, Garnett et al. (1997) reported a direct abundance gradient in NGC 2403 using the optical spectra of 12 H II regions, while Berg et al. (2013) used the optical spectra of 7 H II regions to measure the abundance gradient. Recently, Mao et al. (2018) conducted a spectroscopic study on 11 spatially resolved H II regions in NGC 2403. They used commonly employed strong-line abundance calibrators to check for variations of the inferred abundances as a function of nebular radius. Absolute abundance discrepancies, in addition to different radial/ionization dependences, are found between different strong-line calibrators. Additionally, blue supergiant spectra have been acquired in NGC 2403 (F. Bresolin 2020, private communication). These spectra allow for a completely independent measure of the abundances in the galaxy.

Here, we present the results of the CHAOS observations of NGC 2403, including the chemical abundances, gradients, and dispersions within the galaxy as found from the H II regions with detected temperature-sensitive auroral lines. The remainder of this paper is organized as follows: observations and data reduction are reported in Section 2; Section 3 highlights the electron temperature relations found in five CHAOS galaxies and presents a new technique to better estimate temperature uncertainties when applying empirical T_e - T_e relations; in Section 4 we describe how the abundances of each ionic species are determined; in Section 5 we report the direct abundances observed in NGC 2403, compare these to updated literature values, and examine the abundances in the previous four CHAOS galaxies; Section 6 details the α -element abundance trends found in the present sample of H II regions; and we summarize our findings in Section 7.

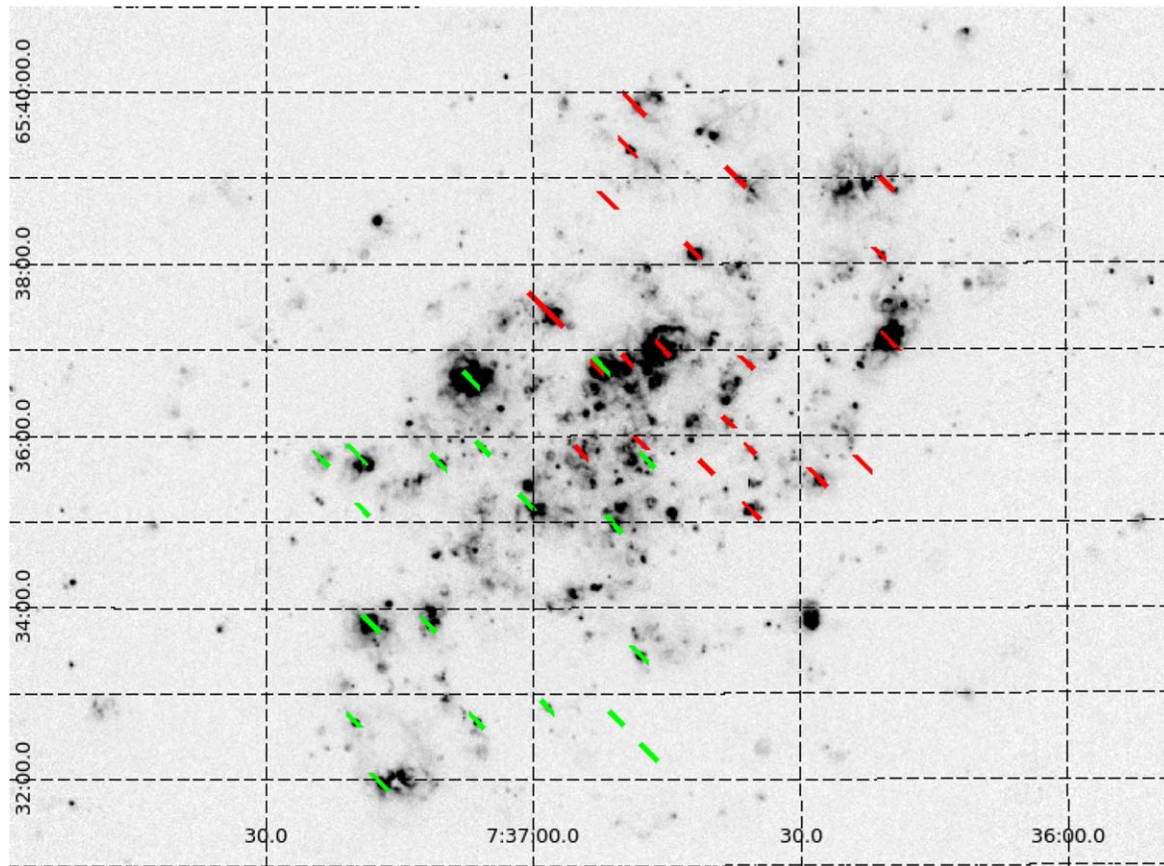


Figure 1. Map of the slits used to observe the H II regions in NGC 2403 overlaid on a continuum-subtracted H α image (obtained from <http://sumac.astro.indiana.edu/~vanzee/LVL/NGC2403/>). The axes are in degrees: R.A. on the x -axis and decl. on the y -axis. The slits are color-coded by observation field: green for Field 1, red for Field 2.

2. NGC 2403 Observations and Data Reduction

2.1. Data Acquisition

The Multi-Object Double Spectrograph (MODS; Pogge et al. 2010) on the Large Binocular Telescope (LBT; Hill 2010) is used to observe two fields of NGC 2403. Custom laser-cut slit masks allow for the concurrent observation of ~ 20 objects per field, which takes advantage of multiplexing and makes the data less susceptible to nightly differences in atmospheric variations. MODS uses the G400L grating (400 lines mm $^{-1}$; $R \approx 1850$) for the blue and the G670L grating (250 lines mm $^{-1}$; $R \approx 2300$) for the red to cover a wavelength range of 3200–10000 Å, appropriate for the optical auroral lines necessary for temperature, density, and abundance determination. The slits are cut to be 1" in width and can range from 10" to 32" in length. The field of view of MODS is 6' \times 6', roughly half the R_{25} of NGC 2403 but large enough to achieve coverage of the disk H II regions in two fields. The resolution of MODS allows for auroral line detections even for lines that are near other nebular emission lines (for instance, [S III] $\lambda 6312$ and [O I] $\lambda 6300$). As a result, MODS and the LBT are optimized for optical direct abundance studies of nearby spiral galaxies.

The first and second fields were observed on 2017 November 16 and 2018 February 8, respectively. Both fields were simultaneously observed in the blue (3200–5800 Å) and red (5500–10000 Å) with MODS1, the detector on the LBT SX telescope. The seeing during the nights of observation range

from 1.0" to 1.3". The fields were observed for six exposures of 1200 s each, at an air mass between 1.2 and 1.4, and at a position angle near the parallactic angle halfway through observation. Observing at low air mass and an optimal parallactic angle, we ensure minimal loss of intensity at the ends of the observed spectrum due to differential atmospheric refraction (Filippenko 1982).

Slits are cut to target bright H II regions spanning the disk of the galaxy. The slit locations are shown in Figure 1, superimposed on a continuum-subtracted H α image of NGC 2403⁷ and color-coded by field. The targeted H II regions range in R_g/R_e from 0.18 to 2.31, sufficient to examine the radial dependence of the chemical abundances. In this paper, the IDs of the targets are provided in terms of the R.A. and decl. offsets of their surface brightness peaks relative to the center of NGC 2403, as given in Table 1. Table 2 provides the radial locations of, and the auroral lines detected in, each of the 33 H II regions targeted. Additionally, the last column of Table 2 notes the presence of Wolf-Rayet (WR) features in the optical spectra. WR stars are high-mass stars with strong stellar winds and are characterized, spectrally, by broadened emission features from He II, C III, C IV, and N III (López-Sánchez & Esteban 2010). These features are typically blended together at ~ 4600 –4700 Å (the blue WR bump) and ~ 5750 –5870 Å (the red WR bump). The blue WR bump is the most common WR

⁷ From Liese van Zee, <http://sumac.astro.indiana.edu/~vanzee/LVL/NGC2403/>.

Table 1
Adopted Properties of NGC 2403

Property	Adopted Value	Reference
R.A.	07 ^h 36 ^m 51.4 ^s	(1)
Decl.	+65°36'09.2"	(1)
Inclination	63°	(2)
Position angle	124°	(2)
Distance	3.18 ± 0.12 Mpc	(3)
$\log(M_*/M_\odot)$	9.57	(4)
R_{25}	10.95'	(5)
R_e	178.0" ± 5"	(6)
Redshift	0.000445	(1)

Note. Units of R.A. are hours, minutes, and seconds, and units of decl. are degrees, arcminutes, and arcseconds.

References. (1) 2MASS Extended Objects Final Release, (2) de Blok et al. (2008), (3) Tully et al. (2013), (4) Leroy et al. (2019), (5) Kendall et al. (2011), (6) the effective radius is calculated in the manner described in Appendix C of Berg et al. (2020).

feature observed in the H II regions of NGC 2403, and a blue WR feature always accompanies a red WR feature when the latter is observed in a H II region (eight objects total). Table 2 also provides the regions which contain C II λ 4267 Å detections. This recombination line allows for the determination of C⁺⁺ abundances (for example, Esteban et al. 2009, 2020; Skillman et al. 2020), but we reserve an analysis of the recombination line abundances in multiple galaxies for a future study.

2.2. MODS Data Reduction and Line Modeling

We highlight the key steps of the CHAOS project’s data reduction pipeline⁸ briefly. For a complete explanation of the MODS data reduction pipeline, the reader is referred to Berg et al. (2015). The `modCCDRed` PYTHON programs are used to bias subtract and flat-field the raw CCD images of the science targets, standard stars, and calibration lamps. The resulting images are used in the current version of the `modIDL` reduction pipeline, which runs in the XIDL reduction package.⁹ Sky subtraction and region extraction are performed on each slit, and calibration lamp data provide a wavelength calibration for the resulting 1D spectrum. Standard stars are used for flux calibration and correction for atmospheric extinction (Bohlin et al. 2014). There are three sky-only slits (skylslits) in each of the field masks (see Figure 1). In some slits, selecting a region for sky subtraction is not possible without additionally removing a substantial amount of flux from the H II region. This is the case for H II regions larger than the length of the slit, such as the large regions NGC 2403+38+51, NGC 2403+7+37, and NGC 2403+96+30. For slits where local sky is unobtainable, the fitted sky spectrum from one of these skylslits, or a neighboring slit with ample sky, is used for sky subtraction. Figure 2 shows an example of a 1D, flux- and wavelength-calibrated spectrum from one of the H II regions (NGC 2403+44+82) containing five auroral line detections.

⁸ The MODS reduction pipeline was developed by Kevin Croxall with funding from NSF Grant AST-1108693. Details at <http://www.astronomy.ohio-state.edu/MODS/Software/modIDL/>.

⁹ <http://www.ucolick.org/~xavier/IDL/>

The spectrum of a H II region contains the underlying stellar continuum from the stars ionizing the region. The STARLIGHTv04¹⁰ spectral synthesis code (Cid Fernandes et al. 2005) is used in conjunction with the stellar population models of Bruzual & Charlot (2003) to model the stellar continuum. We do not constrain the metallicity of the input stellar models because the shape of the stellar continuum is only used for the continuum component of the line-fitting code. We do not use the modeled underlying absorption features for reddening corrections (see Section 2.3). After subtracting the stellar continuum from the spectrum, each emission line is fit with a Gaussian profile while allowing for an additional nebular continuum component. The Gaussian fits work well for most lines, including the auroral lines needed to determine the electron temperatures and densities.

As discussed in Berg et al. (2020), the [O II] $\lambda\lambda$ 3726, 3729 doublet, a density-dependent set of emission lines, is blended at the resolution of MODS (see Figure 2). We use the FWHM of the neighboring lines and the wavelength separation of the two transitions to simultaneously fit the two lines. The total flux in the doublet is reported as the flux of “[O II] λ 3727.” Additionally, [Fe II] λ 4360 can contaminate [O III] λ 4363 at high metallicities ($12 + \log(\text{O/H}) \geq 8.3$) where this line may otherwise be weak or undetected (Curti et al. 2017). If [Fe II] λ 4360 is misinterpreted as a detection of [O III] λ 4363, or if the flux of [Fe II] λ 4360 is blended with the flux of [O III] λ 4363, then temperatures (abundances) derived for that region are biased unphysically high (low). Berg et al. (2020) found evidence for such contamination in a small number of H II regions in the previous CHAOS galaxies. As such, [Fe II] λ 4360 and [O III] λ 4363 are fit simultaneously to avoid contamination.

The MODS spectra have a loss in sensitivity near the dichroic wavelength cutoff at 5700 Å. This can introduce nonphysical features around the wavelength crossover, which makes the stellar continuum difficult to fit properly and can result in missed [N II] λ 5755 detections. To correct for this, the stellar continuum across the dichroic is fit with a low-order polynomial. Then, these features in the blue and red continua are fit with high-order polynomials, taking precaution to avoid any emission lines and WR features. With the continuum and the features modeled by their respective polynomials, the difference between the polynomials is taken and applied to the blue and red spectra. The net result is that the blue and red spectra now match at the dichroic and that the spectra follow the stellar continuum across the dichroic, enabling a better fit for [N II] λ 5755.

Electron temperatures are exponentially sensitive to the auroral-to-nebular line ratios. Therefore, accurate flux measurements, particularly of the weak auroral lines, are essential to the electron temperature determination. While the fitting program used in the MODS data reduction pipeline is able to easily fit the strongest lines, the auroral lines require more care. This is particularly true when night sky lines close to the auroral lines (e.g., Hg I λ 4358 Å) show significant subtraction residuals or if the modeled stellar continuum is not well fit due to differences in the stellar absorption features or other noise structures. Consistent with all CHAOS galaxies, each auroral line is fit by hand and the results compared with those from the MODS data reduction pipeline. In instances where the modeled stellar continuum or night sky noise impacts the line fit from the

¹⁰ www.starlight.ufsc.br

Table 2
NGC 2403 MODS/LBT Observations

H II Region	R.A. (2000)	Decl. (2000)	R_g (arcsec)	$\frac{R_g}{R_e}$	R_g (kpc)	Auroral Line Detections					RLs C II	Wolf Rayet
						[O III]	[N II]	[S III]	[O II]	[S II]		
Total Detections:						18	18	28	32	26	5	13
NGC 2403+19–22	7:36:54.4	65:35:47.24	32.58	0.18	0.50						✓	
NGC 2403–23–16	7:36:47.6	65:35:52.93	59.03	0.33	0.91							
NGC 2403–14+42	7:36:49.2	65:36:51.10	69.18	0.39	1.07		✓	✓	✓	✓	✓	✓
NGC 2403–38+51	7:36:45.2	65:36:59.95	75.43	0.42	1.16	✓	✓	✓	✓	✓	✓	✓
NGC 2403+7+37	7:36:52.6	65:36:45.93	77.57	0.44	1.20	✓	✓	✓	✓	✓	✓	✓
NGC 2403–27–28	7:36:46.9	65:35:41.04	85.37	0.48	1.32			✓	✓	✓		
NGC 2403+56–59	7:37:00.5	65:35:10.39	88.20	0.50	1.36					✓		
NGC 2403+88–18	7:37:05.5	65:35:50.85	111.75	0.63	1.72			✓	✓	✓		✓
NGC 2403–97+39	7:36:35.6	65:36:48.48	113.24	0.64	1.75			✓	✓	✓		
NGC 2403–84–0	7:36:37.8	65:36:09.07	124.50	0.70	1.92			✓	✓	✓		
NGC 2403–3–71	7:36:50.8	65:34:58.60	138.04	0.78	2.12			✓	✓	✓		
NGC 2403+119–28	7:37:10.5	65:35:41.61	148.62	0.83	2.29	✓	✓	✓	✓	✓	✓	✓
NGC 2403–98–19	7:36:35.5	65:35:49.86	171.71	0.96	2.65			✓	✓	✓	✓	
NGC 2403–59+118	7:36:41.8	65:38:07.23	183.34	1.03	2.83	✓	✓	✓	✓	✓	✓	✓
NGC 2403+96+30	7:37:06.8	65:36:39.25	183.51	1.03	2.83	✓	✓	✓	✓	✓	✓	✓
NGC 2403+44+82	7:36:58.5	65:37:31.55	205.28	1.15	3.16	✓	✓	✓	✓	✓	✓	✓
NGC 2403+125–142	7:37:11.6	65:33:46.66	211.84	1.19	3.27	✓		✓	✓	✓	✓	
NGC 2403+166–140	7:37:18.1	65:33:49.15	221.78	1.25	3.42	✓	✓	✓	✓	✓	✓	✓
NGC 2403–190+116	7:36:20.6	65:38:04.55	223.55	1.26	3.45	✓	✓	✓	✓	✓	✓	
NGC 2403+174–24	7:37:19.5	65:35:45.51	233.39	1.31	3.60	✓	✓	✓	✓	✓	✓	
NGC 2403–99–59	7:36:35.4	65:35:09.72	234.98	1.32	3.62	✓	✓	✓	✓	✓	✓	✓
NGC 2403–196+58	7:36:19.7	65:37:07.49	237.12	1.33	3.66	✓	✓	✓	✓	✓	✓	✓
NGC 2403–194+165	7:36:19.9	65:38:53.91	260.70	1.46	4.02			✓	✓	✓		
NGC 2403–89+171	7:36:37.0	65:39:00.61	264.96	1.49	4.08			✓	✓	✓	✓	
NGC 2403–146–38	7:36:27.8	65:35:30.96	268.18	1.51	4.13		✓	✓	✓	✓	✓	✓
NGC 2403+201–24	7:37:23.8	65:35:44.59	271.97	1.53	4.19			✓	✓	✓	✓	
NGC 2403+178–210	7:37:19.9	65:32:38.70	312.22	1.75	4.81	✓		✓	✓	✓	✓	
NGC 2403–22–162	7:36:47.8	65:33:26.94	331.31	1.86	5.11	✓	✓	✓	✓	✓	✓	✓
NGC 2403+92–210	7:37:06.2	65:32:39.11	332.45	1.87	5.13		✓	✓	✓	✓	✓	
NGC 2403+43–200	7:36:58.3	65:32:49.65	344.41	1.93	5.31	✓		✓	✓	✓	✓	
NGC 2403–14+192	7:36:49.1	65:39:21.19	353.85	1.99	5.46	✓	✓	✓	✓	✓	✓	
NGC 2403+160–251	7:37:17.1	65:31:57.98	378.04	2.12	5.83	✓	✓	✓	✓	✓	✓	✓
NGC 2403–18+224	7:36:48.4	65:39:53.26	411.40	2.31	6.34	✓	✓	✓	✓	✓	✓	

Note. H II regions observed in NGC 2403 using MODS on the LBT. The H II region ID, which is the offset in R.A. and decl., in arcseconds, from the central position listed in Table 1, is listed in column 1. The R.A. and decl. of the individual H II regions are given in units of hours, minutes, and seconds, and degrees, arcminutes, and arcseconds, respectively, in columns 2 and 3. Radial distances of the regions are given in columns 4 (in arcseconds), 5 (normalized to R_e), and 6 (in kpc). Columns 7–11 mark the regions that have [O III] λ 4363, [N II] λ 5755, [S III] λ 6312, [O II] $\lambda\lambda$ 7320,7330, and [S II] $\lambda\lambda$ 4068,4076 auroral line detections with S/N > 3. If only one of the [O II] or [S II] lines is detected at S/N > 3 then the region is still marked with a check mark. Column 12 indicates a C II λ 4267 recombination line detection, and column 13 denotes the presence of Wolf-Rayet features in the H II region spectrum.

reduction pipeline, the line fluxes and rms in the continuum are updated to be those of the hand fits. The pipeline fits are used in all other cases to maintain consistency with the fitted strong lines.

Equation (2) from Berg et al. (2013) approximates the uncertainty in the flux of an emission line. This equation is reproduced here:

$$\delta F_\lambda \approx \sqrt{(2 \times \sqrt{n_p} \times RMS)^2 + (0.02 \times F_\lambda)^2}, \quad (1)$$

where n_p is the number of pixels over the FWHM of the line profile, rms is the root mean squared noise in the continuum around the line, and F_λ is the flux of the line. The pixel scale of MODS is 0.5 Å per pixel, so the first term is simplified to $2 \times \sqrt{2 \times \text{FWHM}} \times \text{rms}$. The uncertainty of weak lines is dominated by the rms noise in the continuum about the fit, whereas the uncertainty of the strong lines is dominated by the 2% uncertainty in the flux associated with the flux-calibration

uncertainty when using standard stars (Oke 1990). We consider a line detected if its signal-to-noise ratio (S/N), or $F_\lambda/\delta F_\lambda$, is greater than 3.

2.3. Reddening Corrections

The line-of-sight reddening and the stellar absorption equivalent width are calculated in a manner similar to that described in Olive & Skillman (2001) with a Markov Chain Monte Carlo (MCMC) component introduced by Aver et al. (2011). Recently, Aver et al. (2021) introduced new calibrations using additional hydrogen recombination lines and the BPASS stellar evolution models (Eldridge & Stanway 2009; Eldridge et al. 2017) to obtain the stellar absorption scaling coefficients. The observed hydrogen recombination line fluxes are affected by the underlying stellar absorption, a_H , or the equivalent width of the absorption feature, and reddening, $C(H\beta)$. Given a_H , $C(H\beta)$, and the electron temperature T_e , we

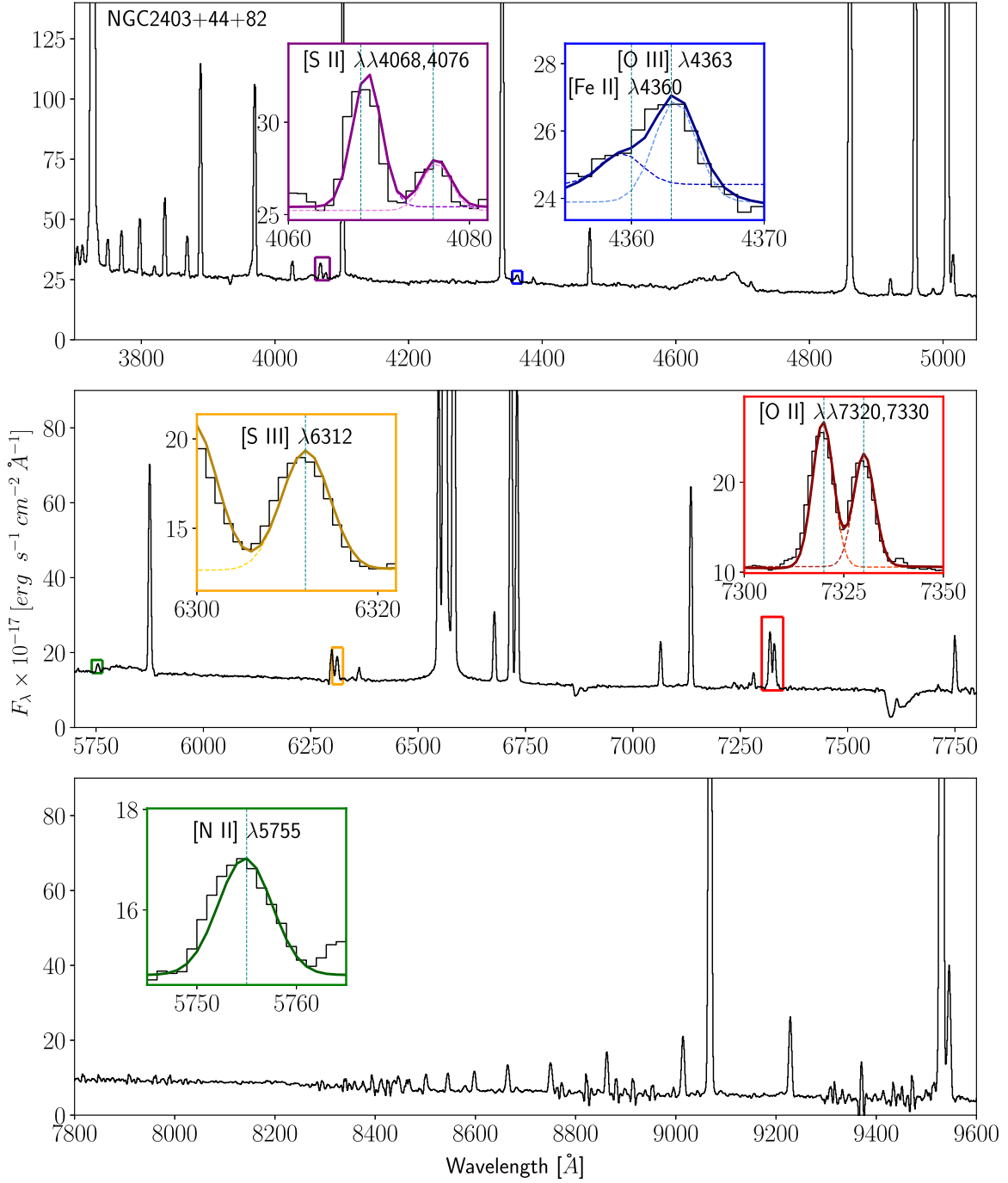


Figure 2. A 1D flux- and wavelength-calibrated spectrum from MODS observations of the region NGC 2403+44+82. Faint, temperature-sensitive auroral lines necessary for direct abundance calculation are magnified in the subplots. The Gaussian fits to the auroral lines and the total fit to the spectra are represented by dashed lines and bold lines, respectively, within each subplot. Additionally, the fit to $[\text{Fe II}] \lambda 4360$ is provided. In this spectrum, the $[\text{S II}] \lambda \lambda 4068, 4076$, $[\text{O III}] \lambda 4363$, $[\text{N II}] \lambda 5755$, $[\text{S III}] \lambda 6312$, and $[\text{O II}] \lambda \lambda 7320, 7330$ lines are all detected at $\text{S/N} \geq 3$. The WR features are also present between 4600 and 4800 Å, and between 5750 and 5900 Å.

calculate theoretical Balmer line fluxes and compare these to the observed Balmer line fluxes. The combination of a_{H} and $C(\text{H}\beta)$ that minimizes the χ^2 function (see Equation (A.2) in Aver et al. 2021) is chosen as the best-fit values. Uncertainties on $C(\text{H}\beta)$ are calculated by fixing a_{H} to the best-fit value and generating a distribution of $C(\text{H}\beta)$ around its best-fit value. Using these inputs, a distribution of theoretical line fluxes is generated and used to repeat the χ^2 minimization. The values of $C(\text{H}\beta)$ at which the χ^2 function equals 1 (the 68% confidence level) are averaged and taken as the uncertainties on

$C(\text{H}\beta)$. The uncertainty on a_{H} is calculated in a similar fashion, except that the lower uncertainty cannot be negative.

This method is similar to the method described in Aver et al. (2011, 2021), except the only parameters that are determined are a_{H} and $C(\text{H}\beta)$. While additional free parameters and high-order hydrogen and helium recombination lines could be considered (see Aver et al. 2021), we use the flux ratios of $\text{H}\alpha/\text{H}\beta$, $\text{H}\gamma/\text{H}\beta$, and $\text{H}\delta/\text{H}\beta$ only. We choose to do this because the Paschen lines can be hard to detect in low surface brightness H II regions or when the sky subtraction is of low

quality. Additionally, the fluxes of high-order Balmer lines above the stellar absorption features are difficult to accurately fit in a consistent and automatic manner. We calculate the electron temperature using the available auroral lines and fix the electron density to $n_e = 10^2 \text{ cm}^{-3}$ instead of leaving these as free parameters.

To implement this method, a linear continuum is fit across the four most intense Balmer lines before stellar continuum subtraction. Although the modeled stellar continuum from STARLIGHT provides a fit to the Balmer absorption features, we leave these as free parameters by fitting a linear continuum around the chosen Balmer lines. The reddening law adopted is from Cardelli et al. (1989) using $A_V = 3.1 \times E(B - V)$, and the electron temperature and density are initially set to $T_e = 10^4 \text{ K}$ and $n_e = 10^2 \text{ cm}^{-3}$, respectively. The theoretical line ratios relative to $\text{H}\beta$ for a given T_e and n_e are calculated using PYNEB (Luridiana et al. 2012, 2015) in conjunction with the recombination line intensities from Storey & Hummer (1995). The χ^2 function is minimized to find the values of a_{H} and $C(\text{H}\beta)$ that best reproduce the observed Balmer line flux ratios. The observed fluxes of the Balmer lines are updated to account for the underlying stellar absorption, adopting the scaling coefficients reported in Aver et al. (2021). The errors on the Balmer lines are updated to account for the error in the flux of the line and the error on a_{H} . The spectrum is then dereddened, and the error in the line flux and error on the reddening correction are combined in quadrature to obtain the reddening-corrected flux error. Electron temperatures are calculated from the available auroral lines in the dereddened spectrum. Using the new electron temperature calculated in the high-ionization zone as the input electron temperature for the theoretical Balmer line calculation, we repeat this process until the change in the electron temperature is $<20 \text{ K}$. If no auroral lines are detected in a H II region, the reddening correction is performed only once at $T_e = 10^4 \text{ K}$.

Table A1 reports the line intensities relative to $\text{H}\beta$ measured from the H II regions in NGC 2403. a_{H} , $C(\text{H}\beta)$, and the flux of $\text{H}\beta$ before accounting for the underlying stellar absorption are also included for each region. The Balmer line intensities typically agree with the expected theoretical ratio within statistical uncertainties, although there is a trend where $I(\text{H}\gamma)/I(\text{H}\beta)$ is systematically greater than the theoretical value. This approach to the reddening correction is unique to NGC 2403 and has not been applied to the previously reported CHAOS galaxies. We intend to update the reddening corrections in those galaxies to be consistent with that of NGC 2403 but doing so here is beyond the scope of this paper.

3. Electron Temperatures

The typical H II region spectrum in NGC 2403 contains multiple temperature-sensitive auroral lines that span the ionization zones of a H II region. The three ratios we use to find the temperatures necessary for abundance analysis are $[\text{N II}]\lambda\lambda 5755/[\text{N II}]\lambda\lambda 6548, 6584$, $[\text{S III}]\lambda\lambda 6312/[\text{S III}]\lambda\lambda 9069, 9532$, and $[\text{O III}]\lambda\lambda 4363/[\text{O III}]\lambda\lambda 4959, 5007$. It is also common to observe the temperature-sensitive lines $[\text{O II}]\lambda\lambda 7320, 7330$ and $[\text{S II}]\lambda\lambda 4069, 4076$ (see Figure 2). However, we currently do not use the $[\text{O II}]$ or $[\text{S II}]$ auroral lines for abundance determination due to the scatter in the measured temperatures from these ions (see discussion in Section 3.2.4 and in Kennicutt et al. 2003b; Croxall et al. 2016; Berg et al. 2020). The strong nebular components of the above ratios are easily detected, although water vapor

absorption features can contaminate the far-red strong lines of $[\text{S III}]$. The ratio of the $[\text{S III}]\lambda 9532$ and $[\text{S III}]\lambda 9069$ emissivities is constant over the range of temperatures and densities typical of a H II region. This ratio is $j_{[\text{S III}]\lambda 9532}/j_{[\text{S III}]\lambda 9069} = 2.47$ as calculated using PYNEB. As such, the ratio of $[\text{S III}]\lambda 9532$ and $[\text{S III}]\lambda 9069$ fluxes is used as a diagnostic to determine if contamination has occurred in the far red. If 2.47 is within the uncertainty of $I([\text{S III}]\lambda 9532)/I([\text{S III}]\lambda 9069)$, then $I([\text{S III}]\lambda 6312)/(I([\text{S III}]\lambda 9532) + I([\text{S III}]\lambda 9069))$ is used to calculate the $[\text{S III}]$ temperature. If the intensity ratio is greater than 2.47, then $I([\text{S III}]\lambda 6312)/(I([\text{S III}]\lambda 9532) \times (1 + 2.47^{-1}))$ is used for $T_e[\text{S III}]$ determination, which corrects for an absorption-contaminated $[\text{S III}]\lambda 9069$ emission line. Similarly, if the intensity ratio is less than the theoretical value, as is the case for a $[\text{S III}]\lambda 9532$ that is too weak, the ratio $I([\text{S III}]\lambda 6312)/(I([\text{S III}]\lambda 9069) \times (1 + 2.47))$ determines $T_e[\text{S III}]$.

PYNEB calculates the best-fit electron temperatures from the measured auroral-to-nebular line flux ratios described above, while the density-sensitive ratio $[\text{S II}]\lambda 6716/[\text{S II}]\lambda 6731$ determines the electron density. The electron density can be used in temperature determinations, but the emissivities of the auroral line transitions are nearly density independent in the low-density limit ($n_e \leq 10^3 \text{ cm}^{-3}$). The low-ionization zone electron temperature (see below) is used for density calculations. All regions in NGC 2403 have densities in the low-density limit, so all temperatures are calculated at $n_e = 10^2 \text{ cm}^{-3}$. MCMC analysis is employed to determine the uncertainty on the electron temperatures: a range of possible flux ratios is generated using the measured flux ratio and its uncertainty, resulting in new temperatures for each generated ratio. The standard deviation of the temperature distribution is taken as the uncertainty on the best-fit temperature. Density uncertainties are calculated in the same manner.

As in previous CHAOS analyses, each H II region is split into three ionization zones. Auroral line emission from particular ions characterizes each zone. For example, emission from $[\text{N II}]\lambda 5755$ originates in the low-ionization zone while $[\text{O III}]\lambda 4363$ is measured in the high-ionization zone. The low-ionization zone temperature is used when calculating the abundances of O^+ , N^+ , and S^+ ; the intermediate-ionization zone temperature is used for the abundances of S^{2+} and Ar^{2+} ; and the high-ionization zone temperature is used for the abundances of O^{2+} and Ne^{2+} .

3.1. T_e – T_e Relation Methods

Ideally, a H II region contains the necessary auroral lines to obtain direct temperatures for each ionization zone. This is not always the case, so T_e – T_e relations are employed to infer the electron temperature in an ionization zone from the direct electron temperature in another zone. Previous studies have determined T_e – T_e relations through photoionization models (Campbell et al. 1986; Garnett 1992; Pagel et al. 1992; Izotov et al. 2006; López-Sánchez et al. 2012, and others), or empirically through auroral line detections in multiple ionization zones (Esteban et al. 2009; Pilyugin et al. 2009; Andrews & Martini 2013; Croxall et al. 2016; Yates et al. 2020; Arellano-Córdova & Rodríguez 2020). CHAOS provides an optimal data set for the latter relations, as the electron temperature data from the numerous spiral galaxies span a large range in T_e parameter space. For example, Croxall et al. (2016) used the 70+ H II regions of NGC 5457 with auroral line detections as a homogeneous data set to develop linear, empirical T_e – T_e relations for $T_e[\text{N II}]$, $T_e[\text{S III}]$, and $T_e[\text{O III}]$ (see their

Equations (5)–(7)). Berg et al. (2020) applied these relations to recalculate the abundances for all the CHAOS galaxies in a uniform manner.

The fit parameters for linear T_e – T_e relations should be invertible such that differences in observational uncertainties associated with obtaining temperatures in different ionization zones do not bias the inferred temperatures. For example, a highly ionized H II region might contain a well-measured [O III] temperature from the dominant ionization zone and a poorly measured [S III] temperature from a physically smaller ionization zone. The opposite scenario is possible in a H II region dominated by the low- and intermediate-ionization zones. Electron temperatures in different ionization zones are dependent on similar properties (e.g., degree of ionization and metallicity). However, linear T_e – T_e relations that assume that one temperature is an independent variable, coupled with the asymmetric uncertainties on the measured temperatures, can result in non-invertible linear fits, depending on the applied fitting technique.

Orthogonal distance regression (ODR) is used to obtain invertible, linear T_e – T_e relations while considering the errors on the observed temperatures. ODR-generated relations are invertible by construction, but the fitted intrinsic dispersion about the best-fit relation is dependent on which temperature is assumed to be the dependent variable. Here, the intrinsic dispersion is defined as random scatter in the dependent variable about the best-fit regression. The intrinsic dispersion about a best-fit T_e – T_e relation can be interpreted as how much an ionization zone can deviate in temperature based on the H II region’s physical structure. Obtaining a temperature in an ionization zone via a T_e – T_e relation disregards true departures from the relationships, departures that a direct temperature may better represent. Therefore, it is critical to develop relations for each ionization zone that appropriately infer temperatures in the other zones and that use the intrinsic dispersion about each relation to better account for the unique physical conditions in each ionization zone. In Section 3.2 we describe the individual T_e – T_e relationships found for the CHAOS data, and we discuss our new methodology for applying the relationships in Section 3.3.

3.2. CHAOS Electron Temperatures and Relations

The combined CHAOS data provide an opportunity to reexamine the homogeneous T_e – T_e relations derived from the NGC 5457 H II regions (Croxall et al. 2016). Here, we use all significant detections from Berg et al. (2020) with those from NGC 2403 to create a data set of 213 H II regions with at least two temperature-sensitive auroral line detections. The data from Berg et al. (2020) is composed of H II regions from NGC 628 (Berg et al. 2015), NGC 5194 (Croxall et al. 2015), NGC 5457 (Croxall et al. 2016), and NGC 3184 (Berg et al. 2020). The previous T_e – T_e relations were fit using the PYTHON LINMIX package.¹¹ This package is the implementation of the IDL fitting program of Kelly (2007) and uses Bayesian statistics and MCMC techniques to fit a linear function to two variables with nonzero uncertainty while accounting for the intrinsic, random scatter in the dependent variable about the line of best fit. However, LINMIX does not produce invertible T_e – T_e relations due to the combination of asymmetric T_e uncertainties and the package’s treatment of uncertainty on the dependent and independent variables.

¹¹ <https://github.com/jmeyers314/linmix>

Here, the T_e – T_e data from all five galaxies are fit using the SCIPY ODR package. The ODR fit to the data is assumed to be a linear relation with the data weighted by their uncertainty in both temperatures. This method provides the best-fit linear relation but not the intrinsic dispersion about the relation. To obtain the intrinsic dispersion, we use a modified version of LINMIX. The modified version fixes the slope and intercept of the relation to the parameters of the ODR linear fit, then samples the parameter space to determine the value of σ_{int} , the intrinsic dispersion, that maximizes the likelihood function. The best-fit dispersion and its uncertainty are taken to be the median and standard deviation of the σ_{int} distribution, respectively.

Figure 3 plots the temperatures of the auroral lines used for abundance analysis and the best-fit T_e – T_e relations (gold dashed lines). Each permutation of the temperature data is fit with the above method, although this technique produces invertible T_e – T_e relations in all cases. For comparison, the black dashed lines are the best-fit T_e – T_e relations for the CHAOS NGC 5457 data from Croxall et al. (2016). Lines of equality are plotted as dotted black lines. The intrinsic and total dispersion (the latter determined in the same manner as Bedregal et al. 2006) in each relation are given in the bottom-right corner of each T_e – T_e plot.

3.2.1. Low- versus Intermediate-ionization T_e

The first row of the T_e – T_e subplots in Figure 3 relates the low- and intermediate-ionization zone temperatures described by T_e [N II] and T_e [S III], respectively. The addition of NGC 2403 brings the total number of H II regions with [N II] and [S III] temperatures to 108. The best-fit T_e – T_e relations are

$$T_e[\text{S III}] = 1.46(\pm 0.07) \times T_e[\text{N II}] - 0.41(\pm 0.05) \quad (2)$$

with $\sigma_{\text{int}} = 170 \pm 70$ K, and

$$T_e[\text{N II}] = 0.68(\pm 0.03) \times T_e[\text{S III}] + 0.28(\pm 0.02) \quad (3)$$

with $\sigma_{\text{int}} = 170 \pm 60$ K, where the units of the two relations (and those that follow) are in 10^4 K. With the addition of the NGC 2403 H II regions, the former relation has a slightly larger slope than the relation of Croxall et al. (2016), and the intrinsic dispersion about the fit is ~ 100 K less than previously reported. The temperatures of NGC 2403 further support the finding from previous CHAOS studies: a tight relation between T_e [N II] and T_e [S III] exists across a wide range of electron temperatures.

3.2.2. Intermediate- versus High-ionization T_e

The second row of panels in Figure 3 shows how the intermediate-ionization zone temperatures of T_e [S III] are related to the high-ionization zone temperatures of T_e [O III]. The best-fit relations for the 76 H II regions are

$$T_e[\text{S III}] = 1.58(\pm 0.17) \times T_e[\text{O III}] - 0.57(\pm 0.16) \quad (4)$$

with $\sigma_{\text{int}} = 1110 \pm 140$ K, and

$$T_e[\text{O III}] = 0.63(\pm 0.07) \times T_e[\text{S III}] + 0.36(\pm 0.06) \quad (5)$$

with $\sigma_{\text{int}} = 800 \pm 100$ K. The T_e [S III]– T_e [O III] relation only just agrees with the previous relation of Croxall et al. (2016) within the uncertainty, and this relation contains the largest intrinsic dispersion about the T_e – T_e relations of Figure 3. Similar intrinsic dispersion in the T_e [S III]– T_e [O III] relation is observed by Croxall et al. (2016), but the difference between

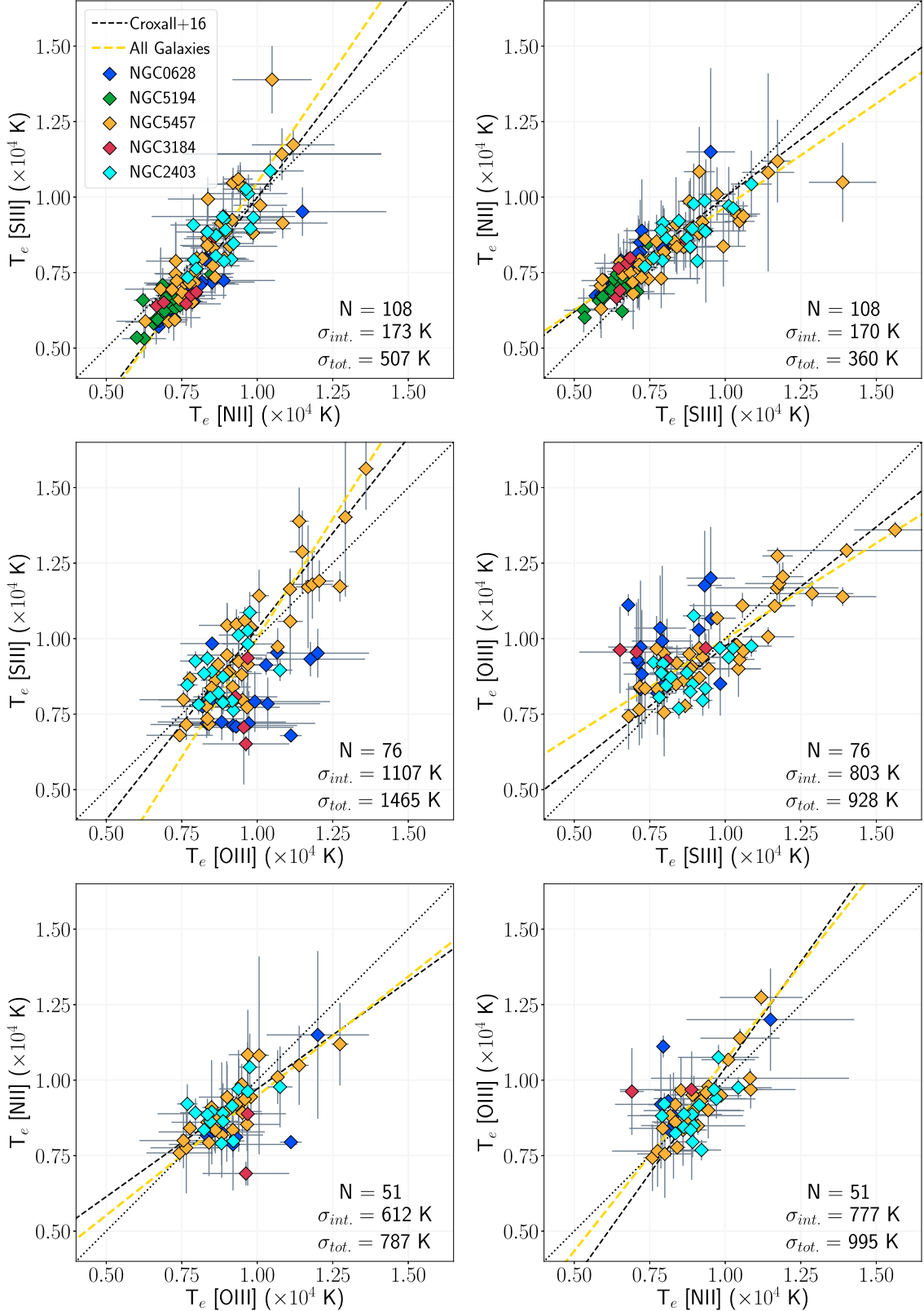


Figure 3. The T_e data for the [O III], [S III], and [N II] auroral lines in each CHAOS galaxy, color-coded by the host galaxy. ODR linear fits to the combined data are plotted in gold, the previous T_e - T_e relations obtained for the NGC 5457 H II regions (Croxall et al. 2016) are plotted as dashed black lines, and the dotted black line represents equivalent temperatures. The rows are ordered by ionization zone relations: the top row compares temperatures in the low- and intermediate-ionization zone, the middle row compares temperatures in the intermediate- and high-ionization zone, and the bottom compares temperatures in the low- and high-ionization zones. Intrinsic and total scatters are included in the bottom-right corner of each plot.

this dispersion and the dispersion in the $T_e[\text{O III}]-T_e[\text{S III}]$ relation is not reported. The larger intrinsic dispersion in $T_e[\text{S III}]-T_e[\text{O III}]$ implies that the intermediate- and high-ionization zone temperatures can vary significantly due to the physical properties of a H II region.

3.2.3. Low- versus High-ionization T_e

The bottom row of Figure 3 plots the relations for the low- and high-ionization zone temperatures. There are fewer H II regions with concurrent $[\text{N II}]\lambda 5755$ and $[\text{O III}]\lambda 4363$ detections than regions with concurrent $[\text{N II}]\lambda 5755$ and $[\text{S III}]\lambda 6312$ detections or $[\text{S III}]\lambda 6312$ and $[\text{O III}]\lambda 4363$ detections. $[\text{O III}]\lambda 4363$ emission corresponds to high electron energies, the product of a hard ionizing source. Depending on the ionizing source, the low-ionization zone within the H II region might be physically smaller than the high-ionization zone, making $[\text{N II}]\lambda 5755$ less likely to be detected. On the other hand, high-metallicity H II regions typical of spiral galaxies will have lower electron energy. Given the high excitation energy of $[\text{O III}]\lambda 4363$, $[\text{N II}]\lambda 5755$ is more likely to be detected in these regions. Nevertheless, there are 51 H II regions with simultaneous detection, and the resulting best-fit T_e-T_e relations are

$$T_e[\text{N II}] = 0.79(\pm 0.14) \times T_e[\text{O III}] + 0.16(\pm 0.13) \quad (6)$$

with $\sigma_{\text{int.}} = 610 \pm 110$ K, and

$$T_e[\text{O III}] = 1.3(\pm 0.2) \times T_e[\text{N II}] - 0.2(\pm 0.2) \quad (7)$$

with $\sigma_{\text{int.}} = 780 \pm 140$ K. The first relation is consistent with the previous empirical relation for NGC 5457, but the intrinsic dispersion is a factor of 2 larger than that of the NGC 5457 data alone. NGC 5457 contains the most regions with both $[\text{N II}]\lambda 5755$ and $[\text{O III}]\lambda 4363$ detections; the inclusion of the other CHAOS galaxies adds additional scatter about the best-fit relation. The difference in the relations reveals the importance of including multiple galaxies to develop robust empirical T_e-T_e relations.

3.2.4. Other T_e-T_e Relations

The majority of H II regions in NGC 2403 contain $[\text{O II}]\lambda\lambda 7320, 7330$ and $[\text{S II}]\lambda\lambda 4069, 4076$ detections. Although these lines are presently not used to determine electron temperatures for abundance analysis, we can assess how these direct temperatures relate to those of the commonly used auroral lines described above. The top panel of Figure 4 plots $T_e[\text{N II}]$ versus $T_e[\text{O II}]$, which compares the electron temperatures determined by two ions originating, primarily, in the low-ionization zone. The best-fit relation is $T_e[\text{N II}] = 0.45(\pm 0.05) \times T_e[\text{O II}] + 0.36(\pm 0.05)$, and the intrinsic dispersion about this relation, $\sigma_{\text{int.}} = 590 \pm 70$ K, is consistent with that found in the $T_e[\text{N II}]$ versus $T_e[\text{O III}]$ relation. The best-fit slope is not consistent with unity, which one might expect for two ions originating in the same ionization zone. The ODR fit prioritizes the orthogonal distance of the points with low temperature uncertainty, resulting in a relation that may not follow the majority of the data. $[\text{O II}]\lambda\lambda 7320, 7330$ are relatively bright compared to the other auroral lines available in the optical, but the above relation reveals that it may be difficult to infer $T_e[\text{N II}]$ using $[\text{O II}]$ auroral line emission.

The same may be said for inferring $T_e[\text{O III}]$ from $T_e[\text{O II}]$, as the relation obtained in the middle panel of Figure 4 has an intrinsic dispersion of $\sigma_{\text{int.}} = 1280 \pm 140$ K, larger than the

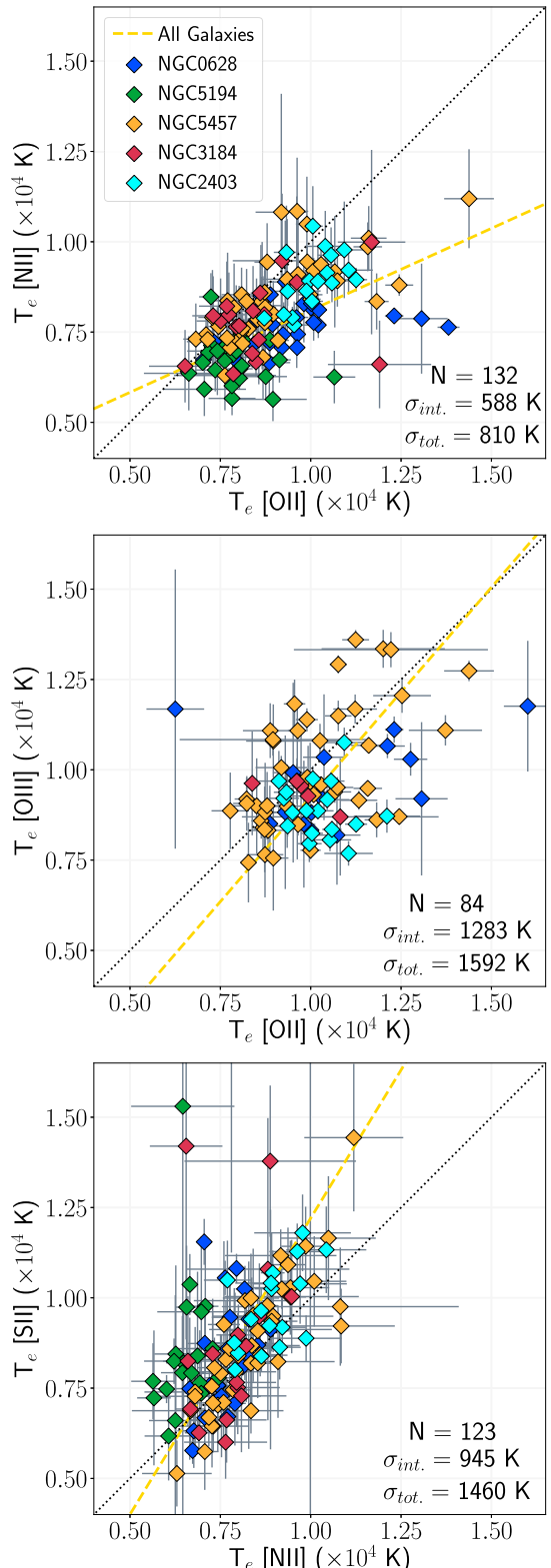


Figure 4. T_e-T_e relations for the electron temperatures determined from the auroral lines $[\text{O II}]\lambda\lambda 7320, 7330$ and $[\text{S II}]\lambda\lambda 4069, 4076$. The top and bottom panels display how the temperatures from these two ions are related to the low-ionization zone temperatures of $[\text{N II}]$. The middle panel compares $[\text{O II}]$ temperatures to the high-ionization zone temperatures from $[\text{O III}]$.

dispersion observed in $T_e[\text{S III}]$ versus $T_e[\text{O III}]$. Other abundance studies have found similar scatter about the $T_e[\text{O III}]-T_e[\text{O II}]$ relation (see Kennicutt et al. 2003b), and it

has been shown that factors such as dielectronic recombination (Rubin 1986; Liu et al. 2001) or contamination (by airglow or telluric absorption) can affect the electron temperatures determined by $[\text{O II}]\lambda\lambda 7320, 7330$. Dielectronic recombination biases $T_e[\text{N II}]$ and $T_e[\text{O II}]$ high, but the tight relation with $[\text{S III}]$ temperatures requires that the contribution of recombination to $[\text{N II}]\lambda 5755$ emission must be small in the majority of the H II regions observed (see discussion in Berg et al. 2020). A relation that is linear in electron temperature may not completely capture the trends observed in $T_e[\text{O III}]$ versus $T_e[\text{O II}]$ (see López-Sánchez et al. 2012; Nicholls et al. 2014; Yates et al. 2020). For now, we simply note that the $[\text{O II}]$ temperatures measured in NGC 2403 are consistent with the trends found in the other CHAOS studies.

$T_e[\text{S II}]$ versus $T_e[\text{N II}]$, which also examines the relation of two ions in the low-ionization zone, is plotted in the bottom of Figure 4. This relation, $T_e[\text{S II}] = 1.64(\pm 0.17) \times T_e[\text{N II}] - 0.42(\pm 0.13)$, is also not consistent with a slope of unity. The general trend is an offset toward higher $T_e[\text{S II}]$ at fixed $T_e[\text{N II}]$, and the intrinsic dispersion is large: $\sigma_{\text{int}} = 950 \pm 120$ K. This scatter is possibly related to the differences in the ionization energies of the two ions. $[\text{S II}]$ emission can originate in a photodissociation region (PDR), a region of primarily neutral gas outside the H II region. The temperature within a PDR is not characteristic of the electron temperature within the H II region, so a comparison between the two may result in the increased scatter in $T_e - T_e$ space observed in the bottom panel of Figure 4.

More direct electron temperature data are needed to fully explore the empirical $T_e - T_e$ relations. For example, the tight relation between $T_e[\text{N II}]-T_e[\text{S III}]$ may not hold at larger temperatures where there is currently a lack of direct $T_e[\text{N II}]$ and $T_e[\text{S III}]$ data. For intermediate- and high-ionization zone relations, Berg et al. (2020) note that the offsets in $T_e - T_e$ space from the best-fit relation could be dependent on a H II region's average ionization, characterized by the parameter $O_{32} = \frac{I(5007)}{I(3727)}$. An analysis of how these offsets are dependent on second parameters will be conducted once more electron temperature data are added to the CHAOS sample. Finally, the trends found in $[\text{O II}]$ and $[\text{S II}]$ temperatures can be explored with the entire CHAOS sample, with the hope that future abundance studies will make use of these temperatures.

3.3. Application of CHAOS $T_e - T_e$ Relations

As described above, applying a linear $T_e - T_e$ relation to obtain the electron temperature in a different ionization zone may not account for the unique physical properties within a given H II region. If the intrinsic dispersion in $T_e - T_e$ space is representative of how differences in physical properties of H II regions affect the measured electron temperatures in these zones, then one must account for this dispersion in order to appropriately infer the temperature in another zone. Not accounting for this intrinsic dispersion is equivalent to neglecting the shortcomings of a linear relation in fitting the data and to assuming that specific H II region properties have little effect on the dispersion of measured electron temperatures.

The uncertainties on the electron temperature inferred from a $T_e - T_e$ relation present an opportunity to incorporate the intrinsic dispersion about the $T_e - T_e$ relation. Previous abundance studies have obtained uncertainties on inferred temperatures from $T_e - T_e$ relations in a number of different ways. For instance, Skillman et al. (2003) used standard propagation of

errors to obtain the uncertainties on the inferred temperatures when applying the photoionization temperature relations of Pagel et al. (1992) and set a lower limit on the inferred T_e uncertainty of 500 K. The lower limit is applied to avoid the small uncertainties on inferred temperatures that would result from propagating errors through a linear $T_e - T_e$ relation that does not account for all the physical properties of a H II region. Kennicutt et al. (2003b) either used the uncertainty on the measured temperature as the uncertainty on the inferred temperature when applying the Garnett (1992) $T_e - T_e$ relations or augmented this uncertainty by 500 K added in quadrature. Rosolowsky & Simon (2008) used the photoionization $T_e - T_e$ relations of Campbell et al. (1986) to obtain $T_e[\text{O II}]$ for all H II regions they observe in M33. The error in their inferred $T_e[\text{O II}]$ values is assumed to be 300 K, citing the magnitude of the uncertainties in Kennicutt et al. (2003b) as justification for this choice. Finally, Esteban et al. (2020) used the empirical, linear $T_e - T_e$ relations from Esteban et al. (2009) when necessary, and standard propagation of errors is applied, without a lower limit, to obtain the uncertainties on the inferred temperatures.

With the amount of electron temperature data amassed by CHAOS, we can now update the method we apply to obtain uncertainties on inferred electron temperatures. This method attempts to account for both the uncertainty in the measured temperature being used to infer a temperature in a different ionization zone and the uncertainty in applying a linear $T_e - T_e$ relation to account for the potential range of physical conditions within a H II region. For an inferred electron temperature $T_{e,Y}$ determined by the direct temperature $T_{e,X}$ and the $T_e - T_e$ relation $T_{e,Y} = m \times T_{e,X} + b$, the uncertainty on the inferred temperature, $\delta T_{e,Y}$, is now determined by

$$\delta T_{e,Y} = \sqrt{(m \times \delta T_{e,X})^2 + (\sigma_{i,Y})^2}, \quad (8)$$

where $\sigma_{i,Y}$ is the intrinsic dispersion in $T_{e,Y}$ about the relation. With this equation, a lower bound is imposed on the inferred temperature uncertainty equivalent to the intrinsic dispersion about the best-fit relation. In this way, applying one of the above $T_e - T_e$ relations always results in a higher fractional uncertainty on the inferred temperature, but the result accounts for some of the unknowns that are not fit when applying a linear $T_e - T_e$ relation. In other words, the uncertainty on the inferred temperature is now more likely to capture the true electron temperature within the ionization zone. The best-fit variables and intrinsic dispersion of each relation will change as more electron temperature data are acquired; if the intrinsic dispersion becomes smaller, then so too will the lower bound on the inferred temperature uncertainties. Moving forward, we use Equation (8) to determine the uncertainty in the inferred electron temperatures, and this approach is recommended for all studies using linear, empirical $T_e - T_e$ relations.

While the intrinsic dispersion about a $T_e - T_e$ relation is readily obtained for empirical relations, an estimate on the scatter when using photoionization model $T_e - T_e$ relations can be obtained by varying model inputs and finding a range of possible best-fit parameters. More recent $T_e - T_e$ relations have adopted nonlinear forms (López-Sánchez et al. 2012; Arellano-Córdova & Rodríguez 2020), while others have included a dependence on the H II region's metallicity (Nicholls et al. 2014; Yates et al. 2020). An exploration of how the intrinsic scatter can be used in these relations is beyond the scope of this paper, but we stress that inferred electron temperatures that

account for the two main sources of uncertainty discussed above are critical for proper abundance analysis.

In fitting the different temperature permutations with a linear relation, we have assumed that each ion temperature is a smooth function of the electron temperature in a different ionization zone. As mentioned earlier, ionization zone temperatures within a H II region are dependent on similar parameters, such as degree of ionization, metallicity, etc. Additionally, the errors on the data strongly affect the ODR linear fits, which can bias the line of best fit toward temperatures from well-measured lines in extremely bright H II regions. In future works, we will consider additional parameters and explore possible nonlinear T_e – T_e relations to better fit the observed scatter in electron temperatures.

4. Abundance Determinations in NGC 2403

To determine gas-phase abundances, we assume a five-level atom model (De Robertis et al. 1987) with the updated atomic data used in Berg et al. (2015). This model is used with the electron temperature of a given ionization zone in PYNEB’s `getIonAbundance` function, assuming an electron density of 10^2 cm $^{-3}$, to obtain the abundance of an ion in that zone. The fractional uncertainties in the line intensity ratio and in the emissivity (as a function of temperature) are added in quadrature to obtain the ionic abundance uncertainty. This process is applied to the uncertainty on relative abundances of ions within the same ionization zone (e.g., Ne $^{2+}$ /O $^{2+}$). For these cases, the fractional uncertainty on the net emissivity is usually small relative to the intensity uncertainty because of the similar temperature dependencies of the emissivities.

Previously, Berg et al. (2020) used ionization-based temperature prioritizations to determine the electron temperature in the three ionization zones. This method attempts to use, when possible, a direct temperature measurement from the dominant ionization zone within a H II region (see Figure 5 in Berg et al. 2020, reproduced in Appendix B as Figure B1). If a temperature outside the dominant ionization zone is used with a T_e – T_e relation, then the resulting fractional uncertainty on the ionization zone temperature will be large due to the addition of the intrinsic dispersion about the T_e – T_e relation. This increased temperature, and abundance, uncertainty is sometimes not reflective of the quality of the spectra, particularly spectra with multiple auroral line detections. For instance, an [O III] $\lambda 4363$ detection at high S/N might more reliably determine the true electron temperature in the high-ionization zone than a low-S/N [S III] $\lambda 6312$ detection with a T_e – T_e relation.

An alternative approach is to use all electron temperature measurements as independent methods of calculating the electron temperature in a given ionization zone. This is justified because all ionization zones within a H II region are assumed to have the same metallicity, and metallicity is the dominant parameter in determining the electron temperature. Thus, electron temperatures in different ionization zones are strongly correlated. When all three commonly used auroral lines are measured, the direct electron temperature from the dominant ion and the two inferred temperatures from the T_e – T_e relations are combined in a weighted average to determine the ionization zone temperature. The uncertainty on an inferred electron temperature when using a T_e – T_e relation will typically weight these temperatures lower than a direct temperature measurement from the dominant ion. The exception is when the dominant ion is measured at low S/N, which results in an

ionization zone temperature that is closer to the average of the measured and inferred temperatures. In this way, a single, poorly constrained electron temperature will not bias the ionization zone temperature used in abundance determination.

The uncertainty in the ionization zone temperature is taken to be the uncertainty of the weighted average, which is smaller than the uncertainty on the most well-measured temperature used in calculating the weighted average. The abundance analysis has been repeated by adopting the lowest temperature uncertainty of the values used to calculate the weighted average, and all results are consistent within uncertainty. Adopting a weighted-average ionization zone temperature removes the prioritization based on the average ionization of a H II region in favor of utilizing all available temperature data in the CHAOS sample. A comparison of the weighted-average and ionization-based temperature prioritizations is given in Appendix B, and it is found that the two prioritization methods produce consistent results. As discussed in Section 3.2.4, the [O II] and [S II] auroral lines are not used for abundance determination due to the dispersion observed in the temperatures. Only the H II regions with at least one of the auroral lines from [O III], [N II], or [S III] are used for abundance determination, which brings the number of H II regions in NGC 2403 that are used for abundance analysis to 28. Table A2 provides the adopted temperature in each ionization zone, the ionic abundances, and ionization correction factors (ICFs) used for these 28 regions.

4.1. Oxygen Abundances

The dominant ionization states of oxygen in a HII region are O $^+$ in the intermediate- and low-ionization zones and O $^{2+}$ in the high-ionization zone. The ionization energy of O 0 is close to that of neutral hydrogen, but the ratio of [O I] $\lambda 6300$ to H β can assess the amount of O 0 in each region. However, the observed neutral oxygen emission may come from a PDR, so including the neutral oxygen may not appropriately estimate the amount of oxygen contained within the H II region.

For the typical temperature of an O- or B-type star, the number of photons able to triply ionize oxygen makes up a small fraction of the total photons produced. Photons that can triply ionize oxygen can doubly ionize helium, so we would expect emission from the He II recombination lines if we observe an extremely ionized H II region. For the one H II region where narrow He II $\lambda 4686$ emission is detected (NGC 2403+160–251), a possible correction to account for the presence of O $^{3+}$ /H $^+$ could be justified. However, the size of this correction is smaller than the uncertainty on O/H, so no correction is applied to account for O $^{3+}$ in the regions of NGC 2403. Additionally, we do not correct for the depletion of oxygen onto dust grains, which is on the order of 0.1 dex in the most metal-rich H II regions (Peimbert & Peimbert 2010; Peña-Guerrero et al. 2012). Therefore, it is assumed that all of the oxygen in a H II region is present in either O $^+$ or O $^{2+}$ such that O/H = (O $^+$ + O $^{2+}$)/H $^+$.

4.2. Nitrogen Abundances

Other common emission lines from N, Ne, S, and Ar are observed in a typical CHAOS spectrum, but these elements have unobserved ionic species in the optical. Ionization correction factors account for the unobserved ionic species of an element, J, by weighting the observed ionic species with a

function, $ICF(J)$, or: $\frac{J}{H} = ICF(J) \times \frac{J^{+i}}{H^{+i}}$. A common example is nitrogen with the observable lines of N^+ but with no emission lines of N^{2+} or N^{3+} in our wavelength range. The ionization energy of O^+ fully spans that of N^+ , thus it is often assumed that $N/O \approx N^+/O^+$. This approximation is useful because the ratio primarily relates two lines originating in the low-ionization zone, but O^+ also slightly overlaps with the intermediate-ionization zone. This ICF is found to be good to within 10% of the actual N/O abundance, with the departures coming primarily from low-metallicity ($12 + \log(O/H) < 8.1$) systems (Nava et al. 2006). None of the H II regions in NGC 2403 have oxygen abundances less than 8.1, so it is assumed that $ICF(N) = O/O^+$ will accurately describe the data. We determine the N^+/O^+ relative abundance and uncertainty using the emissivity ratio $j_{[N\,II]\lambda6584}/j_{[O\,II]\lambda3727}$ directly with the low-ionization zone temperature and the observed intensity of $[N\,II]\lambda6584$ and $[O\,II]\lambda3727$.

4.3. α Elements: $ICFs$ and Abundances

4.3.1. Neon

The singly and doubly ionized states of neon are present in a typical H II region, but only one line, $[Ne\,III]\lambda3868$, is commonly, and easily, observed in CHAOS spectra.¹² $[Ne\,III]$ emission comes from the high-ionization zone, so it is common to employ the ICF of Peimbert & Costero (1969): $ICF(Ne) = O/O^{2+}$, such that $Ne/O = Ne^{2+}/O^{2+}$ (see also Crockett et al. 2006). However, the reliability of this ICF at low ionization has come into question. This can be seen in the top panel of Figure 5, where the scatter about the best-fit average (black line) of Ne^{2+}/O^{2+} grows substantially at intermediate ionization ($O^+/O > 0.5$), with much of the scatter coming from regions with low Ne^{2+}/O^{2+} at fixed O^+/O . This trend has been observed in previous CHAOS studies (Croxall et al. 2016; Berg et al. 2020) and planetary nebula studies (for example, Torres-Peimbert & Peimbert 1977).

Motivated by the findings of García-Rojas et al. (2013), we examine Ne/Ar in each region and find that many of the regions with low Ne^{2+}/O^{2+} have low Ne/Ar . For regions with $O^+/O > 0.5$, Berg et al. (2020) corrected the Ne/O abundance by subtracting the difference between $\log(Ne/Ar)$ and $\log(Ne/Ar)_{avg}$ from $\log(Ne/O)$. For regions with low Ne/Ar relative to the average Ne/Ar of all regions, this preliminary correction offsets the low neon abundances and results in larger $\log(Ne/O)$ at low ionizations. Alternatively, the Ne/O abundances can be lowered for regions with high Ne/Ar (or low Ar/O) abundances.

In the lower panel of Figure 5, the regions with $\log(Ne/Ar) < \log(Ne/Ar)_{avg} - \log(Ne/Ar)_{sig}$ are noted in yellow, where $\log(Ne/Ar)_{sig}$ is the 1σ error on $\log(Ne/Ar)_{avg}$. These are the regions that would benefit most from the correction in Berg et al. (2020), resulting in larger Ne^{2+}/O^{2+} values and lower scatter about the best-fit Ne^{2+}/O^{2+} average. The regions with $\log(Ne/Ar) > \log(Ne/Ar)_{avg} + \log(Ne/Ar)_{sig}$ are noted in purple. These regions could benefit from the correction, but some regions close to the line of best fit have low argon abundance (see Figure 7) resulting in relatively large offsets from the average Ne/Ar value. This means that these regions could have their Ne^{2+}/O^{2+} ratios oversubtracted, resulting in increased scatter

¹² The reduction pipeline also fits $[Ne\,III]\lambda3967$, but this line is blended with $He\,I\,\lambda3964$ and $He\,II\,\lambda3970$. As such, it is not used for Ne abundance determinations.

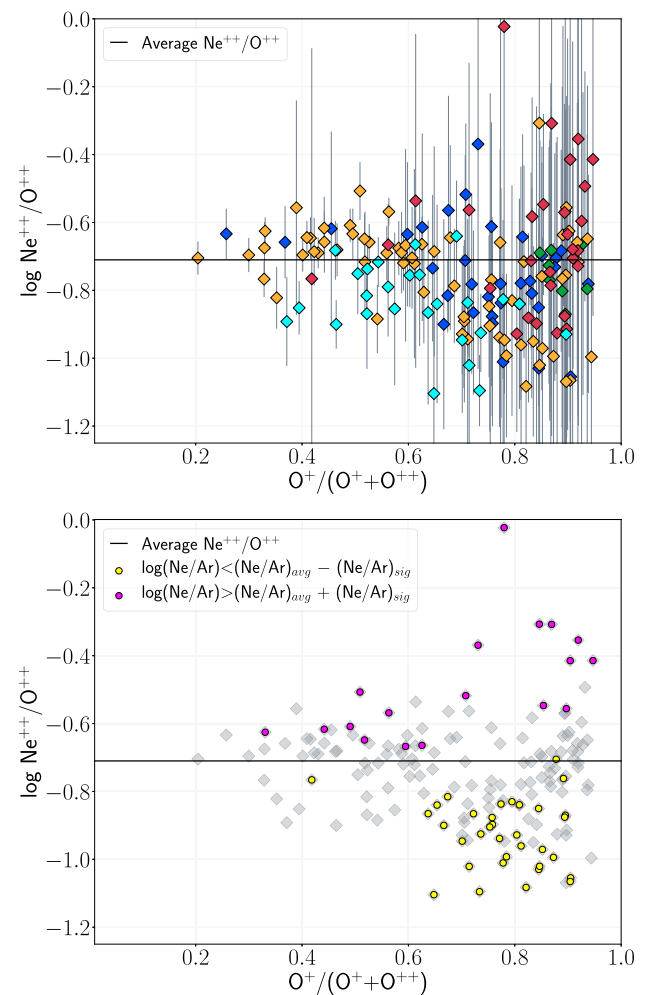


Figure 5. Top panel: $\log(Ne^{2+}/O^{2+})$ data from all five CHAOS galaxies plotted against each region's O^+/O . Uncertainty on O^+/O is not plotted for clarity. The weighted average of the data is plotted as a solid black line. Data are color-coded by galaxy (same as Figure 3). Bottom panel: the same data are plotted, except the colors and errors are now removed. The yellow points indicate regions with $\log(Ne/Ar) < \log(Ne/Ar)_{avg} - \log(Ne/Ar)_{sig}$ and the purple points indicate regions with $\log(Ne/Ar) > \log(Ne/Ar)_{avg} + \log(Ne/Ar)_{sig}$. The dispersion about the average Ne^{2+}/O^{2+} grows at lower ionization and is dominated by the points with enhanced or reduced Ne/Ar .

(this has also been noted in Berg et al. 2020). We simply adopt $ICF(Ne) = O/O^{2+}$ for this study. We use the relative emissivities of $[Ne\,III]\lambda3868$ and $[O\,III]\lambda5007$, the intensity of these lines, and the high-ionization zone temperature to obtain the Ne^{2+}/O^{2+} relative abundance.

4.3.2. Sulfur

The emission from S^{2+} characterizes the intermediate-ionization zone, but S^{3+} is expected to be present in a H II region given that the ionization energy of S^{2+} is 34.79 eV, about the same as that of O^+ . However, there are no S^{3+} emission lines in our wavelength range, requiring an ICF to account for the missing ions in this ionization state. The ionization energies of S^0 and S^{2+} (10.36 and 34.79 eV) cover an energy range that is nearly coincident with that of O^0 and O^+ (13.62 and 35.12 eV). Previous CHAOS studies (Croxall et al. 2016; Berg et al. 2020) have examined the approximation $S/O = (S^+ + S^{2+})/O^+$ (see Peimbert & Costero 1969) such that the ICF for S is $ICF(S) = O/O^+ = (O^+ + O^{2+})/O^+$.

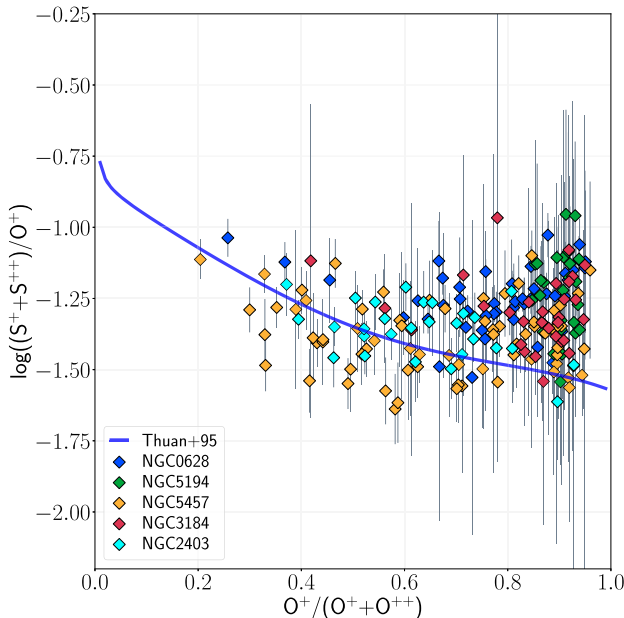


Figure 6. The $\log((S^+ + S^{2+})/O^+)$ data from all five CHAOS galaxies plotted against each region’s O^+/O . Uncertainty on O^+/O is not plotted for clarity. The Thuan et al. (1995) photoionization ICF is plotted as a solid blue line. While the photoionization ICF appears to underpredict the $(S^+ + S^{2+})/O^+$ low ionization, it fits the general trend of the regions with $O^+/O < 0.6$.

This approximation is particularly useful when the ionization of a H II region is such that the O^+ zone is more dominant than the O^{2+} zone. In such a H II region, the ICF is accounting for a smaller fraction of unobserved S^{3+} and is using detections from a proportionally larger volume of the H II region to infer the relative sulfur abundance. For higher ionization H II regions, this ICF is not adequate to describe the amount of S^{3+} present.

Figure 6 plots $\log((S^+ + S^{2+})/O^+)$ versus O^+/O for the H II regions in the present CHAOS sample. The sulfur ICF of Thuan et al. (1995) is plotted as a solid blue line. This ICF is generated from the photoionization models of Stasińska (1990) and is a function of O^+/O . The ICF tends to underpredict the $(S^+ + S^{2+})/O^+$ observed in the CHAOS H II regions with $O^+/O > 0.6$, which are the regions where the $ICF(S) = O/O^+$ is believed to be the most reliable. Instead, we find general agreement between the ICF of Thuan et al. (1995) and the data at $O^+/O < 0.6$, although there are fewer highly ionized H II regions in the sample and there is an appreciable amount of scatter. Given this general agreement, we adopt $ICF(S) = O/O^+$ when $O^+/O > 0.6$ and the ICF from Thuan et al. (1995) when $O^+/O < 0.6$, similar to the technique previously applied in other CHAOS galaxies (see Croxall et al. 2016; Berg et al. 2020). The percent uncertainty when applying the Thuan et al. (1995) ICF is assumed to be 10%. The energy required to ionize S^0 (10.36 eV) is such that some S^+ is contained within a PDR. This portion should be discounted when determining the true sulfur abundance within the H II region, but it is assumed that this makes up a small fraction of the total S^+ abundance.

4.3.3. Argon

Multiple ionization states of Ar are expected to be present in a typical H II region: Ar^+ is present in the low-ionization zone, Ar^{2+} in the intermediate- and high-ionization zones, and Ar^{3+} can be found in the high-ionization zone. For CHAOS, the only easily observed emission lines in these ionization states are $[Ar\ III]$

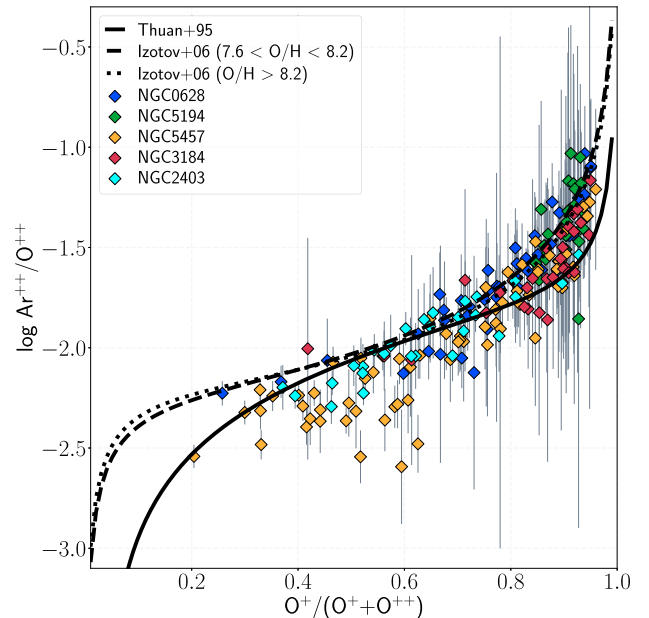


Figure 7. The $\log(Ar^{2+}/O^{2+})$ data from all five CHAOS galaxies plotted against each region’s O^+/O . Uncertainty on O^+/O is not plotted for clarity. With the updated temperatures and abundances, the shape of the CHAOS data is better fit by the metallicity-dependent ICF of Izotov et al. (2006, dashed and dotted lines) rather than the ICF of Thuan et al. (1995, solid line).

$\lambda 7135$ and the occasional $[Ar\ IV]\lambda 4740$ in the most highly ionized H II regions. The overlap of Ar^{2+} with the intermediate-ionization zone has motivated previous studies to use Ar^{2+}/S^{2+} relative abundances and ICFs. Both Kennicutt et al. (2003b) and Croxall et al. (2016) found that the Ar^{2+}/S^{2+} ratio remains relatively constant over a range of O^+/O values, with the latter adopting a linearly decreasing ICF to account for the lowest ionization H II regions of the CHAOS sample. After updating the ionic abundance data using ionization-based temperature prioritizations, Berg et al. (2020) determined that the photoionization model ICF from Thuan et al. (1995) fit the CHAOS data over a large range of ionization.

Figure 7 plots the Ar^{2+}/O^{2+} data versus O^+/O from the CHAOS sample. With the updated electron temperatures and the use of a weighted-average temperature in each ionization zone, the agreement between the CHAOS data and the expected Ar^{2+}/O^{2+} trend from the Thuan et al. (1995) ICF (solid line) is less obvious, particularly at $O^+/O > 0.8$. Applying this ICF may lead to unphysical trends in Ar/O , requiring a new argon ICF. Plotted as dashed and dotted lines are the intermediate- and high-metallicity argon ICFs of Izotov et al. (2006), respectively. The shape of these ICFs matches the observed trends in the CHAOS Ar^{2+}/O^{2+} data over nearly the entire range of H II region ionization. We update our Ar^{2+} ICF to be that of Izotov et al. (2006). The intermediate-metallicity ICF is applied when a H II region has $12 + \log(O/H) < 7.6$, the high-metallicity ICF is applied at $12 + \log(O/H) > 8.2$, and a linear interpolation of the two for $7.6 < 12 + \log(O/H) < 8.2$. As with the sulfur ICF, there is an attributed 10% uncertainty for applying the Izotov et al. (2006) ICF.

5. Direct Abundance Gradients

The above methods are used to calculate the abundances of all CHAOS galaxies using all regions from Berg et al. (2020) with at least one of the auroral lines from $[O\ III]$, $[N\ II]$, or $[S\ III]$

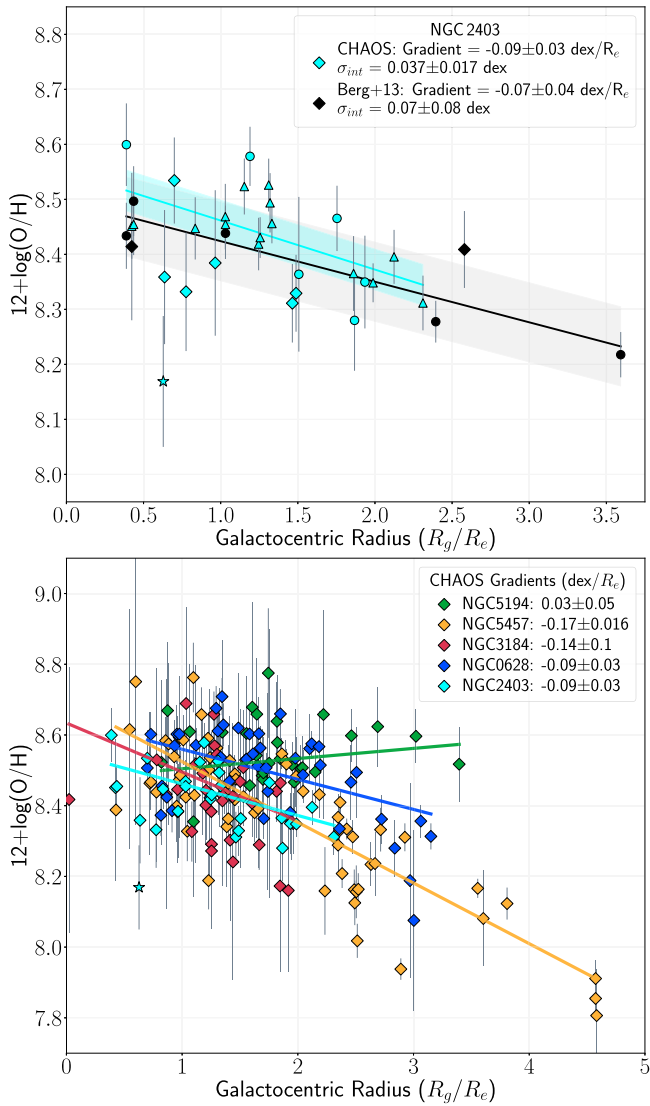


Figure 8. Top panel: CHAOS (cyan) and the recalculated Berg et al. (2013, black) oxygen abundances in NGC 2403 plotted vs. R_g/R_e . The gradients in each galaxy are plotted as solid lines and are provided in the legend. The intrinsic dispersion about each gradient, represented as the shaded region around each gradient, is also reported in the legend. The number of direct electron temperatures used in the weighted-average temperature in each ionization zone are represented by the different shapes: diamonds = 1 direct temperature; circles = 2; triangles = 3. Bottom panel: same as the top panel but for the oxygen abundances of all CHAOS galaxies and the regions are no longer distinguished by the number of direct T_e used in the average. The shaded portions around each gradient are removed for clarity, and the galaxies listed in the legend are ordered by decreasing stellar mass.

detected. The following sections discuss the resulting O/H and N/O abundance gradients

5.1. Oxygen Abundance Gradient in NGC 2403

The top panel of Figure 8 plots, in cyan, the oxygen abundances measured in NGC 2403. The abundances are plotted against the galactocentric radius of the H II regions normalized to the effective, or half-light, radius (R_e) of NGC 2403. The effective radius of NGC 2403 is measured from the ZOMGS WISE 1 maps using the same technique as applied to the previous four CHAOS galaxies (see discussion in Appendix C of Berg et al. 2020). For each region, the number

of direct electron temperatures applied in the weighted-average ionization zone temperatures is designated by the shape of the point used: diamonds = 1 temperature, circles = 2, and triangles = 3.

LINMIX is applied to find the best-fit gradients, assuming that the errors on the distances are $0.05 \times R_e$ for each H II region. Additionally, the abundance gradients are fit with the ODR and modified LINMIX combination described in Section 3.2. The abundance gradients and intrinsic dispersions determined by the LINMIX-only fits are consistent with the ODR-LINMIX combination fits, so we adopt the former. The gradient determined for the regions of NGC 2403 reported here is

$$12 + \log(O/H) = 8.55(\pm 0.04) - 0.09(\pm 0.03)R_g/R_e. \quad (9)$$

Using the position of each H II region in kiloparsec, the gradient in NGC 2403 is

$$12 + \log(O/H) = 8.55(\pm 0.04) - 0.032(\pm 0.010)R_g \text{ kpc}^{-1}. \quad (10)$$

The intrinsic dispersion about these fits is $\sigma_{\text{int}} = 0.037 \pm 0.017$ dex; the shaded region about the gradient in Figure 8 represents the intrinsic dispersion. The oxygen abundance gradient is determined from 27 H II regions; one H II region, NGC 2403 +88–18 (the cyan star in Figure 8), is not fit in the reported oxygen abundance gradient due to the presence of unrecognizable and extreme emission features.

Garnett et al. (1997) and Berg et al. (2013) have previously observed NGC 2403 and conducted direct abundance studies on a number of H II regions within the galaxy. The former used the Imaging Photon Counting System (IPCS) at La Palma Observatory to measure the auroral lines of [O III], [S III], and [O II] in 12 H II regions in NGC 2403. The latter used the Blue Channel Spectrograph on the MMT to observe seven bright H II regions in NGC 2403, allowing for direct T_e [O III] and T_e [N II] determination. These two studies measured the slope of the oxygen abundance gradient in NGC 2403 as -0.102 ± 0.009 dex kpc^{-1} (Garnett et al. 1997) and -0.027 ± 0.008 dex kpc^{-1} (Berg et al. 2013). Additionally, Berg et al. (2013) reported an intrinsic scatter about the oxygen abundance gradient of 0.02 dex. We observe some of the same H II regions as Garnett et al. (1997), but the IPCS has nonlinear counting effects and complicated statistical errors at all count rates (Jenkins 1987). As such, we only perform a complete comparison to the direct abundances of Berg et al. (2013).

Berg et al. (2013) targeted seven bright H II regions, four of which overlap with our observations. Multiple factors could result in differences between our findings and the results reported in Berg et al. (2013): our T_e – T_e relations and uncertainties are different from those of Garnett (1992; see Section 3), we determine the electron temperature in an ionization zone using the weighted average of all temperature data, the atomic data are updated (see Berg et al. 2015), and we observe roughly four times as many regions with temperature-sensitive auroral lines. To eliminate as many systematic differences as possible, we use the reported line intensities from the H II regions in Berg et al. (2013) and recalculate the temperatures and abundances following the methods described in Sections 3 and 4. This includes the use of PYNEB to determine T_e [N II] and T_e [O III] from their observations (T_e [S III] is unobtainable due to the lack of wavelength

coverage for the [S III] nebular lines), the T_e – T_e relations and new application method described in Section 3, weighted-average temperatures in each ionization zone, and updated atomic data and ICFs for the elemental abundances.

The top panel of Figure 8 plots, in black, the updated direct abundances of NGC 2403 acquired from the line intensities of Berg et al. (2013).¹³ The shapes of the points represent the number of direct temperatures used in the weighted-average ionization zone temperatures. Because Berg et al. (2013) obtain no direct [S III] temperatures, the maximum number of temperatures used in the weighted average is two. The oxygen abundance gradient is calculated for these seven regions:

$$12 + \log(O/H)_{B+13} = 8.50(\pm 0.09) - 0.07(\pm 0.04)R_g/R_e, \quad (11)$$

or

$$12 + \log(O/H)_{B+13} = 8.50(\pm 0.09) - 0.026(\pm 0.016)R_g/\text{kpc}, \quad (12)$$

with an intrinsic dispersion of $\sigma_{\text{int}} = 0.07 \pm 0.08$ dex. The redetermined gradient is in agreement with the previously reported gradient for the seven H II regions, although the magnitude of the intrinsic scatter is larger than previously reported. This scatter is consistent with $\sigma_{\text{int}} = 0$ dex within uncertainty.

The CHAOS-measured abundance gradient in NGC 2403 agrees with the Berg et al. (2013) redetermined gradient within uncertainty, and the temperatures and oxygen abundances in three of the four overlapping regions agree within uncertainty. We can add the three outer H II regions of Berg et al. (2013), or those that we have not observed, to our data set to increase the radial sampling of the H II regions in NGC 2403. We measure an abundance gradient for this combined data set, totaling 30 H II regions from R_g/R_e of 0.39 to 3.59, of

$$12 + \log(O/H)_{\text{All}} = 8.56(\pm 0.03) - 0.093(\pm 0.017)R_g/R_e, \quad (13)$$

with an intrinsic dispersion about the gradient of $\sigma_{\text{int}} = 0.034 \pm 0.017$ dex. This gradient is consistent with Equations (9) and (11) within statistical uncertainty.

The oxygen abundance determined for the innermost H II region with direct abundances, NGC 2403–14+42, does not agree with the redetermined abundance. For this region, the low-ionization zone temperature measured, 7800 ± 300 K, is significantly lower than the redetermined temperature, 8600 ± 300 K. The difference in the O/H abundances is entirely consistent with the difference in the low-ionization zone temperature: recalculating the abundance within this region using the redetermined low-ionization zone temperature for the O⁺ abundance (keeping all else constant) yields $12 + \log(O/H) = 8.46 \pm 0.07$ dex, in agreement with the redetermined Berg et al. (2013) abundance in this region.

We measure an intrinsic dispersion about the O/H gradient of $\sigma_{\text{int}} = 0.037 \pm 0.017$ dex; this is smaller than the redetermined $\sigma_{\text{int}} = 0.07 \pm 0.08$ dex from the Berg et al. (2013) data and is not consistent with 0 dex within uncertainty. The same

¹³ The angular offsets of the overlapping H II regions disagreed with those reported by Berg et al. (2013). After confirming our H II region locations with a recent study of NGC 2403 by Mao et al. (2018), we update the positions of the Berg et al. (2013) H II regions to be concurrent with the radial distances of our regions.

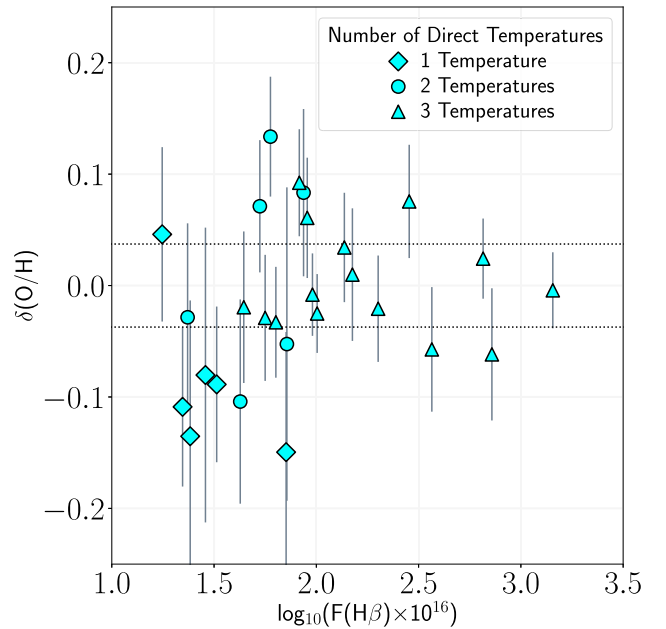


Figure 9. The offset from the O/H gradient in NGC 2403 vs. the observed flux of H β . The intrinsic dispersion about the gradient is represented by the dotted horizontal lines. The number of direct temperatures from the commonly used auroral lines (from [N II], [S III], and [O III]) measured in each region is represented by the different shapes. The regions with the most auroral line detections typically fall within the intrinsic scatter about the abundance gradient of Equation (9), while regions with fewer direct temperatures are more scattered about the gradient.

result is found when using the ionization-based temperature prioritization method; see Table B1 in Appendix B. The sample of H II regions selected might affect the dispersion in the oxygen abundances: Berg et al. (2013) target four bright H II regions within the first ~ 3 kpc and three extended H II regions, while we target many H II regions within ~ 4.5 kpc and very few outer H II regions. The regions we select range from the same bright H II regions of Berg et al. (2013) to a few relatively dim regions that are on the outskirts of the diffuse spiral arms. As mentioned in Section 1, IFU studies have detected abundance enhancement in arm H II regions relative to interarm regions (Ho et al. 2019; Kreckel et al. 2019; Sánchez-Menguiano et al. 2020). If physical processes such as radial mixing are more efficient along the spiral arms of a galaxy, then these processes might be a source of the nonzero scatter in abundances we observe. However, the spiral structure of NGC 2403 is difficult to trace, and a conservative estimate of the number of interarm H II regions results in too few regions to make a statistical comparison between the two populations of H II regions.

To investigate the impact of having more than one temperature measurement, we plot in Figure 9 the offsets from the best-fit abundance gradient, $\delta(O/H)$, versus the flux of H β before accounting for stellar absorption. The dotted lines represent the intrinsic dispersion about the abundance gradient in NGC 2403. The different shapes designate the number of electron temperatures used in the weighted-average ionization zone temperature (same convention as the top panel in Figure 8). There is no clear trend between offset from the abundance gradient and the flux of H β . Fitting the average and standard deviation for each population of H II regions, we find that the H II regions with the most direct temperatures are most consistent with the gradient ($\langle \delta(O/H) \rangle = 0.00$ dex with

Table 3
CHAOS Abundance Fits

y	x	Galaxy	# Reg.	Equation	$\sigma_{\text{int.}}$	$\sigma_{\text{tot.}}$
12 + log(O/H) (dex)	$R_g (R_e^{-1})$	NGC 0628	45	$y = (8.65 \pm 0.05) - (0.09 \pm 0.03) \times x$	0.082 ± 0.015	0.099
		NGC 5194	28	$y = (8.48 \pm 0.10) + (0.03 \pm 0.05) \times x$	0.04 ± 0.02	0.07
		NGC 5457	71	$y = (8.70 \pm 0.04) - (0.172 \pm 0.016) \times x$	0.097 ± 0.013	0.113
		NGC 3184	30	$y = (8.63 \pm 0.15) - (0.14 \pm 0.10) \times x$	0.08 ± 0.03	0.11
		NGC 2403	27	$y = (8.55 \pm 0.04) - (0.09 \pm 0.03) \times x$	0.037 ± 0.017	0.063
log(N/O) (dex)	$R_g (R_e^{-1})$	NGC 0628	45	$y = (-0.49 \pm 0.03) - (0.283 \pm 0.019) \times x$	0.072 ± 0.010	0.075
		NGC 5194	28	$y = (-0.28 \pm 0.06) - (0.15 \pm 0.03) \times x$	0.072 ± 0.015	0.075
		NGC 5457	71	$y = (-0.70 \pm 0.03) - (0.196 \pm 0.017) \times x$	0.110 ± 0.012	0.120
		NGC 3184	30	$y = (-0.34 \pm 0.08) - (0.34 \pm 0.06) \times x$	0.059 ± 0.017	0.076
		NGC 2403	27	$y = (-0.96 \pm 0.05) - (0.17 \pm 0.03) \times x$	0.060 ± 0.018	0.075
log(Ne/O) (dex)	ALL		166	$y = -0.72 \pm 0.11$		
log(S/O) (dex)	ALL		202	$y = -1.42 \pm 0.17$		
log(Ar/O) (dex)	ALL		201	$y = -2.36 \pm 0.13$		

Note. Best-fit equations for the oxygen, nitrogen, and α /O abundances observed in the CHAOS galaxies. The first and second columns are the dependent and independent variables, respectively, used for the equation listed in the fifth column. The galaxy and the number of regions used for the fit are given in the third and fourth columns. The intrinsic and total scatter, both in dex, are listed in the sixth and seventh columns, respectively.

standard deviation $\sigma = 0.04$ dex). The regions with two direct temperatures ($\langle \delta(\text{O/H}) \rangle = 0.02$ dex, $\sigma = 0.08$ dex) or a single direct temperature ($\langle \delta(\text{O/H}) \rangle = -0.08$ dex, $\sigma = 0.06$ dex) contain more scatter about the gradient. The regions with the most auroral line detections have the potential to have the lowest oxygen abundance uncertainty due to the weighted-average approach to the ionization zone temperatures, so it is likely that the best-fit gradient is weighted to these regions.

Fitting the oxygen abundances in the 15 regions with the [N II], [S III], and [O III] auroral line detections, the abundance gradient is measured to be -0.08 ± 0.03 dex/ R_e with an intrinsic scatter of $\sigma_{\text{int.}} = 0.031 \pm 0.018$ dex. The intrinsic dispersion is within the uncertainty of the dispersion about the gradient in Equation (9) and the dispersion about the gradient obtained when using the ionization-based temperature prioritizations (see Table B1). It should be mentioned that this subsample of H II regions may have its own biases (for instance, toward bright H II regions; see Figure 9) and that we are not advocating for the rejection of the regions lacking in all available auroral lines. Instead, this reveals that the regions in which the weighted-average approach should be performing optimally also have a small, but nonzero, intrinsic dispersion about their best-fit gradient. Given these findings, we conclude that the dispersion about the abundance gradient is not a product of the weighted-average temperature prioritization method. Perhaps some component is dependent on the use of single-temperature H II regions, but we do not have the large number of H II regions to examine the true source of the abundance variations in NGC 2403.

5.2. CHAOS O/H Gradients

The bottom panel of Figure 8 plots the oxygen abundances of the four previously reported CHAOS galaxies in addition to the oxygen abundances of NGC 2403 against R_g/R_e . The abundances in the previous galaxies are rederived using the line intensities from Berg et al. (2020), the weighted-average temperature prioritizations, and the ICFs discussed in

Section 4. Plotting these abundances versus R_g/R_e allows for a better comparison to IFU abundance studies. While an IFU survey obtains a much larger number of H II regions and differences between direct and strong-line abundances are to be expected, it is worthwhile to determine if the five CHAOS galaxies have similar oxygen abundance gradients when plotted against R_g/R_e . For clarity, all H II regions (except for NGC2403+88-18) are represented by the same shapes.

Table 3 contains the best-fit gradients and dispersions for the CHAOS galaxies plotted in the bottom panel of Figure 8. NGC 628, NGC 3184, and NGC 2403 have abundance gradients within the uncertainty of the -0.1 ± 0.03 dex/ R_e universal oxygen abundance gradient reported by Sánchez et al. (2014) and Sánchez-Menguiano et al. (2018). The oxygen abundance gradients are slightly shallower than those reported in Berg et al. (2020), which is the result of the increased uncertainty obtained when applying a T_e - T_e relation. The largest change is observed in NGC 5194's oxygen abundance gradient, which is now slightly positive as opposed to negative.

The more significant change in the abundance gradient of NGC 5194 is due to the increased uncertainties on the temperatures and abundances. Croxall et al. (2015) detected no [O III] auroral lines in the H II regions of this galaxy, resulting in an inferred temperature for the high-ionization zone in each region. The increased uncertainty on the inferred temperatures propagates into the uncertainty on the abundances, and large uncertainties on all abundance measurements flatten the best-fit gradient. The new gradient reported here for NGC 5194 is consistent with zero, which is not unexpected for an interacting galaxy (see discussion in Croxall et al. 2015). A flatter gradient consistent with zero is observed even when using the ionization-based temperature prioritizations, as seen in Table B1 in Appendix B, although the best-fit gradient is negative.

The reported oxygen abundance gradient of NGC 5457, which is consistent with other studies (Kennicutt et al. 2003b; Esteban et al. 2020), is steeper than the universal oxygen

abundance gradient observed by the aforementioned IFU studies and, therefore, is an outlier in that regard. It is also notable that, in the five galaxies, the O/H abundance observed at one half-light radius is fairly constant. The O/H abundance at $R_g = R_e$ ranges from $12 + \log(\text{O/H}) = 8.46$ dex in NGC 2403 to $12 + \log(\text{O/H}) = 8.56$ dex in NGC 628.

Another difference between the findings in this study and Berg et al. (2020) is the scatter about the best-fit gradients. Now that the uncertainties on inferred temperatures are larger in magnitude, the uncertainties on the oxygen abundances have increased in the H II regions that are most reliant on single auroral line detections. Additionally, poor detections are weighted less in the calculation of the ionization zone temperatures, which should result in temperatures/ abundances that are close to the true values within a region. Underestimating the uncertainty on oxygen abundances or using imprecise measurements can result in an overestimation of the intrinsic dispersion about the abundance gradient; this artificially larger scatter could be falsely interpreted as real chemical inhomogeneities within the system (see discussion in Esteban et al. 2020). With the appropriately estimated temperatures and uncertainties, it is expected that the fitted dispersion about the best-fit gradient will decrease in the four previously reported CHAOS galaxies. This is the case for NGC 628, NGC 5194, and NGC 3184, but the intrinsic dispersion of NGC 5457 is still within the uncertainty of the previously reported value. The intrinsic dispersion values obtained using the ionization-prioritization temperatures with the updated $T_e - T_e$ relations are consistent with those reported in Table 3 within uncertainty (see Table B2).

All galaxies have σ_{int} significantly above 0 dex. NGC 2403 has the smallest intrinsic dispersion observed in the noninteracting galaxies, and this dispersion is reproduced when examining the subsample of H II regions with [O III], [S III], and [N II] auroral line detections. This analysis is repeated for NGC 5457, which is the only other galaxy with a statistically significant population of H II regions with all three of these auroral lines detected (26 regions). We find that the intrinsic dispersion about the gradient for these regions drops to $\sigma_{\text{int}} = 0.052 \pm 0.018$ dex, still significantly larger than 0 dex. However, the new gradient is shallower (-0.15 ± 0.02 dex/ R_e) on account of the shorter radial coverage of these H II regions: the regions in NGC 5457 with all three auroral line detections span $R_g/R_e = 0.86$ to 3.55 as opposed to the full sample, which covers $R_g/R_e = 0.43$ to 4.58. We do not expect all H II regions to contain each auroral line, especially the high-metallicity central H II regions where [O III] $\lambda 4363$ is difficult to detect. However, this subsample of H II regions in NGC 5457 reveals a scatter that is still significantly greater than zero, and so we can conclude that the nonzero intrinsic dispersions in Table 3 indicate the presence of nonzero abundance variations in these galaxies.

5.3. N/O Relative Abundance Gradient

Nitrogen has both primary and secondary origins (Henry et al. 2000). N/O gradients trace intermediate-mass stars' contribution to secondary N relative to the primary N and O production in high-mass stars. The trend observed in previous CHAOS galaxies is a negative N/O radial gradient with small scatter relative to the scatter observed in O/H. The N/O relative abundances of NGC 2403 from this study and those recalculated from the line intensities of Berg et al. (2013) are

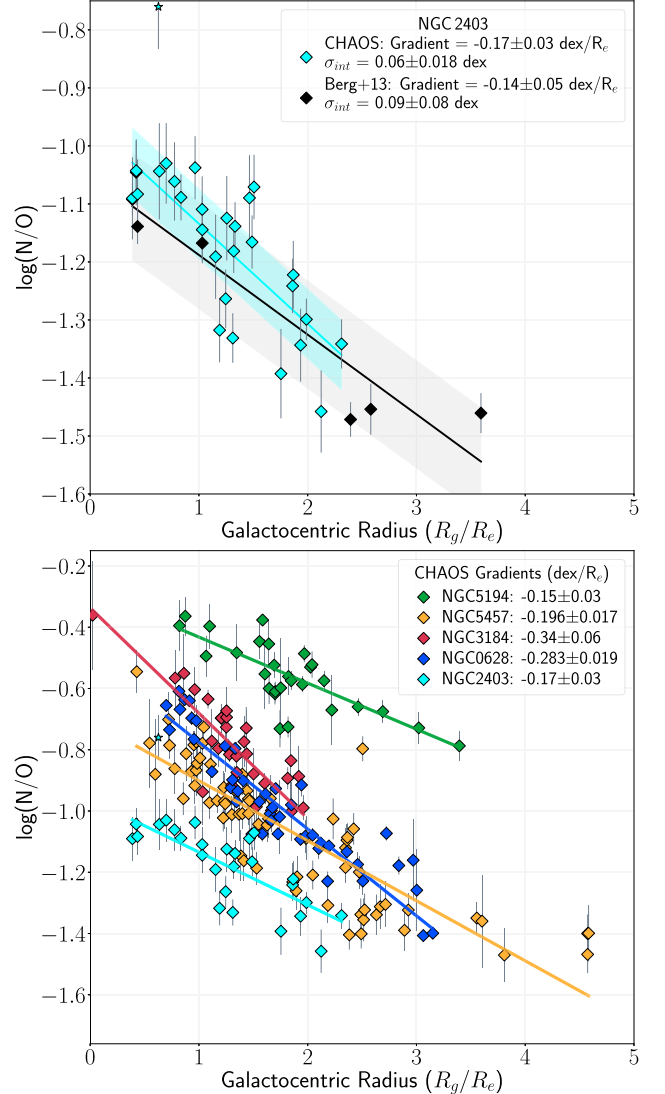


Figure 10. Top panel: CHAOS (cyan) and the recalculated Berg et al. (2013; black) N/O relative abundances in NGC 2403 plotted vs. R_g/R_e . The gradients in each galaxy are plotted as solid lines and are provided in the legend. The intrinsic dispersion about each gradient, represented as the shaded region around each gradient, are also reported in the legend. Bottom panel: same as the top panel but for the N/O relative abundances of all CHAOS galaxies. The shaded portions around each gradient are removed for clarity, and the galaxies listed in the legend are ordered by decreasing stellar mass.

plotted against R_g/R_e in the top panel of Figure 10; the N/O abundances of all CHAOS galaxies are plotted in the bottom panel of this figure. The best-fit N/O gradients in the top panel are consistent within uncertainty:

$$\log(\text{N}/\text{O}) = -0.96(\pm 0.05) - 0.17(\pm 0.03)R_g/R_e \quad (14)$$

$$\log(\text{N}/\text{O})_{B+13} = -1.05(\pm 0.09) - 0.14(\pm 0.05)R_g/R_e. \quad (15)$$

As described in Section 5.1, NGC 2403+88–18, the region represented by a cyan star, is not included in the fit. The intrinsic dispersion about the fits is 0.060 ± 0.018 dex and 0.09 ± 0.08 dex, respectively. Including the outer three H II regions of Berg et al. (2013) in our data set results in a N/O gradient of -0.16 ± 0.02 dex/ R_e , consistent with the above results. Additionally, the N/O abundances of all the overlapping H II regions agree within uncertainty.

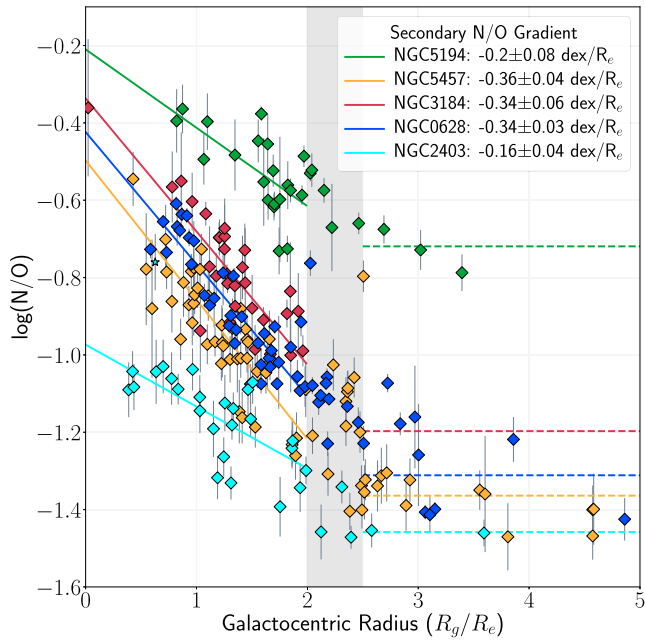


Figure 11. N/O relative abundances in the five CHAOS galaxies plotted vs. R_g/R_e . The secondary N/O gradients in each galaxy are plotted as solid lines from $R_g/R_e = 0$ to 2.0, and the primary N/O plateaus are plotted as dashed lines from $R_g/R_e = 2.5$ and beyond. The secondary N/O gradients are provided in the legend. The gray shaded box indicates the region where the primary N/O transitions to secondary, and the regions within this area are not used in the fits. The secondary N/O gradients of NGC 5457, NGC 3184, and NGC 628 are all consistent, while NGC 2403's secondary N/O gradient is significantly shallower.

The central H II region contains a relative N/O that agrees with the redetermined value, despite having a significantly lower low-ionization zone temperature. The emissivity of [N II] $\lambda 6584$ relative to that of [O II] $\lambda 3727$ is dependent on T_e such that $j_{\text{[N II]} 6584}/j_{\text{[O II]} 3727}$ decreases with increasing T_e . As T_e increases to higher temperatures, the proportional change in the relative emissivities becomes smaller. The difference in the emissivity using the temperature reported here and the temperature redetermined from the previous line intensities is $\sim 20\%$. However, a similar difference in the relative intensities of [N II] $\lambda 6584$ and [O II] $\lambda 3727$ is found when comparing the line intensities measured here (see Table A1) to those in Table 7 of Berg et al. (2013). The net result is an agreement in the relative N/O abundances, while the O/H abundances are discrepant due to the difference in low-ionization zone temperatures.

Berg et al. (2020) found evidence for a universal secondary N/O gradient of $-0.33 \text{ dex}/R_e$ at $R_g/R_e < 2.0$ in noninteracting galaxies, implying that secondary N production dominates at these radii. This result is obtained by fitting the combined N/O abundances at $R_g/R_e < 2.0$ with a single gradient and using the y-intercept or each galaxy's primary N/O plateau at $R_g/R_e > 2.5$ to scale each of the noninteracting galaxies. The most distant H II region that we observe in NGC 2403 is located at $R_g/R_e = 2.31$, but we use the combined data set with the recalculated Berg et al. (2013) N/O abundances in the outer three H II regions to obtain an estimate on the primary N/O plateau in NGC 2403. Figure 11 plots the N/O relative abundances, secondary N/O gradient, and primary N/O plateau in each galaxy. Secondary N/O gradients are obtained using LINMIX. The primary N/O plateaus are calculated using a weighted average of the N/O abundances in the regions at

$R_g/R_e > 2.5$ in each galaxy. The regions found at $2.0 < R_g/R_e < 2.5$ are considered to be in transition from primary to secondary N production and are excluded from the fits. We note that NGC 3184 contains no regions at $R_g/R_e > 2.5$, requiring an extrapolation of this galaxy's secondary N/O gradient to estimate the primary N/O plateau. We also note that Berg et al. (2020) also use the H II regions observed in NGC 628 by Berg et al. (2013) to measure this galaxy's primary N/O plateau. Consistent with our approach to the regions of NGC 2403, we recalculate the N/O abundances in the Berg et al. (2013) regions of NGC 628 using a method consistent with those described in Sections 3 and 4 before combining them with the CHAOS NGC 628 data.

The secondary N/O gradient at $R_g/R_e < 2.0$ in NGC 2403 is

$$\log(\text{N/O})_{\text{Sec}} = -0.97(\pm 0.05) - 0.16(\pm 0.04)R_g/R_e, \quad (16)$$

and the primary N/O is -1.46 dex. If we determine the N/O abundance at $R_g/R_e = 2.5$ via the above equation (similar to the approach taken for NGC 3184), we measure a primary N/O plateau of -1.37 dex, similar to the primary N/O plateau measured in NGC 5457. We do not expect exact agreement among the primary N/O plateaus of the CHAOS galaxies, as primary N and O production is dependent on the star formation history in the galaxy (see discussion in Berg et al. 2020). However, the secondary N/O gradient in NGC 2403 is significantly shallower than the other noninteracting CHAOS galaxies, which indicates that the secondary N production in NGC 2403 is unique in this sample of galaxies. The stellar mass of NGC 2403 is also smaller than the other CHAOS galaxies. The stellar masses for the CHAOS galaxies are $\log(M_*/M_\odot) = 9.6, 10.0, 10.3, 10.4$, and 10.7 for NGC 2403, NGC 628, NGC 3184, NGC 5457, and NGC 5194, respectively.¹⁴ NGC 2403, with its smaller stellar mass, is less chemically evolved, and so secondary nitrogen production has not had time to establish a strong N/O gradient in the galaxy.

The intrinsic dispersion about the observed N/O gradient in NGC 2403 is consistent with the dispersion observed within the other galaxies. The intrinsic dispersions about the best-fit N/O gradients in NGC 5194, NGC 5457, and NGC 3184 have increased from the previous results in Berg et al. (2020). This is because the errors on N/O have decreased for all regions due to the weak dependence of $j_{\text{[N II]} 6584}/j_{\text{[O II]} 3727}$ on the low-ionization zone electron temperature at $T_e > 8000$ K. As such, the dominant source of uncertainty is in the measured fluxes of the strong nebular lines, which is small for the average CHAOS spectrum. Additionally, the single N/O gradient is not an appropriate fit for some of the galaxies; the secondary N/O gradient with a primary N/O plateau provides a better fit to the relative abundances in galaxies like NGC 5457 and NGC 628 (see Figure 11). The dispersion about the N/O gradient in NGC 2403 is dominated by five regions at low N/O relative to the gradient between $R_g/R_e = 1$ and ~ 2 . Interestingly, these regions are found within or near the same diffuse spiral arm.

¹⁴ ZOMGS WISE observations presented in Leroy et al. (2019) are used to obtain the stellar masses. These masses are dependent on the luminosity and, therefore, the adopted distance to each galaxy. We have scaled the stellar masses of each CHAOS galaxy to the distances reported in Table 1 of Berg et al. (2020) and in Table 1.

6. α -element Abundance Trends

Production of different α elements takes place in the same progenitors (high-mass stars), and so it is expected that the relative abundance of these elements is fairly constant at a given metallicity. It is common to compare the relative abundances of α/O to O/H to see if the relative production of an α element varies as a function of metallicity. The Ne/O , S/O , and Ar/O relative abundances of NGC 2403 and the full CHAOS sample versus O/H are plotted in Figure 12. The left column examines the α/O trends observed in NGC 2403 and compares these abundances to the redetermined Berg et al. (2013) α -element abundances. The dashed lines and shaded regions correspond to the weighted average and 1σ uncertainty of each data set, respectively. Additionally, the overlapping regions are connected by solid black lines for easier comparisons between the common H II regions. The right column plots all CHAOS α/O data. In these panels, the blue dotted line is the solar value of the plotted α/O ratio (from Asplund et al. 2009), the light blue shaded box is the uncertainty on the solar average, the black dashed line is the weighted average of the CHAOS data, and the gray box about the CHAOS average is the 1σ error on the average.

We first address the NGC 2403 α -element abundances in the left column. There is generally good agreement between the redetermined α -element abundances from the intensities of Berg et al. (2013) and those determined in this study. The average values determined in NGC 2403 are $\log(\text{Ne}/\text{O})_{\text{avg}} = -0.81 \pm 0.12$ dex, $\log(\text{S}/\text{O})_{\text{avg}} = -1.46 \pm 0.11$ dex, and $\log(\text{Ar}/\text{O})_{\text{avg}} = -2.37 \pm 0.10$ dex. The averages determined for the updated Berg et al. (2013) data are $\log(\text{Ne}/\text{O})_{B+13} = -0.76 \pm 0.07$ dex, $\log(\text{S}/\text{O})_{B+13} = -1.56 \pm 0.10$ dex, and $\log(\text{Ar}/\text{O})_{B+13} = -2.34 \pm 0.05$ dex. Both the average Ne/O and Ar/O values of each sample agree within 0.04 dex, and both samples exhibit no Ne/O trend as a function of metallicity. The Pearson's correlation coefficient for the CHAOS NGC 2403 Ar/O versus O/H data is 0.31 with a p value of 0.10, suggesting that there might be a weak, positive correlation of Ar/O as a function of O/H in these regions. No such trend is observed in the S/O data (Pearson correlation coefficient of 0.09 with a p value of 0.64 for the CHAOS NGC 2403 H II regions). The CHAOS NGC 2403 average S/O is larger than the updated Berg et al. (2013) average S/O by 0.11 dex, almost outside the uncertainties of either average.

When considering the differences in how sulfur abundances are calculated, the discrepancy between $\log(\text{S}/\text{O})_{\text{avg}}$ and $\log(\text{S}/\text{O})_{B+13}$ is not altogether surprising. The source of the discrepancy is the use of the $[\text{S III}]\lambda 6312$ emissivity in the determination of the Berg et al. (2013) S^{2+} abundances. Berg et al. (2013) used the Blue Channel Spectrograph on the MMT to obtain their H II region spectra; this spectrograph has a wavelength cutoff at 6790 Å, which means the strong nebular $[\text{S III}]$ lines are not used for abundance determination. The emissivity of $[\text{S III}]\lambda 6312$ is a strong function of the electron temperature, hence it is useful as a temperature diagnostic. However, this sensitivity, coupled with the use of inferred temperatures from T_e-T_e relations, makes abundances using the emissivity of $[\text{S III}]\lambda 6312$ strongly dependent on the physical conditions within a different ionization zone. The weighted average of the inferred temperatures from the recalculated $T_e[\text{N II}]$ and $T_e[\text{O III}]$ is not enough to resolve the issue of using $[\text{S III}]\lambda 6312$ for S^{2+} abundance determination. Given the wavelength coverage of MODS, we use the strong $[\text{S III}]\lambda\lambda$

9069,9532 nebular lines, corrected to the theoretical ratio if there is evidence of contamination (as described at the beginning of Section 3), for abundance determination. These lines have a weaker dependence on the electron temperature and are at significantly higher S/N than $[\text{S III}]\lambda 6312$.

We now turn our attention to the net α -element abundances in the right column of Figure 12. The solar values are in agreement with the CHAOS weighted averages for all three α elements, within statistical uncertainties. The weak temperature dependence of the relative $[\text{Ne III}]\lambda 3686$ and $[\text{O III}]\lambda 5007$ emissivities result in small uncertainties on the Ne/O relative abundances. This is similar to the small N/O uncertainties discussed in Section 5.3, although the ratio of the $[\text{N II}]\lambda 6584$ and $[\text{O II}]\lambda 3727$ emissivities is a stronger function of T_e at low electron temperatures. The dispersion in $\text{Ne}^{2+}/\text{O}^{2+}$ at low ionization manifests as increased scatter below the best-fit average at intermediate and high metallicity. Despite this dispersion, the average of the CHAOS data agrees with the solar Ne/O . While there is no S/O trend as a function of O/H in the NGC 2403 data, the Pearson correlation coefficient for the net CHAOS data set is 0.46. The evidence for increasing S/O with O/H is primarily found in NGC 5457, although regions with the lowest metallicity do not follow the trend. Additionally, the Pearson correlation coefficient for Ar/O versus O/H is 0.54, indicating that the trend is more evident for all the regions other than just those of NGC 2403. Esteban et al. (2020) find a trend of increasing Ar/O versus O/H in NGC 5457. With the updated temperatures and ICF (which now matches the ICF used by Esteban et al. 2020), the CHAOS data do appear to increase in Ar/O at increasing O/H . The lack of H II regions with $12 + \log(\text{O}/\text{H}) < 8.2$ and the spread in Ar/O in the majority of the H II regions limit our ability to further explore this trend.

7. Conclusions

The CHAOS project has observed nearby, face-on spiral galaxies to build a catalog of high-quality H II region spectra for direct electron temperature measurements. The results of the fifth CHAOS galaxy, NGC 2403, are presented here. With the addition of NGC 2403, the CHAOS database has grown to include 213 H II regions with more than one temperature-sensitive auroral line detection.

With a large database of H II regions with multiple direct temperatures, we create statistically significant empirical T_e-T_e relations to infer electron temperatures in different ionization zones. The Croxall et al. (2016) empirical T_e-T_e relations, developed using the large, homogeneous data set of H II regions in NGC 5457, provide no prescription for estimating errors on the inferred electron temperature nor are the intrinsic dispersions about the relations used. We propose that the intrinsic dispersion in T_e is due to real differences in the physical properties of a H II region that lead to variations in electron temperature within an ionization zone.

The newly measured intrinsic dispersions are used to, partially, account for these unknowns when applying a T_e-T_e relation via the uncertainty on the inferred temperatures. When using an empirical, linear T_e-T_e relation, we propose adding the intrinsic dispersion in quadrature with the uncertainty on the measured temperature to obtain more realistic uncertainties on the inferred electron temperature (see Equation (8)). This sets a minimum uncertainty on inferred electron temperatures, which

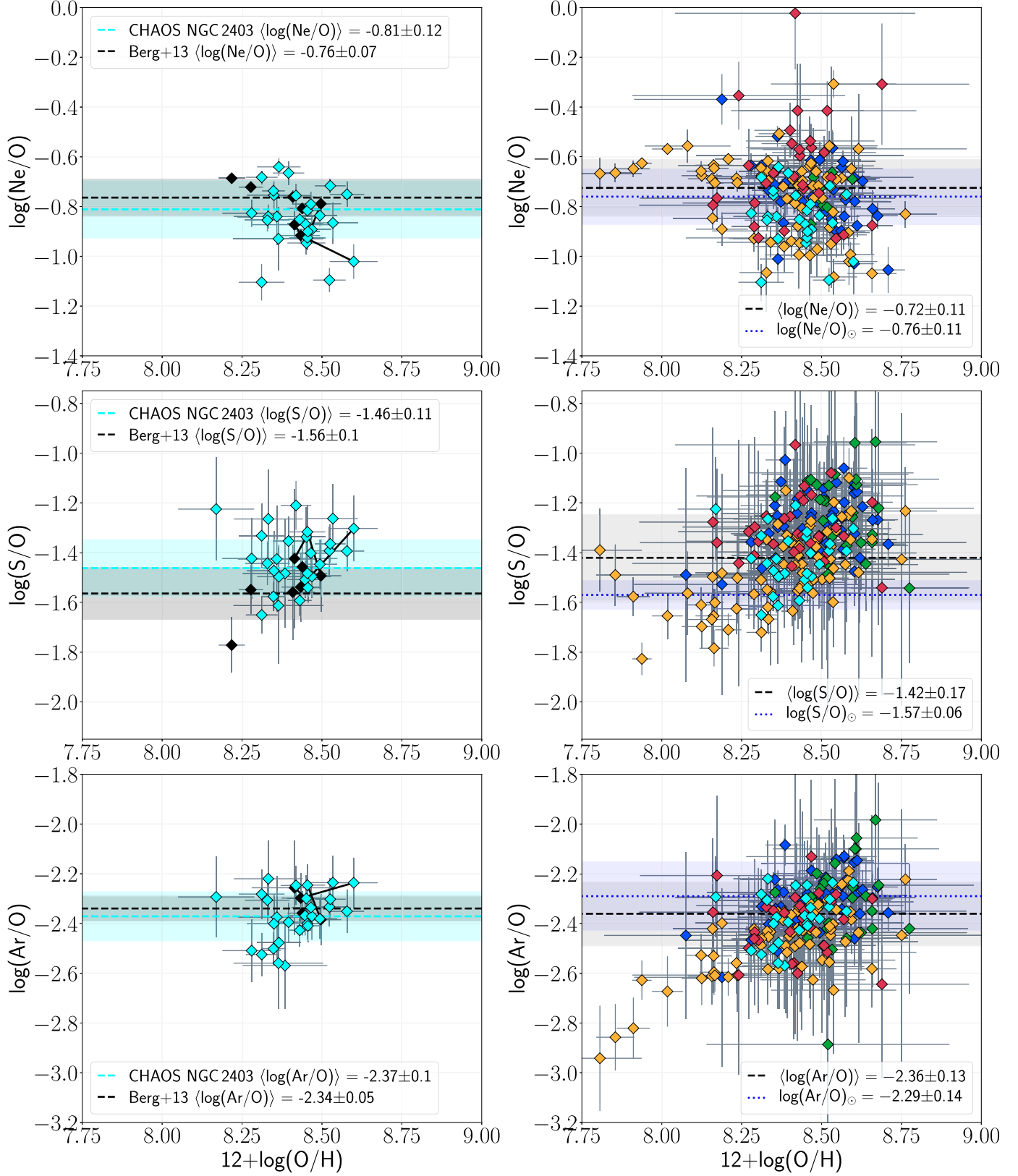


Figure 12. α/O relative abundances of the CHAOS galaxies plotted vs. $12 + \log(O/H)$. Left column: cyan points are α/O abundances in NGC 2403 as observed by CHAOS, while black points are the redetermined α/O relative abundances from Berg et al. (2013). The weighted averages and 1σ uncertainty of each data set are plotted as dashed lines and shaded regions, respectively. The solid black lines connecting some of the CHAOS and Berg et al. (2013) data represent overlapping H II regions. Right column: all CHAOS α/O data for the five galaxies (color-coding same as Figure 3). The black dashed line and the gray shaded portion are the best-fit weighted-average α/O and its 1σ uncertainty, respectively. The dotted blue line and the shaded blue area are the solar α/O value and its uncertainty, respectively, from Asplund et al. (2009).

is appropriate to account for physical differences between ionization zones within a H II region.

With updated temperatures and uncertainties, we recompute the abundances of all H II regions from Berg et al. (2020) along with the 28 H II regions in NGC 2403 with [N II], [S III], or [O III] auroral line detections. We apply a new method to determine the temperatures in each ionization zone: the temperature used is the weighted average of all temperature data in the region, including the dominant ion temperature and inferred ion temperatures when available. The ionization-based temperature prioritizations described in Berg et al. (2020) produce similar results (see Appendix B). The ICFs adopted for abundance determinations are slightly different from those previously applied in other CHAOS studies, as discussed in Section 4. The oxygen abundance gradients of NGC 628, NGC 5457, and NGC 3184 are consistent with those previously reported in Berg et al. (2020), within uncertainty. The new gradient for NGC 5194 is consistent with zero, which is not unexpected for an interacting galaxy.

To compare the results for NGC 2403 to the literature values, we use the line intensities from Berg et al. (2013) and recalculate the temperatures and abundances in a method consistent with the one applied to all CHAOS galaxies. The oxygen abundance gradient in NGC 2403 agrees with the redetermined Berg et al. (2013) gradient. Additionally, the intrinsic dispersion about this gradient is the smallest observed in the sample of five galaxies. The intrinsic dispersion in O/H measured in each CHAOS galaxy is significantly greater than zero, and we associate the dispersion in NGC 2403 with real abundance variations in the galaxy.

The N/O abundances in NGC 2403 agree with the Berg et al. (2013) abundances: all four H II regions that were previously observed have similar N/O, and the N/O gradients agree within uncertainty. The secondary N/O gradient in NGC 2403 is the shallowest of all noninteracting CHAOS galaxies; the low stellar mass of NGC 2403 might indicate that this galaxy has not produced a sufficient amount of secondary nitrogen to establish a steep N/O gradient.

There is agreement between the NGC 2403 Ne/O and Ar/O abundances reported here and recalculated from the Berg et al. (2013) line intensities. The agreement between the S/O abundances is not as clear, but this is due to the different emission lines used for S²⁺ abundance calculation. The α /O best-fit averages for the entire CHAOS data set agree with the solar values, within statistical uncertainty. We observe a possible trend of increasing S/O and Ar/O with O/H in the CHAOS data, a trend that is also reported by Esteban et al. (2020). More H II region abundance data, particularly at low O/H, are needed to verify this trend. With more H II region data, we can begin to develop robust empirical ICFs that

appropriately cover the full range of ionization observed in H II regions and better fit the empirical sulfur, neon, and argon data.

We are grateful to the referee for their insightful comments and thorough feedback, which have substantially improved the clarity and depth of this paper.

This work has been supported by NSF grants AST-1109066 and AST-1714204. This paper uses data taken with the MODS spectrographs built with funding from NSF grant AST-9987045 and the NSF Telescope System Instrumentation Program (TSIP), with additional funds from the Ohio Board of Regents and the Ohio State University Office of Research. This paper made use of the `modsdIDL` spectral data reduction pipeline developed by KVC in part with funds provided by NSF grant AST-1108693. The LBT is an international collaboration among institutions in the United States, Italy, and Germany. LBT Corporation partners are: The University of Arizona on behalf of the Arizona Board of Regents; Istituto Nazionale di Astrofisica, Italy; LBT Beteiligungsgesellschaft, Germany, representing the Max-Planck Society, The Leibniz Institute for Astrophysics Potsdam, and Heidelberg University; The Ohio State University, representing OSU, University of Notre Dame, University of Minnesota, and University of Virginia.

The work of J.S. is partially supported by the National Science Foundation (NSF) under grants No. 1615105, 1615109, and 1653300, as well as by the National Aeronautics and Space Administration (NASA) under ADAP grants NNX16AF48G and NNX17AF39G.

We are grateful to D. Fanning, J. X. Prochaska, J. Hennawi, C. Markwardt, and M. Williams, and others who have developed the IDL libraries of which we have made use: coyote graphics, XIDL, idlutils, MPFIT, MPFITXY, and impro.

This research has made use of the NASA/IPAC Extragalactic Database (NED), which is operated by the Jet Propulsion Laboratory, California Institute of Technology, under contract with the National Aeronautics and Space Administration. This publication makes use of data products from the Two Micron All Sky Survey (2MASS), which is a joint project of the University of Massachusetts and the Infrared Processing and Analysis Center/California Institute of Technology, funded by NASA and the NSF.

Appendix A

NGC 2403 Line Intensities, Temperatures, and Abundances

We report the emission line intensities in the H II regions of NGC 2403 in Table A1. In Table A2, we report the temperatures and abundances within the regions with at least one of the auroral lines from [O III], [S III], or [N II] detected.

Table A1
Emission Line Intensities in NGC 2403

Ion	$I(\lambda)/I(\text{H}\beta)$						
	+19–22	–23–16	–14+42	–38+51	+7+37	–27–28	+56–59
H14 λ 3721	0.014 ± 0.004	0.025 ± 0.003	0.023 ± 0.002	0.020 ± 0.002	0.023 ± 0.002	0.023 ± 0.003	0.014 ± 0.003
[O II] λ 3727	1.591 ± 0.105	2.509 ± 0.178	2.412 ± 0.178	2.030 ± 0.135	2.125 ± 0.147	2.349 ± 0.074	1.712 ± 0.105
H13 λ 3734	0.017 ± 0.005	0.031 ± 0.004	0.029 ± 0.003	0.025 ± 0.002	0.029 ± 0.002	0.028 ± 0.003	0.017 ± 0.004
H12 λ 3750	0.034 ± 0.004	0.033 ± 0.007	0.034 ± 0.003	0.043 ± 0.008	0.041 ± 0.005	0.045 ± 0.007	0.021 ± 0.007
H11 λ 3770	0.032 ± 0.010	0.046 ± 0.009	0.046 ± 0.005	0.049 ± 0.008	0.049 ± 0.004	0.045 ± 0.005	0.019 ± 0.008
H10 λ 3797	0.038 ± 0.011	0.066 ± 0.009	0.062 ± 0.005	0.056 ± 0.005	0.064 ± 0.005	0.062 ± 0.007	0.037 ± 0.008
He I λ 3819	0.011 ± 0.012	0.007 ± 0.010	0.013 ± 0.002	...	0.005 ± 0.003	0.004 ± 0.008	...
H9 λ 3835	0.063 ± 0.012	0.083 ± 0.009	0.079 ± 0.007	0.065 ± 0.006	0.079 ± 0.006	0.087 ± 0.009	0.062 ± 0.007
[Ne III] λ 3868	0.042 ± 0.008	0.017 ± 0.005	0.039 ± 0.004	0.048 ± 0.004	0.051 ± 0.004	0.011 ± 0.007	0.018 ± 0.002
He I λ 3888	0.135 ± 0.015	0.062 ± 0.013	0.066 ± 0.010	0.058 ± 0.011	0.067 ± 0.010	0.060 ± 0.006	0.100 ± 0.009
H8 λ 3889	0.073 ± 0.020	0.127 ± 0.017	0.119 ± 0.010	0.108 ± 0.010	0.125 ± 0.010	0.119 ± 0.014	0.072 ± 0.016
He I λ 3964	0.027 ± 0.007	0.015 ± 0.008	0.013 ± 0.006	...	0.013 ± 0.008	0.010 ± 0.004	0.015 ± 0.006
[Ne III] λ 3967	0.073 ± 0.012	0.004 ± 0.010	0.019 ± 0.004	0.056 ± 0.008
H7 λ 3970	0.108 ± 0.030	0.185 ± 0.026	0.175 ± 0.015	0.161 ± 0.015	0.186 ± 0.015	0.176 ± 0.021	0.108 ± 0.024
[Ne III] λ 4011	...	0.005 ± 0.010	0.006 ± 0.006	...
He I λ 4026	0.013 ± 0.011	0.026 ± 0.010	0.016 ± 0.002	...	0.012 ± 0.005	0.018 ± 0.005	0.000 ± 0.005
[S II] λ 4068	0.009 ± 0.007	0.023 ± 0.010	0.014 ± 0.002	0.007 ± 0.001	0.009 ± 0.001	0.018 ± 0.006	0.009 ± 0.003
[S II] λ 4076	...	0.019 ± 0.007	0.008 ± 0.002	0.004 ± 0.001	0.003 ± 0.001	0.011 ± 0.005	0.004 ± 0.003
H8 λ 4101	0.254 ± 0.020	0.269 ± 0.018	0.265 ± 0.020	0.254 ± 0.017	0.253 ± 0.018	0.257 ± 0.012	0.259 ± 0.014
He I λ 4120	...	0.011 ± 0.009	0.003 ± 0.004	0.001 ± 0.002	0.000 ± 0.001	0.003 ± 0.004	...
He I λ 4143	...	0.008 ± 0.004	0.002 ± 0.002	0.001 ± 0.004	...
C II λ 4267	0.001 ± 0.007	0.015 ± 0.009	0.002 ± 0.002	0.004 ± 0.001	0.004 ± 0.001	0.003 ± 0.004	0.004 ± 0.002
H γ λ 4340	0.493 ± 0.032	0.520 ± 0.030	0.503 ± 0.035	0.486 ± 0.031	0.485 ± 0.032	0.478 ± 0.019	0.471 ± 0.023
[O III] λ 4363	0.005 ± 0.008	0.006 ± 0.006	0.003 ± 0.002	0.006 ± 0.001	0.007 ± 0.001	0.002 ± 0.004	...
He I λ 4387	0.015 ± 0.012	0.008 ± 0.006	0.005 ± 0.002	0.005 ± 0.002	0.005 ± 0.001	0.008 ± 0.004	0.006 ± 0.004
He I λ 4471	0.044 ± 0.009	0.031 ± 0.005	0.043 ± 0.004	0.033 ± 0.004	0.040 ± 0.003	0.022 ± 0.004	0.027 ± 0.003
[Fe III] λ 4658	0.009 ± 0.010	...	0.001 ± 0.001	0.015 ± 0.008	0.008 ± 0.004	...	0.001 ± 0.002
He II λ 4686	0.009 ± 0.012	...	0.006 ± 0.003	0.018 ± 0.011	0.006 ± 0.004	...	0.004 ± 0.002
H β λ 4861	1.000 ± 0.080	1.000 ± 0.074	1.000 ± 0.092	1.000 ± 0.082	1.000 ± 0.085	1.000 ± 0.039	1.000 ± 0.059
He I λ 4921	0.015 ± 0.007	0.009 ± 0.003	0.010 ± 0.001	0.009 ± 0.002	0.010 ± 0.001	0.005 ± 0.003	0.010 ± 0.002
[O III] λ 4959	0.257 ± 0.021	0.211 ± 0.017	0.484 ± 0.046	0.478 ± 0.037	0.475 ± 0.040	0.114 ± 0.005	0.214 ± 0.012
[O III] λ 5007	0.751 ± 0.058	0.661 ± 0.050	1.450 ± 0.142	1.446 ± 0.114	1.429 ± 0.121	0.341 ± 0.014	0.657 ± 0.035
He I λ 5015	0.021 ± 0.015	0.022 ± 0.027	0.025 ± 0.081	0.026 ± 0.052	0.026 ± 0.061	0.014 ± 0.007	0.020 ± 0.011
[N II] λ 5755	0.003 ± 0.004	0.010 ± 0.005	0.004 ± 0.001	0.004 ± 0.001	0.004 ± 0.001	0.006 ± 0.002	0.005 ± 0.002
He I λ 5876	0.116 ± 0.010	0.077 ± 0.011	0.121 ± 0.009	0.110 ± 0.008	0.114 ± 0.008	0.094 ± 0.006	0.105 ± 0.007
[O I] λ 6300	0.027 ± 0.004	...	0.019 ± 0.002	0.013 ± 0.002	0.012 ± 0.002	0.022 ± 0.005	0.012 ± 0.003
[S III] λ 6312	0.006 ± 0.002	...	0.010 ± 0.001	0.010 ± 0.001	0.009 ± 0.001	0.006 ± 0.004	0.004 ± 0.002
[O I] λ 6363	0.004 ± 0.002	...	0.006 ± 0.001	0.004 ± 0.001	0.004 ± 0.001	0.008 ± 0.002	0.002 ± 0.002
[N II] λ 6548	0.217 ± 0.026	0.210 ± 0.021	0.185 ± 0.055	0.168 ± 0.067	0.156 ± 0.037	0.254 ± 0.082	0.172 ± 0.064
H α λ 6563	2.902 ± 0.175	3.095 ± 0.176	3.130 ± 0.215	2.949 ± 0.182	2.952 ± 0.187	2.875 ± 0.100	2.868 ± 0.134
[N II] λ 6584	0.608 ± 0.043	0.684 ± 0.064	0.559 ± 0.045	0.478 ± 0.038	0.455 ± 0.034	0.745 ± 0.050	0.506 ± 0.034
He I λ 6678	0.034 ± 0.003	0.011 ± 0.023	0.033 ± 0.003	0.032 ± 0.003	0.033 ± 0.002	0.028 ± 0.003	0.029 ± 0.002
[S II] λ 6717	0.243 ± 0.015	0.688 ± 0.419	0.230 ± 0.019	0.173 ± 0.013	0.178 ± 0.013	0.393 ± 0.026	0.221 ± 0.015
[S II] λ 6731	0.169 ± 0.011	0.152 ± 0.171	0.167 ± 0.014	0.135 ± 0.011	0.131 ± 0.010	0.284 ± 0.020	0.152 ± 0.012
He I λ 7065	0.023 ± 0.003	0.021 ± 0.010	0.021 ± 0.002	0.022 ± 0.002	0.018 ± 0.001	0.014 ± 0.001	0.013 ± 0.002
[Ar III] λ 7135	0.057 ± 0.004	0.087 ± 0.010	0.101 ± 0.008	0.073 ± 0.005	0.080 ± 0.006	0.053 ± 0.003	0.055 ± 0.003
[O II] λ 7320	0.016 ± 0.003	0.013 ± 0.009	0.022 ± 0.002	0.017 ± 0.001	0.017 ± 0.001	0.015 ± 0.002	0.012 ± 0.003
[O II] λ 7330	0.011 ± 0.003	0.017 ± 0.009	0.016 ± 0.002	0.014 ± 0.001	0.014 ± 0.001	0.011 ± 0.002	0.009 ± 0.003
[Ar III] λ 7751	0.018 ± 0.004	0.025 ± 0.009	0.025 ± 0.002	0.022 ± 0.002	0.024 ± 0.002	0.010 ± 0.002	0.012 ± 0.001
P13 λ 8665	0.017 ± 0.003	0.024 ± 0.012	0.010 ± 0.001	0.012 ± 0.001	0.010 ± 0.001	0.005 ± 0.002	0.010 ± 0.003
P12 λ 8750	0.012 ± 0.004	0.012 ± 0.011	0.013 ± 0.002	0.011 ± 0.001	0.012 ± 0.001	0.012 ± 0.005	0.013 ± 0.008
P11 λ 8862	0.011 ± 0.005	0.007 ± 0.010	0.015 ± 0.001	0.017 ± 0.002	0.015 ± 0.001	0.008 ± 0.002	0.008 ± 0.010
P10 λ 9015	0.018 ± 0.002	0.024 ± 0.009	0.021 ± 0.002	0.020 ± 0.002	0.021 ± 0.002	0.020 ± 0.002	0.024 ± 0.002
[S III] λ 9069	0.199 ± 0.013	0.206 ± 0.014	0.278 ± 0.020	0.215 ± 0.014	0.271 ± 0.018	0.157 ± 0.008	0.220 ± 0.013
P9 λ 9229	0.020 ± 0.002	0.026 ± 0.007	0.030 ± 0.002	0.025 ± 0.002	0.028 ± 0.002	0.021 ± 0.002	0.018 ± 0.003
[S III] λ 9532	0.527 ± 0.035	0.816 ± 0.047	0.895 ± 0.064	0.657 ± 0.043	0.720 ± 0.047	0.552 ± 0.032	0.621 ± 0.039
P8 λ 9546	0.038 ± 0.011	0.040 ± 0.005	0.046 ± 0.009	0.039 ± 0.011	0.042 ± 0.010	0.042 ± 0.012	0.048 ± 0.019
$C(\text{H}\beta)$	0.55 ± 0.03	0.76 ± 0.03	0.66 ± 0.03	0.36 ± 0.03	0.31 ± 0.03	0.52 ± 0.03	0.31 ± 0.03
a_{H}	2.6 ^{+0.3} _{-0.3}	0.0 ^{+1.0} _{-0.0}	0.0 ^{+2.1} _{-0.0}	1.1 ^{+0.2} _{-0.2}	0.8 ^{+0.6} _{-0.6}	0.7 ^{+0.8} _{-0.7}	2.3 ^{+0.3} _{-0.3}
$F_{\text{H}\beta}$	37.98 ± 2.13	20.30 ± 1.06	86.61 ± 5.62	721.68 ± 41.58	367.06 ± 21.83	43.70 ± 1.16	57.65 ± 2.39

Table A1
(Continued)

Ion	$I(\lambda)/I(\text{H}\beta)$						
	+88-18	-97+39	-84-0	-3-71	+119-28	-98-19	-59+118
H14 λ 3721	0.020 \pm 0.002	0.020 \pm 0.003	0.025 \pm 0.004	0.017 \pm 0.002	0.022 \pm 0.002	0.019 \pm 0.002	0.017 \pm 0.001
[O II] λ 3727	1.515 \pm 0.087	2.642 \pm 0.181	2.472 \pm 0.149	1.589 \pm 0.076	2.478 \pm 0.106	2.512 \pm 0.149	1.470 \pm 0.106
H13 λ 3734	0.025 \pm 0.003	0.026 \pm 0.004	0.031 \pm 0.005	0.021 \pm 0.002	0.028 \pm 0.002	0.023 \pm 0.003	0.022 \pm 0.002
H12 λ 3750	0.035 \pm 0.005	0.024 \pm 0.011	0.031 \pm 0.015	0.025 \pm 0.004	0.032 \pm 0.003	0.025 \pm 0.006	0.030 \pm 0.003
H11 λ 3770	0.043 \pm 0.004	0.044 \pm 0.010	0.041 \pm 0.012	0.035 \pm 0.003	0.041 \pm 0.002	0.037 \pm 0.006	0.037 \pm 0.003
H10 λ 3797	0.056 \pm 0.007	0.056 \pm 0.008	0.067 \pm 0.010	0.046 \pm 0.005	0.060 \pm 0.004	0.051 \pm 0.007	0.048 \pm 0.004
He I λ 3819	0.005 \pm 0.006	0.004 \pm 0.003	0.007 \pm 0.002	...	0.007 \pm 0.001
H9 λ 3835	0.084 \pm 0.008	0.064 \pm 0.010	0.066 \pm 0.010	0.073 \pm 0.005	0.081 \pm 0.004	0.059 \pm 0.011	0.068 \pm 0.005
[Ne III] λ 3868	0.006 \pm 0.010	0.038 \pm 0.010	0.084 \pm 0.016	0.053 \pm 0.004	0.083 \pm 0.005	0.002 \pm 0.005	0.079 \pm 0.007
He I λ 3888	0.110 \pm 0.017	0.056 \pm 0.011	0.061 \pm 0.018	0.088 \pm 0.008	0.078 \pm 0.006	0.029 \pm 0.010	0.084 \pm 0.010
H8 λ 3899	0.109 \pm 0.013	0.108 \pm 0.015	0.125 \pm 0.019	0.089 \pm 0.009	0.115 \pm 0.008	0.099 \pm 0.013	0.094 \pm 0.007
He I λ 3964	0.006 \pm 0.005	0.001 \pm 0.010	0.015 \pm 0.011	0.018 \pm 0.005	0.006 \pm 0.004	...	0.011 \pm 0.006
[Ne III] λ 3967	0.020 \pm 0.007	0.036 \pm 0.006	0.025 \pm 0.004	...	0.027 \pm 0.007
H7 λ 3970	0.164 \pm 0.020	0.161 \pm 0.023	0.180 \pm 0.028	0.134 \pm 0.013	0.169 \pm 0.012	0.147 \pm 0.019	0.142 \pm 0.011
[Ne III] λ 4011	...	0.010 \pm 0.005	0.014 \pm 0.141
He I λ 4026	0.008 \pm 0.012	0.023 \pm 0.009	0.018 \pm 0.013	0.006 \pm 0.006	0.015 \pm 0.004	...	0.012 \pm 0.005
[S II] λ 4068	0.027 \pm 0.003	0.014 \pm 0.006	0.030 \pm 0.014	0.008 \pm 0.003	0.016 \pm 0.003	0.016 \pm 0.004	0.008 \pm 0.001
[S II] λ 4076	0.016 \pm 0.003	0.011 \pm 0.005	0.022 \pm 0.011	...	0.005 \pm 0.003	...	0.004 \pm 0.001
H8 λ 4101	0.272 \pm 0.017	0.256 \pm 0.019	0.295 \pm 0.021	0.257 \pm 0.012	0.261 \pm 0.014	0.254 \pm 0.015	0.255 \pm 0.017
He I λ 4120	0.008 \pm 0.005	0.003 \pm 0.003	0.010 \pm 0.006	...	0.001 \pm 0.001	...	0.001 \pm 0.001
He I λ 4143	...	0.003 \pm 0.004	0.016 \pm 0.008	...	0.000 \pm 0.002
C II λ 4267	0.027 \pm 0.015	0.002 \pm 0.002	0.003 \pm 0.001
H γ λ 4340	0.476 \pm 0.026	0.477 \pm 0.032	0.518 \pm 0.027	0.465 \pm 0.019	0.498 \pm 0.022	0.484 \pm 0.026	0.473 \pm 0.030
[O III] λ 4363	0.003 \pm 0.003	0.001 \pm 0.003	0.011 \pm 0.007	0.001 \pm 0.003	0.006 \pm 0.002	0.001 \pm 0.004	0.005 \pm 0.001
He I λ 4387	0.009 \pm 0.003	0.005 \pm 0.007	0.003 \pm 0.006	0.005 \pm 0.004	0.005 \pm 0.001	0.004 \pm 0.005	0.005 \pm 0.001
He I λ 4471	0.041 \pm 0.005	0.026 \pm 0.005	0.042 \pm 0.006	0.033 \pm 0.003	0.042 \pm 0.002	0.015 \pm 0.004	0.042 \pm 0.004
[Fe III] λ 4658	0.049 \pm 0.042	0.003 \pm 0.004	0.001 \pm 0.007	0.005 \pm 0.002	0.001 \pm 0.001	0.002 \pm 0.003	0.004 \pm 0.003
He II λ 4686	0.032 \pm 0.017	0.002 \pm 0.002	0.008 \pm 0.005	0.004 \pm 0.004	0.020 \pm 0.013
H β λ 4861	1.000 \pm 0.066	1.000 \pm 0.087	1.000 \pm 0.066	1.000 \pm 0.043	1.000 \pm 0.051	1.000 \pm 0.065	1.000 \pm 0.083
He I λ 4921	0.023 \pm 0.006	0.007 \pm 0.002	0.007 \pm 0.004	0.013 \pm 0.002	0.012 \pm 0.001	0.002 \pm 0.004	0.012 \pm 0.001
[O III] λ 4959	0.165 \pm 0.018	0.284 \pm 0.027	0.688 \pm 0.044	0.405 \pm 0.017	0.691 \pm 0.031	0.096 \pm 0.006	0.736 \pm 0.061
[O III] λ 5007	0.517 \pm 0.056	0.860 \pm 0.080	2.092 \pm 0.133	1.250 \pm 0.050	2.098 \pm 0.094	0.291 \pm 0.018	2.230 \pm 0.184
He I λ 5015	0.035 \pm 0.047	0.023 \pm 0.029	0.034 \pm 0.064	0.021 \pm 0.017	0.024 \pm 0.008	0.013 \pm 0.008	0.028 \pm 0.057
[N II] λ 5755	0.006 \pm 0.002	0.006 \pm 0.003	0.004 \pm 0.002	0.002 \pm 0.001	0.005 \pm 0.001	0.005 \pm 0.002	0.003 \pm 0.001
He I λ 5876	0.124 \pm 0.019	0.101 \pm 0.008	0.121 \pm 0.007	0.122 \pm 0.007	0.123 \pm 0.006	0.052 \pm 0.004	0.130 \pm 0.009
[O I] λ 6300	0.011 \pm 0.003	0.034 \pm 0.004	0.029 \pm 0.004	0.015 \pm 0.004	0.016 \pm 0.002	0.024 \pm 0.004	0.014 \pm 0.002
[S III] λ 6312	0.007 \pm 0.002	0.010 \pm 0.003	0.014 \pm 0.002	0.008 \pm 0.003	0.013 \pm 0.001	0.006 \pm 0.002	0.011 \pm 0.001
[O I] λ 6363	0.008 \pm 0.002	0.007 \pm 0.003	0.009 \pm 0.002	0.003 \pm 0.002	0.005 \pm 0.001	0.010 \pm 0.001	0.003 \pm 0.001
[N II] λ 6548	0.208 \pm 0.080	0.183 \pm 0.060	0.196 \pm 0.056	0.122 \pm 0.080	0.145 \pm 0.022	0.196 \pm 0.030	0.096 \pm 0.078
H α λ 6563	3.040 \pm 0.156	2.920 \pm 0.190	3.271 \pm 0.167	2.912 \pm 0.107	3.017 \pm 0.126	2.942 \pm 0.149	2.939 \pm 0.182
[N II] λ 6584	0.627 \pm 0.052	0.560 \pm 0.045	0.573 \pm 0.035	0.344 \pm 0.022	0.437 \pm 0.027	0.583 \pm 0.034	0.266 \pm 0.023
He I λ 6678	0.036 \pm 0.006	0.027 \pm 0.002	0.039 \pm 0.003	0.036 \pm 0.003	0.035 \pm 0.002	0.017 \pm 0.002	0.035 \pm 0.003
[S II] λ 6717	0.372 \pm 0.027	0.273 \pm 0.023	0.247 \pm 0.016	0.186 \pm 0.011	0.221 \pm 0.014	0.403 \pm 0.023	0.147 \pm 0.012
[S II] λ 6731	0.265 \pm 0.020	0.196 \pm 0.016	0.195 \pm 0.013	0.129 \pm 0.009	0.167 \pm 0.010	0.280 \pm 0.017	0.104 \pm 0.009
He I λ 7065	0.026 \pm 0.005	0.014 \pm 0.001	0.033 \pm 0.002	0.014 \pm 0.002	0.024 \pm 0.001	0.009 \pm 0.001	0.020 \pm 0.002
[Ar III] λ 7135	0.045 \pm 0.003	0.063 \pm 0.005	0.114 \pm 0.007	0.074 \pm 0.004	0.103 \pm 0.005	0.033 \pm 0.002	0.091 \pm 0.007
[O II] λ 7320	0.015 \pm 0.002	0.023 \pm 0.003	0.035 \pm 0.003	0.015 \pm 0.003	0.024 \pm 0.001	0.018 \pm 0.002	0.017 \pm 0.001
[O II] λ 7330	0.011 \pm 0.001	0.016 \pm 0.002	0.026 \pm 0.003	0.015 \pm 0.003	0.018 \pm 0.001	0.011 \pm 0.002	0.013 \pm 0.001
[Ar III] λ 7751	0.010 \pm 0.002	0.022 \pm 0.004	0.032 \pm 0.003	0.021 \pm 0.003	0.023 \pm 0.002	0.014 \pm 0.002	0.021 \pm 0.002
P13 λ 8665	0.011 \pm 0.001	0.013 \pm 0.003	0.009 \pm 0.001	0.004 \pm 0.003	0.010 \pm 0.001	0.009 \pm 0.002	0.010 \pm 0.001
P12 λ 8750	0.010 \pm 0.003	0.011 \pm 0.004	0.013 \pm 0.003	0.013 \pm 0.005	0.013 \pm 0.002	0.013 \pm 0.002	0.012 \pm 0.001
P11 λ 8862	0.018 \pm 0.004	0.018 \pm 0.004	0.018 \pm 0.001	0.010 \pm 0.005	0.016 \pm 0.001	0.017 \pm 0.002	0.015 \pm 0.002
P10 λ 9015	0.031 \pm 0.003	0.014 \pm 0.002	0.019 \pm 0.001	0.021 \pm 0.003	0.023 \pm 0.001	0.022 \pm 0.003	0.018 \pm 0.001
[S III] λ 9069	0.184 \pm 0.014	0.225 \pm 0.017	0.323 \pm 0.017	0.232 \pm 0.012	0.241 \pm 0.012	0.111 \pm 0.006	0.196 \pm 0.015
P9 λ 9229	0.036 \pm 0.004	0.020 \pm 0.004	0.030 \pm 0.002	0.022 \pm 0.003	0.028 \pm 0.001	0.027 \pm 0.003	0.026 \pm 0.002
[S III] λ 9532	0.267 \pm 0.021	0.562 \pm 0.043	0.914 \pm 0.048	0.150 \pm 0.010	0.561 \pm 0.029	0.405 \pm 0.021	0.615 \pm 0.046
P8 λ 9546	0.064 \pm 0.008	0.039 \pm 0.009	0.046 \pm 0.006	0.032 \pm 0.006	0.058 \pm 0.008	0.031 \pm 0.004	0.038 \pm 0.010
C(H β)	0.25 \pm 0.03	0.41 \pm 0.03	1.16 \pm 0.03	0.26 \pm 0.03	0.65 \pm 0.03	0.42 \pm 0.03	0.16 \pm 0.03
a_{H}	0.0 ^{+0.5} _{-0.0}	1.9 ^{+0.5} _{-0.5}	0.0 ^{+8.2} _{-0.0}	3.8 ^{+0.4} _{-0.4}	0.0 ^{+1.2} _{-0.0}	1.1 ^{+0.2} _{-0.2}	2.4 ^{+0.6} _{-0.6}
F $_{\text{H}\beta}$	39.84 \pm 1.85	24.17 \pm 1.48	17.64 \pm 0.81	71.17 \pm 2.11	56.21 \pm 1.97	28.70 \pm 1.31	150.10 \pm 8.73

Table A1
(Continued)

Ion	$I(\lambda)/I(H\beta)$						
	+96+30	+44+82	+125–142	+166–140	–190+116	+174–24	–99–59
H14 λ 3721	0.019 ± 0.002	0.022 ± 0.002	0.019 ± 0.002	0.021 ± 0.003	0.020 ± 0.002	0.018 ± 0.002	0.022 ± 0.002
[O II] λ 3727	2.384 ± 0.056	2.994 ± 0.216	1.998 ± 0.140	1.997 ± 0.142	1.858 ± 0.063	2.152 ± 0.082	3.315 ± 0.186
H13 λ 3734	0.024 ± 0.002	0.028 ± 0.003	0.023 ± 0.003	0.027 ± 0.003	0.025 ± 0.002	0.023 ± 0.002	0.028 ± 0.002
H12 λ 3750	0.031 ± 0.003	0.038 ± 0.006	0.027 ± 0.003	0.035 ± 0.005	0.030 ± 0.002	0.026 ± 0.003	0.035 ± 0.003
H11 λ 3770	0.035 ± 0.002	0.044 ± 0.004	0.034 ± 0.004	0.039 ± 0.005	0.036 ± 0.002	0.033 ± 0.004	0.044 ± 0.003
H10 λ 3797	0.052 ± 0.004	0.061 ± 0.006	0.051 ± 0.006	0.058 ± 0.007	0.053 ± 0.004	0.050 ± 0.005	0.060 ± 0.004
He I λ 3819	0.005 ± 0.001	0.005 ± 0.003	0.007 ± 0.002	0.006 ± 0.003	0.008 ± 0.002	0.007 ± 0.001	0.007 ± 0.002
H9 λ 3835	0.068 ± 0.002	0.072 ± 0.006	0.072 ± 0.006	0.077 ± 0.007	0.064 ± 0.003	0.064 ± 0.005	0.080 ± 0.005
[Ne III] λ 3868	0.096 ± 0.003	0.032 ± 0.003	0.120 ± 0.009	0.115 ± 0.009	0.102 ± 0.004	0.160 ± 0.007	0.075 ± 0.005
He I λ 3888	0.080 ± 0.003	0.066 ± 0.010	0.089 ± 0.011	0.089 ± 0.011	0.063 ± 0.005	0.097 ± 0.009	0.082 ± 0.009
H8 λ 3899	0.102 ± 0.008	0.117 ± 0.011	0.099 ± 0.012	0.114 ± 0.014	0.103 ± 0.008	0.096 ± 0.010	0.118 ± 0.008
He I λ 3964	0.011 ± 0.001	0.009 ± 0.007	0.019 ± 0.007	0.015 ± 0.008	0.007 ± 0.003	0.036 ± 0.006	0.010 ± 0.006
[Ne III] λ 3967	0.029 ± 0.003	...	0.034 ± 0.008	0.036 ± 0.009	0.019 ± 0.004	0.019 ± 0.007	0.020 ± 0.006
H7 λ 3970	0.151 ± 0.012	0.174 ± 0.017	0.148 ± 0.019	0.170 ± 0.021	0.152 ± 0.012	0.143 ± 0.015	0.175 ± 0.012
[Ne III] λ 4011	0.001 ± 0.001
He I λ 4026	0.010 ± 0.004	0.010 ± 0.006	0.012 ± 0.004	0.006 ± 0.005	0.014 ± 0.003	0.013 ± 0.004	0.016 ± 0.002
[S II] λ 4068	0.015 ± 0.001	0.013 ± 0.001	0.013 ± 0.001	0.010 ± 0.002	0.008 ± 0.001	0.011 ± 0.001	0.018 ± 0.001
[S II] λ 4076	0.005 ± 0.001	0.005 ± 0.001	0.005 ± 0.001	0.003 ± 0.001	0.002 ± 0.001	0.005 ± 0.001	0.005 ± 0.001
H8 λ 4101	0.256 ± 0.011	0.264 ± 0.018	0.255 ± 0.018	0.256 ± 0.018	0.255 ± 0.011	0.255 ± 0.013	0.259 ± 0.015
He I λ 4120	0.001 ± 0.001	0.001 ± 0.001	0.001 ± 0.001	0.002 ± 0.001	0.002 ± 0.001
He I λ 4143	0.000 ± 0.002	...	0.001 ± 0.002
C II λ 4267	0.002 ± 0.001	0.002 ± 0.001	0.000 ± 0.001	...	0.002 ± 0.003	0.001 ± 0.001	0.001 ± 0.001
H γ λ 4340	0.477 ± 0.017	0.493 ± 0.031	0.476 ± 0.031	0.471 ± 0.030	0.477 ± 0.017	0.483 ± 0.020	0.494 ± 0.025
[O III] λ 4363	0.008 ± 0.001	0.005 ± 0.001	0.007 ± 0.001	0.010 ± 0.001	0.008 ± 0.001	0.012 ± 0.001	0.007 ± 0.001
He I λ 4387	0.005 ± 0.001	0.005 ± 0.001	0.005 ± 0.002	0.004 ± 0.001	0.006 ± 0.001	0.005 ± 0.002	0.005 ± 0.001
He I λ 4471	0.037 ± 0.002	0.039 ± 0.003	0.041 ± 0.003	0.039 ± 0.003	0.041 ± 0.002	0.043 ± 0.003	0.040 ± 0.003
[Fe III] λ 4658	0.011 ± 0.003	0.009 ± 0.005	0.003 ± 0.001	0.015 ± 0.008	0.004 ± 0.002	0.002 ± 0.001	0.009 ± 0.003
He II λ 4686	0.008 ± 0.004	0.014 ± 0.009	0.001 ± 0.002	0.014 ± 0.009	...	0.000 ± 0.001	0.003 ± 0.002
H β λ 4861	1.000 ± 0.033	1.000 ± 0.082	1.000 ± 0.086	1.000 ± 0.083	1.000 ± 0.034	1.000 ± 0.046	1.000 ± 0.062
He I λ 4921	0.011 ± 0.001	0.011 ± 0.001	0.011 ± 0.002	0.012 ± 0.001	0.012 ± 0.001	0.011 ± 0.001	0.011 ± 0.002
[O III] λ 4959	0.712 ± 0.023	0.460 ± 0.039	0.801 ± 0.072	0.701 ± 0.058	0.826 ± 0.028	0.918 ± 0.041	0.564 ± 0.037
[O III] λ 5007	2.159 ± 0.070	1.383 ± 0.117	2.419 ± 0.224	2.132 ± 0.180	2.498 ± 0.082	2.781 ± 0.119	1.699 ± 0.108
He I λ 5015	0.026 ± 0.011	0.026 ± 0.061	0.026 ± 0.102	0.027 ± 0.081	0.030 ± 0.019	0.026 ± 0.042	0.026 ± 0.034
[N II] λ 5755	0.004 ± 0.001	0.005 ± 0.001	0.003 ± 0.001	0.003 ± 0.001	0.003 ± 0.001	0.003 ± 0.001	0.005 ± 0.001
He I λ 5876	0.120 ± 0.005	0.114 ± 0.007	0.120 ± 0.009	0.129 ± 0.010	0.119 ± 0.005	0.124 ± 0.007	0.109 ± 0.005
[O I] λ 6300	0.018 ± 0.001	0.015 ± 0.001	0.012 ± 0.002	0.011 ± 0.001	0.011 ± 0.001	0.017 ± 0.003	0.036 ± 0.003
[S III] λ 6312	0.013 ± 0.001	0.012 ± 0.001	0.012 ± 0.001	0.012 ± 0.001	0.013 ± 0.001	0.012 ± 0.002	0.013 ± 0.001
[O I] λ 6363	0.005 ± 0.001	0.006 ± 0.001	0.003 ± 0.001	0.004 ± 0.001	0.004 ± 0.001	0.004 ± 0.001	0.011 ± 0.001
[N II] λ 6548	0.127 ± 0.031	0.160 ± 0.049	0.081 ± 0.048	0.086 ± 0.051	0.100 ± 0.032	0.080 ± 0.036	0.166 ± 0.022
H α λ 6563	2.909 ± 0.092	3.067 ± 0.189	2.934 ± 0.188	2.923 ± 0.183	2.925 ± 0.094	2.920 ± 0.114	2.992 ± 0.145
[N II] λ 6584	0.361 ± 0.020	0.453 ± 0.033	0.248 ± 0.023	0.260 ± 0.021	0.284 ± 0.017	0.246 ± 0.014	0.482 ± 0.034
He I λ 6678	0.035 ± 0.002	0.035 ± 0.003	0.036 ± 0.003	0.040 ± 0.004	0.033 ± 0.002	0.035 ± 0.002	0.034 ± 0.002
[S II] λ 6717	0.190 ± 0.011	0.204 ± 0.014	0.160 ± 0.015	0.182 ± 0.015	0.129 ± 0.007	0.164 ± 0.010	0.345 ± 0.017
[S II] λ 6731	0.151 ± 0.009	0.144 ± 0.010	0.112 ± 0.011	0.133 ± 0.011	0.097 ± 0.005	0.118 ± 0.007	0.247 ± 0.013
He I λ 7065	0.027 ± 0.001	0.020 ± 0.001	0.019 ± 0.002	0.024 ± 0.002	0.020 ± 0.001	0.020 ± 0.001	0.019 ± 0.001
[Ar III] λ 7135	0.091 ± 0.004	0.090 ± 0.006	0.096 ± 0.008	0.091 ± 0.007	0.092 ± 0.004	0.100 ± 0.005	0.092 ± 0.005
[O II] λ 7320	0.028 ± 0.001	0.025 ± 0.002	0.020 ± 0.002	0.020 ± 0.002	0.020 ± 0.001	0.021 ± 0.002	0.031 ± 0.002
[O II] λ 7330	0.022 ± 0.001	0.020 ± 0.002	0.017 ± 0.002	0.017 ± 0.002	0.015 ± 0.001	0.017 ± 0.002	0.024 ± 0.002
[Ar III] λ 7751	0.020 ± 0.001	0.026 ± 0.002	0.026 ± 0.002	0.029 ± 0.003	0.021 ± 0.001	0.026 ± 0.002	0.027 ± 0.002
P13 λ 8665	0.010 ± 0.001	0.012 ± 0.001	0.008 ± 0.001	0.007 ± 0.002	0.008 ± 0.001	0.010 ± 0.001	0.008 ± 0.001
P12 λ 8750	0.012 ± 0.001	0.012 ± 0.001	0.011 ± 0.003	0.009 ± 0.001	0.010 ± 0.001	0.013 ± 0.002	0.009 ± 0.001
P11 λ 8862	0.014 ± 0.001	0.016 ± 0.001	0.019 ± 0.002	0.018 ± 0.001	0.013 ± 0.001	0.016 ± 0.001	0.014 ± 0.001
P10 λ 9015	0.019 ± 0.001	0.024 ± 0.002	0.024 ± 0.002	0.026 ± 0.003	0.016 ± 0.001	0.022 ± 0.001	0.020 ± 0.001
[S III] λ 9069	0.256 ± 0.010	0.308 ± 0.020	0.295 ± 0.023	0.283 ± 0.019	0.223 ± 0.010	0.276 ± 0.013	0.234 ± 0.012
P9 λ 9229	0.025 ± 0.001	0.030 ± 0.002	0.027 ± 0.002	0.028 ± 0.002	0.021 ± 0.001	0.025 ± 0.001	0.028 ± 0.002
[S III] λ 9532	0.536 ± 0.020	0.808 ± 0.052	0.836 ± 0.063	0.807 ± 0.054	0.547 ± 0.025	0.806 ± 0.037	0.651 ± 0.034
P8 λ 9546	0.042 ± 0.006	0.049 ± 0.014	0.049 ± 0.013	0.053 ± 0.014	0.031 ± 0.009	0.048 ± 0.010	0.039 ± 0.011
C(H β)	0.36 ± 0.03	0.44 ± 0.03	0.36 ± 0.03	0.36 ± 0.03	0.55 ± 0.03	0.42 ± 0.03	0.32 ± 0.03
a_H	1.4 ^{+0.7} _{-0.7}	0.0 ^{+0.8} _{-0.0}	3.1 ^{+0.8} _{-0.8}	2.3 ^{+0.4} _{-0.4}	3.4 ^{+1.1} _{-1.1}	0.7 ^{+0.8} _{-0.7}	0.0 ^{+1.2} _{-0.0}
F $H\beta$	1432.56 ± 31.88	284.50 ± 16.28	59.66 ± 3.59	200.57 ± 11.74	95.74 ± 2.18	82.56 ± 2.62	90.30 ± 3.88

Table A1
(Continued)

Ion	$I(\lambda)/I(\text{H}\beta)$						
	-196+58	-194+165	-89+171	-146-38	+201-24	+178-210	-22-162
H14 λ 3721	0.019 \pm 0.001	0.016 \pm 0.002	0.020 \pm 0.002	0.019 \pm 0.001	0.026 \pm 0.003	0.019 \pm 0.003	0.021 \pm 0.003
[O II] λ 3727	1.909 \pm 0.077	2.139 \pm 0.059	2.114 \pm 0.114	2.684 \pm 0.128	2.661 \pm 0.091	2.065 \pm 0.142	3.634 \pm 0.151
H13 λ 3734	0.024 \pm 0.002	0.020 \pm 0.003	0.025 \pm 0.002	0.024 \pm 0.001	0.032 \pm 0.004	0.024 \pm 0.004	0.026 \pm 0.003
H12 λ 3750	0.029 \pm 0.002	0.029 \pm 0.011	0.031 \pm 0.005	0.031 \pm 0.008	0.072 \pm 0.010	0.030 \pm 0.006	0.038 \pm 0.005
H11 λ 3770	0.036 \pm 0.002	0.030 \pm 0.010	0.042 \pm 0.005	0.046 \pm 0.006	0.066 \pm 0.012	0.039 \pm 0.006	0.045 \pm 0.004
H10 λ 3797	0.053 \pm 0.004	0.044 \pm 0.007	0.054 \pm 0.005	0.053 \pm 0.003	0.070 \pm 0.008	0.053 \pm 0.008	0.057 \pm 0.007
He I λ 3819	0.007 \pm 0.001	0.009 \pm 0.005	0.004 \pm 0.002	...	0.001 \pm 0.012	0.004 \pm 0.003	0.007 \pm 0.004
H9 λ 3835	0.064 \pm 0.003	0.051 \pm 0.006	0.074 \pm 0.005	0.056 \pm 0.006	0.091 \pm 0.009	0.077 \pm 0.007	0.077 \pm 0.005
[Ne III] λ 3868	0.077 \pm 0.004	0.038 \pm 0.006	0.089 \pm 0.006	0.015 \pm 0.005	0.033 \pm 0.010	0.106 \pm 0.008	0.131 \pm 0.007
He I λ 3888	0.069 \pm 0.006	0.058 \pm 0.008	0.085 \pm 0.008	0.080 \pm 0.011	0.095 \pm 0.011	0.094 \pm 0.013	0.087 \pm 0.010
H8 λ 3899	0.104 \pm 0.008	0.086 \pm 0.013	0.104 \pm 0.010	0.103 \pm 0.006	0.136 \pm 0.015	0.103 \pm 0.016	0.111 \pm 0.013
He I λ 3964	0.009 \pm 0.004	0.005 \pm 0.004	0.014 \pm 0.006	...	0.012 \pm 0.010	0.034 \pm 0.009	0.009 \pm 0.004
[Ne III] λ 3967	0.014 \pm 0.004	0.009 \pm 0.004	0.035 \pm 0.006	0.026 \pm 0.009	0.048 \pm 0.005
H7 λ 3970	0.155 \pm 0.012	0.127 \pm 0.019	0.154 \pm 0.015	0.153 \pm 0.009	0.204 \pm 0.023	0.154 \pm 0.024	0.164 \pm 0.020
[Ne III] λ 4011	...	0.004 \pm 0.007	0.012 \pm 0.007
He I λ 4026	0.011 \pm 0.003	0.008 \pm 0.006	0.017 \pm 0.003	...	0.008 \pm 0.010	0.008 \pm 0.004	0.009 \pm 0.008
[S II] λ 4068	0.009 \pm 0.001	0.008 \pm 0.004	0.013 \pm 0.002	0.013 \pm 0.003	0.023 \pm 0.007	0.011 \pm 0.002	0.024 \pm 0.004
[S II] λ 4076	0.003 \pm 0.001	...	0.004 \pm 0.003	0.001 \pm 0.007	0.010 \pm 0.007	0.004 \pm 0.002	0.007 \pm 0.002
H8 λ 4101	0.257 \pm 0.012	0.258 \pm 0.012	0.254 \pm 0.014	0.260 \pm 0.014	0.257 \pm 0.012	0.256 \pm 0.018	0.257 \pm 0.013
He I λ 4120	0.001 \pm 0.001	0.003 \pm 0.003	0.002 \pm 0.003	0.004 \pm 0.003	0.012 \pm 0.007
He I λ 4143
C II λ 4267	0.002 \pm 0.004	0.001 \pm 0.005	0.001 \pm 0.009	0.002 \pm 0.001	...
H γ λ 4340	0.471 \pm 0.018	0.464 \pm 0.017	0.490 \pm 0.023	0.469 \pm 0.020	0.481 \pm 0.020	0.475 \pm 0.031	0.476 \pm 0.019
[O III] λ 4363	0.007 \pm 0.001	0.002 \pm 0.003	0.004 \pm 0.003	0.006 \pm 0.002	0.000 \pm 0.006	0.009 \pm 0.002	0.009 \pm 0.002
He I λ 4387	0.005 \pm 0.001	0.006 \pm 0.005	0.005 \pm 0.002	0.005 \pm 0.004	0.001 \pm 0.005	0.004 \pm 0.002	0.001 \pm 0.002
He I λ 4471	0.040 \pm 0.002	0.036 \pm 0.004	0.038 \pm 0.003	0.027 \pm 0.004	0.037 \pm 0.009	0.035 \pm 0.003	0.032 \pm 0.003
[Fe III] λ 4658	0.005 \pm 0.001	...	0.003 \pm 0.002	0.008 \pm 0.005	0.010 \pm 0.006	0.002 \pm 0.001	0.033 \pm 0.025
He II λ 4686	0.006 \pm 0.004	0.040 \pm 0.011	0.008 \pm 0.006	0.001 \pm 0.001	0.020 \pm 0.016
H β λ 4861	1.000 \pm 0.040	1.000 \pm 0.035	1.000 \pm 0.055	1.000 \pm 0.046	1.000 \pm 0.037	1.000 \pm 0.086	1.000 \pm 0.044
He I λ 4921	0.011 \pm 0.001	0.010 \pm 0.002	0.012 \pm 0.002	0.016 \pm 0.004	0.015 \pm 0.004	0.010 \pm 0.002	0.011 \pm 0.001
[O III] λ 4959	0.715 \pm 0.028	0.517 \pm 0.019	0.680 \pm 0.035	0.144 \pm 0.007	0.464 \pm 0.019	0.733 \pm 0.062	0.591 \pm 0.028
[O III] λ 5007	2.160 \pm 0.084	1.542 \pm 0.055	2.035 \pm 0.104	0.427 \pm 0.020	1.391 \pm 0.051	2.211 \pm 0.188	1.792 \pm 0.083
He I λ 5015	0.028 \pm 0.029	0.020 \pm 0.021	0.027 \pm 0.035	0.021 \pm 0.011	0.026 \pm 0.016	0.025 \pm 0.078	0.025 \pm 0.042
[N II] λ 5755	0.003 \pm 0.001	0.006 \pm 0.002	0.004 \pm 0.002	0.004 \pm 0.001	0.001 \pm 0.006	0.001 \pm 0.001	0.005 \pm 0.002
He I λ 5876	0.117 \pm 0.005	0.097 \pm 0.005	0.118 \pm 0.007	0.090 \pm 0.006	0.122 \pm 0.009	0.111 \pm 0.008	0.116 \pm 0.007
[O I] λ 6300	0.012 \pm 0.001	0.012 \pm 0.002	0.005 \pm 0.003	0.014 \pm 0.004	0.051 \pm 0.009	0.014 \pm 0.002	0.023 \pm 0.003
[S III] λ 6312	0.011 \pm 0.001	0.012 \pm 0.002	0.011 \pm 0.001	0.007 \pm 0.002	0.011 \pm 0.005	0.011 \pm 0.001	0.015 \pm 0.002
[O I] λ 6363	0.004 \pm 0.001	0.001 \pm 0.002	0.004 \pm 0.001	0.006 \pm 0.001	0.012 \pm 0.008	0.005 \pm 0.001	0.008 \pm 0.002
[N II] λ 6548	0.123 \pm 0.066	0.130 \pm 0.040	0.106 \pm 0.054	0.195 \pm 0.025	0.106 \pm 0.037	0.067 \pm 0.022	0.136 \pm 0.078
H α λ 6563	2.902 \pm 0.102	2.889 \pm 0.094	2.928 \pm 0.130	2.909 \pm 0.113	2.879 \pm 0.097	2.924 \pm 0.188	2.881 \pm 0.108
[N II] λ 6584	0.315 \pm 0.023	0.364 \pm 0.023	0.304 \pm 0.021	0.432 \pm 0.038	0.297 \pm 0.013	0.209 \pm 0.015	0.394 \pm 0.024
He I λ 6678	0.034 \pm 0.002	0.033 \pm 0.003	0.033 \pm 0.002	0.030 \pm 0.004	0.036 \pm 0.003	0.035 \pm 0.003	0.034 \pm 0.002
[S II] λ 6717	0.150 \pm 0.008	0.193 \pm 0.011	0.174 \pm 0.011	0.243 \pm 0.011	0.234 \pm 0.010	0.128 \pm 0.009	0.331 \pm 0.019
[S II] λ 6731	0.110 \pm 0.006	0.143 \pm 0.008	0.123 \pm 0.009	0.166 \pm 0.008	0.158 \pm 0.009	0.094 \pm 0.007	0.241 \pm 0.016
He I λ 7065	0.019 \pm 0.001	0.017 \pm 0.001	0.017 \pm 0.001	0.018 \pm 0.002	0.023 \pm 0.005	0.018 \pm 0.001	0.018 \pm 0.001
[Ar III] λ 7135	0.086 \pm 0.004	0.082 \pm 0.004	0.088 \pm 0.005	0.038 \pm 0.002	0.082 \pm 0.011	0.087 \pm 0.006	0.079 \pm 0.004
[O II] λ 7320	0.018 \pm 0.001	0.025 \pm 0.002	0.017 \pm 0.001	0.021 \pm 0.002	0.029 \pm 0.009	0.026 \pm 0.003	0.030 \pm 0.002
[O II] λ 7330	0.015 \pm 0.001	0.021 \pm 0.003	0.013 \pm 0.002	0.014 \pm 0.002	0.021 \pm 0.013	0.023 \pm 0.003	0.024 \pm 0.003
[Ar III] λ 7751	0.021 \pm 0.001	0.015 \pm 0.002	0.018 \pm 0.002	0.013 \pm 0.003	0.023 \pm 0.008	0.026 \pm 0.003	0.023 \pm 0.003
P13 λ 8665	0.009 \pm 0.001	0.008 \pm 0.002	0.010 \pm 0.001	0.016 \pm 0.001	0.008 \pm 0.005	0.007 \pm 0.002	0.009 \pm 0.002
P12 λ 8750	0.009 \pm 0.001	0.011 \pm 0.002	0.012 \pm 0.003	0.010 \pm 0.005	0.009 \pm 0.020	0.015 \pm 0.006	0.010 \pm 0.006
P11 λ 8862	0.013 \pm 0.001	0.012 \pm 0.002	0.015 \pm 0.001	0.015 \pm 0.003	0.023 \pm 0.012	0.016 \pm 0.004	0.020 \pm 0.001
P10 λ 9015	0.013 \pm 0.001	0.016 \pm 0.002	0.015 \pm 0.001	0.016 \pm 0.002	0.025 \pm 0.006	0.022 \pm 0.002	0.019 \pm 0.001
[S III] λ 9069	0.225 \pm 0.010	0.239 \pm 0.012	0.197 \pm 0.012	0.142 \pm 0.006	0.140 \pm 0.008	0.277 \pm 0.018	0.214 \pm 0.011
P9 λ 9229	0.022 \pm 0.001	0.025 \pm 0.001	0.025 \pm 0.002	0.019 \pm 0.002	0.019 \pm 0.005	0.027 \pm 0.003	0.022 \pm 0.002
[S III] λ 9532	0.557 \pm 0.024	0.584 \pm 0.031	0.514 \pm 0.031	0.349 \pm 0.016	0.566 \pm 0.025	0.674 \pm 0.044	0.307 \pm 0.014
P8 λ 9546	0.035 \pm 0.006	0.037 \pm 0.012	0.036 \pm 0.007	0.038 \pm 0.005	0.043 \pm 0.024	0.036 \pm 0.006	0.048 \pm 0.003
C(H β)	0.28 \pm 0.03	0.43 \pm 0.03	0.52 \pm 0.03	0.37 \pm 0.03	0.28 \pm 0.03	0.28 \pm 0.03	0.39 \pm 0.03
a_{H}	3.9 ^{+0.9} _{-0.9}	7.0 ^{+1.1} _{-1.1}	1.9 ^{+1.1} _{-1.1}	0.0 ^{+0.3} _{-0.0}	0.1 ^{+0.4} _{-0.1}	2.1 ^{+0.4} _{-0.4}	1.5 ^{+1.0} _{-1.0}
F $_{\text{H}\beta}$	653.78 \pm 17.96	22.19 \pm 0.52	32.57 \pm 1.24	71.78 \pm 2.28	14.21 \pm 0.36	52.95 \pm 3.21	44.19 \pm 1.32

Table A1
(Continued)

Ion	$I(\lambda)/I(H\beta)$				
	+92–210	+43–200	–14+192	+160–251	–18+224
H ₁₄ λ 3721	0.024 ± 0.004	0.023 ± 0.003	0.020 ± 0.002	0.029 ± 0.004	0.022 ± 0.002
[O II] λ 3727	3.070 ± 0.185	2.984 ± 0.200	2.858 ± 0.111	2.836 ± 0.204	2.579 ± 0.070
H ₁₃ λ 3734	0.029 ± 0.004	0.028 ± 0.003	0.025 ± 0.002	0.036 ± 0.004	0.027 ± 0.003
H ₁₂ λ 3750	0.039 ± 0.008	0.041 ± 0.010	0.030 ± 0.002	0.042 ± 0.006	0.030 ± 0.003
H ₁₁ λ 3770	0.044 ± 0.007	0.047 ± 0.009	0.037 ± 0.003	0.051 ± 0.006	0.043 ± 0.004
H ₁₀ λ 3797	0.064 ± 0.010	0.062 ± 0.007	0.054 ± 0.005	0.078 ± 0.010	0.059 ± 0.006
H _e I λ 3819	...	0.009 ± 0.005	0.008 ± 0.002	0.008 ± 0.002	0.010 ± 0.002
H ₉ λ 3835	0.084 ± 0.007	0.088 ± 0.008	0.067 ± 0.005	0.095 ± 0.011	0.072 ± 0.004
[Ne III] λ 3868	0.054 ± 0.005	0.124 ± 0.011	0.161 ± 0.008	0.230 ± 0.017	0.202 ± 0.009
He I λ 3888	0.078 ± 0.012	0.103 ± 0.014	0.076 ± 0.007	0.086 ± 0.027	0.079 ± 0.005
H ₈ λ 3889	0.125 ± 0.019	0.120 ± 0.014	0.106 ± 0.010	0.152 ± 0.019	0.116 ± 0.012
He I λ 3964	0.002 ± 0.006	0.021 ± 0.009	0.006 ± 0.004	0.012 ± 0.014	0.002 ± 0.002
[Ne III] λ 3967	0.012 ± 0.007	0.041 ± 0.009	0.042 ± 0.005	0.038 ± 0.014	0.044 ± 0.003
H ₇ λ 3970	0.186 ± 0.028	0.177 ± 0.020	0.157 ± 0.014	0.227 ± 0.028	0.172 ± 0.018
[Ne III] λ 4011	...	0.001 ± 0.005
He I λ 4026	...	0.018 ± 0.004	0.013 ± 0.003	0.014 ± 0.003	0.014 ± 0.005
[S II] λ 4068	0.028 ± 0.003	0.017 ± 0.005	0.016 ± 0.001	0.017 ± 0.002	0.014 ± 0.002
[S II] λ 4076	0.007 ± 0.002	0.007 ± 0.005	0.005 ± 0.001	0.006 ± 0.001	0.007 ± 0.002
H _δ λ 4101	0.262 ± 0.017	0.262 ± 0.018	0.257 ± 0.013	0.261 ± 0.018	0.256 ± 0.012
He I λ 4120	...	0.004 ± 0.004	0.001 ± 0.001	0.000 ± 0.002	0.002 ± 0.003
H _e I λ 4143	0.001 ± 0.001	0.001 ± 0.002	0.000 ± 0.003
C II λ 4267	...	0.006 ± 0.005	0.000 ± 0.001	0.004 ± 0.001	0.003 ± 0.002
H _γ λ 4340	0.470 ± 0.027	0.487 ± 0.030	0.497 ± 0.021	0.484 ± 0.030	0.498 ± 0.019
[O III] λ 4363	0.004 ± 0.002	0.013 ± 0.004	0.016 ± 0.001	0.026 ± 0.003	0.018 ± 0.002
He I λ 4387	0.004 ± 0.004	0.008 ± 0.003	0.006 ± 0.001	0.004 ± 0.003	0.008 ± 0.002
He I λ 4471	0.032 ± 0.003	0.042 ± 0.004	0.039 ± 0.002	0.036 ± 0.003	0.041 ± 0.002
[Fe III] λ 4658	0.002 ± 0.003	0.003 ± 0.003	0.002 ± 0.001	0.002 ± 0.002	0.001 ± 0.002
He II λ 4686	0.001 ± 0.002	...	0.001 ± 0.001	0.015 ± 0.003	...
H _β λ 4861	1.000 ± 0.071	1.000 ± 0.079	1.000 ± 0.046	1.000 ± 0.079	1.000 ± 0.039
He I λ 4921	0.009 ± 0.002	0.009 ± 0.003	0.010 ± 0.001	0.009 ± 0.001	0.011 ± 0.002
[O III] λ 4959	0.374 ± 0.028	0.726 ± 0.060	0.905 ± 0.041	1.049 ± 0.088	0.997 ± 0.041
[O III] λ 5007	1.122 ± 0.084	2.195 ± 0.181	2.731 ± 0.129	3.160 ± 0.261	2.994 ± 0.124
He I λ 5015	0.021 ± 0.043	0.026 ± 0.054	0.027 ± 0.061	0.028 ± 0.082	0.023 ± 0.060
[N II] λ 5755	0.005 ± 0.001	0.011 ± 0.004	0.004 ± 0.001	0.003 ± 0.001	0.003 ± 0.001
He I λ 5876	0.101 ± 0.008	0.121 ± 0.011	0.109 ± 0.005	0.109 ± 0.007	0.117 ± 0.005
[O I] λ 6300	0.140 ± 0.009	0.024 ± 0.004	0.021 ± 0.002	0.028 ± 0.002	0.025 ± 0.006
[S III] λ 6312	0.010 ± 0.002	0.014 ± 0.003	0.015 ± 0.001	0.015 ± 0.001	0.014 ± 0.002
[O I] λ 6363	0.044 ± 0.003	0.008 ± 0.002	0.005 ± 0.001	0.009 ± 0.001	0.009 ± 0.001
[N II] λ 6548	0.123 ± 0.049	0.093 ± 0.068	0.089 ± 0.051	0.069 ± 0.020	0.071 ± 0.048
H _α λ 6563	2.927 ± 0.159	2.960 ± 0.177	2.930 ± 0.114	2.976 ± 0.178	2.908 ± 0.101
[N II] λ 6584	0.361 ± 0.024	0.262 ± 0.022	0.263 ± 0.015	0.204 ± 0.017	0.207 ± 0.011
He I λ 6678	0.025 ± 0.002	0.034 ± 0.003	0.030 ± 0.002	0.033 ± 0.002	0.031 ± 0.001
[S II] λ 6717	0.492 ± 0.030	0.188 ± 0.015	0.206 ± 0.011	0.201 ± 0.014	0.198 ± 0.009
[S II] λ 6731	0.352 ± 0.022	0.134 ± 0.011	0.146 ± 0.009	0.143 ± 0.011	0.140 ± 0.007
He I λ 7065	0.015 ± 0.001	0.020 ± 0.002	0.017 ± 0.001	0.020 ± 0.001	0.019 ± 0.001
[Ar III] λ 7135	0.052 ± 0.004	0.089 ± 0.007	0.080 ± 0.004	0.085 ± 0.005	0.078 ± 0.003
[O II] λ 7320	0.033 ± 0.003	0.024 ± 0.003	0.030 ± 0.002	0.030 ± 0.002	0.024 ± 0.002
[O II] λ 7330	0.024 ± 0.003	0.018 ± 0.003	0.023 ± 0.002	0.026 ± 0.002	0.020 ± 0.001
[Ar III] λ 7751	0.025 ± 0.003	0.028 ± 0.004	0.019 ± 0.001	0.022 ± 0.002	0.018 ± 0.002
P ₁₃ λ 8665	0.008 ± 0.001	0.010 ± 0.002	0.007 ± 0.001	0.009 ± 0.001	0.010 ± 0.001
P ₁₂ λ 8750	0.007 ± 0.007	0.010 ± 0.004	0.010 ± 0.001	0.017 ± 0.002	0.009 ± 0.002
P ₁₁ λ 8862	0.013 ± 0.002	0.026 ± 0.004	0.016 ± 0.001	0.016 ± 0.002	0.015 ± 0.001
P ₁₀ λ 9015	0.018 ± 0.002	0.019 ± 0.002	0.018 ± 0.001	0.022 ± 0.002	0.017 ± 0.002
[S III] λ 9069	0.139 ± 0.008	0.223 ± 0.016	0.172 ± 0.008	0.245 ± 0.015	0.128 ± 0.005
P ₉ λ 9229	0.021 ± 0.002	0.025 ± 0.003	0.024 ± 0.001	0.023 ± 0.002	0.023 ± 0.001
[S III] λ 9532	0.429 ± 0.025	0.142 ± 0.010	0.505 ± 0.024	0.718 ± 0.046	0.427 ± 0.017
P ₈ λ 9546	0.050 ± 0.009	0.037 ± 0.007	0.037 ± 0.007	0.037 ± 0.013	0.027 ± 0.006
C(H β)	0.40 ± 0.03	0.51 ± 0.03	0.41 ± 0.03	0.33 ± 0.03	0.39 ± 0.03
a_H	0.0 $^{+0.4}_{-0.0}$	0.0 $^{+0.9}_{-0.0}$	0.0 $^{+1.3}_{-0.0}$	0.0 $^{+0.9}_{-0.0}$	0.0 $^{+0.9}_{-0.0}$
F _{Hβ}	42.47 ± 2.10	23.48 ± 1.30	100.92 ± 3.20	137.10 ± 7.59	63.41 ± 1.69

Note. The reddening-corrected line intensities in the H II regions of NGC 2403. These intensities are relative to $I(H\beta)$. $C(H\beta)$, a_H (in Å), and the flux of $H\beta$ before correction for stellar absorption (in 10^{-16} ergs s^{-1} cm^{-2}) are provided in the last three rows.

(This table is available in machine-readable form.)

Table A2
Temperatures, Ionic, and Total Abundances in NGC 2403

Property	-14+42	-38+51	+7+37	+88-18	-97+39	-84-0	-3-71
$T_e[\text{SII}]$ (K)	10500 ± 1100	8000 ± 800	8500 ± 500	12000 ± 1200
$T_e[\text{NII}]$ (K)	7700 ± 700	7900 ± 300	8000 ± 300
$T_e[\text{OII}]$ (K)	9500 ± 500	9500 ± 400	9300 ± 400	10100 ± 600	9300 ± 500	12500 ± 700	10700 ± 1100
$T_e[\text{SIII}]$ (K)	7300 ± 300	7900 ± 400	7600 ± 300	8200 ± 900	8500 ± 1000	8000 ± 400	8000 ± 800
$T_e[\text{O III}]$ (K)	...	8800 ± 300	9200 ± 400
n_e (cm^{-3})	50 ± 100	120 ± 120	60 ± 100	30 ± 80	40 ± 110	130 ± 100	10 ± 70
$T_{e,\text{low}}$ (K)	7800 ± 300	8100 ± 300	8100 ± 300	8500 ± 600	8700 ± 700	8300 ± 300	8300 ± 600
$T_{e,\text{int.}}$ (K)	7300 ± 300	7700 ± 400	7700 ± 300	8200 ± 900	8500 ± 1000	8000 ± 400	8000 ± 800
$T_{e,\text{high}}$ (K)	8100 ± 800	8700 ± 300	9000 ± 400	8900 ± 1000	9100 ± 1000	8700 ± 900	8700 ± 1000
O^+/H^+ (10^5)	28.4 ± 5.7	19.8 ± 3.9	21.0 ± 3.7	11.9 ± 4.5	18.5 ± 7.2	21.8 ± 4.8	14.0 ± 5.1
O^{+2}/H^+ (10^5)	11.4 ± 4.9	8.4 ± 1.3	7.5 ± 1.3	2.8 ± 1.2	4.4 ± 1.9	12.4 ± 4.8	7.4 ± 3.2
$12 + \log(\text{O/H})$	8.60 ± 0.08	8.45 ± 0.06	8.45 ± 0.06	8.17 ± 0.12	8.36 ± 0.12	8.53 ± 0.08	8.33 ± 0.11
N^+/H^+ (10^6)	23.2 ± 4.0	18.0 ± 2.5	17.3 ± 2.5	20.7 ± 4.9	16.9 ± 3.9	20.3 ± 3.5	12.2 ± 2.8
N ICF	1.4 ± 0.4	1.4 ± 0.4	1.4 ± 0.3	1.2 ± 0.6	1.2 ± 0.6	1.6 ± 0.5	1.5 ± 0.7
$\log(\text{N/H})$	7.51 ± 0.12	7.41 ± 0.11	7.37 ± 0.10	7.41 ± 0.19	7.32 ± 0.19	7.50 ± 0.13	7.27 ± 0.18
$\log(\text{N/O})$	-1.09 ± 0.07	-1.04 ± 0.05	-1.08 ± 0.06	-0.76 ± 0.07	-1.04 ± 0.08	-1.03 ± 0.07	-1.06 ± 0.07
S^+/H^+ (10^7)	19.7 ± 1.9	13.8 ± 1.3	13.8 ± 1.2	25.0 ± 4.0	17.2 ± 2.9	18.6 ± 1.8	13.2 ± 2.1
S^{+2}/H^+ (10^7)	121.6 ± 16.0	77.4 ± 11.2	87.3 ± 9.7	46.0 ± 12.4	52.1 ± 14.2	100.3 ± 14.6	63.1 ± 16.4
S ICF	1.40 ± 0.39	1.43 ± 0.35	1.36 ± 0.30	1.24 ± 0.61	1.24 ± 0.62	1.57 ± 0.46	1.53 ± 0.71
$\log(\text{S/H})$	7.30 ± 0.11	7.11 ± 0.11	7.14 ± 0.09	6.94 ± 0.18	6.93 ± 0.19	7.27 ± 0.12	7.07 ± 0.18
$\log(\text{S/O})$	-1.30 ± 0.13	-1.34 ± 0.12	-1.32 ± 0.11	-1.23 ± 0.21	-1.43 ± 0.21	-1.26 ± 0.14	-1.26 ± 0.20
$\text{Ne}^{+2}/\text{H}^+$ (10^6)	10.8 ± 5.6	9.6 ± 1.7	8.9 ± 1.8	...	6.3 ± 3.6	16.9 ± 8.3	10.7 ± 5.6
Ne ICF	3.5 ± 1.6	3.3 ± 0.7	3.8 ± 0.8	...	5.2 ± 2.8	2.8 ± 1.2	2.9 ± 1.5
$\log(\text{Ne/H})$	7.58 ± 0.23	7.50 ± 0.10	7.53 ± 0.11	...	7.52 ± 0.25	7.67 ± 0.22	7.49 ± 0.24
$\log(\text{Ne/O})$	-1.02 ± 0.07	-0.95 ± 0.05	-0.93 ± 0.05	...	-0.84 ± 0.11	-0.87 ± 0.08	-0.84 ± 0.05
$\text{Ar}^{+2}/\text{H}^+$ (10^7)	19.4 ± 2.9	12.0 ± 2.0	13.5 ± 1.7	6.1 ± 1.9	7.8 ± 2.5	17.2 ± 2.9	11.1 ± 3.4
Ar ICF	1.19 ± 0.12	1.19 ± 0.12	1.20 ± 0.12	1.23 ± 0.12	1.23 ± 0.12	1.16 ± 0.12	1.17 ± 0.12
$\log(\text{Ar/H})$	6.36 ± 0.07	6.15 ± 0.08	6.21 ± 0.06	5.88 ± 0.12	5.98 ± 0.12	6.30 ± 0.08	6.11 ± 0.12
$\log(\text{Ar/O})$	-2.24 ± 0.10	-2.30 ± 0.09	-2.25 ± 0.08	-2.29 ± 0.16	-2.37 ± 0.17	-2.24 ± 0.11	-2.22 ± 0.15
Property	+119-28	-98-19	-59+118	+96+30	+44+82	+125-142	+166-140
$T_e[\text{SII}]$ (K)	10300 ± 1600	7300 ± 1000	9200 ± 900	10700 ± 600	9600 ± 600	11900 ± 1300	8600 ± 900
$T_e[\text{NII}]$ (K)	8900 ± 500	...	9200 ± 700	8900 ± 300	8600 ± 400	...	9100 ± 600
$T_e[\text{OII}]$ (K)	10000 ± 300	8400 ± 400	11000 ± 700	11300 ± 300	9400 ± 500	10500 ± 600	10500 ± 600
$T_e[\text{SIII}]$ (K)	9300 ± 300	7900 ± 900	8500 ± 500	8900 ± 300	8100 ± 200	7800 ± 300	7900 ± 300
$T_e[\text{O III}]$ (K)	8000 ± 500	...	7700 ± 300	8500 ± 200	8400 ± 300	8100 ± 300	9200 ± 300
n_e (cm^{-3})	90 ± 90	10 ± 60	20 ± 90	140 ± 100	30 ± 80	20 ± 130	50 ± 130
$T_{e,\text{low}}$ (K)	9000 ± 300	8200 ± 600	8600 ± 400	8900 ± 300	8400 ± 200	8100 ± 300	8500 ± 300
$T_{e,\text{int.}}$ (K)	9100 ± 300	7900 ± 900	8400 ± 500	8900 ± 300	8100 ± 200	7800 ± 300	8100 ± 300
$T_{e,\text{high}}$ (K)	8500 ± 500	8700 ± 1000	8000 ± 300	8600 ± 200	8500 ± 300	8100 ± 300	9100 ± 300
O^+/H^+ (10^5)	14.6 ± 2.2	22.5 ± 8.6	10.9 ± 2.4	14.9 ± 2.0	24.5 ± 3.9	19.1 ± 3.6	15.8 ± 2.6
O^{+2}/H^+ (10^5)	13.4 ± 3.2	1.7 ± 0.8	18.5 ± 3.6	13.6 ± 1.1	8.9 ± 1.4	18.7 ± 3.4	10.4 ± 1.5
$12 + \log(\text{O/H})$	8.45 ± 0.06	8.38 ± 0.13	8.47 ± 0.06	8.45 ± 0.03	8.52 ± 0.05	8.58 ± 0.05	8.42 ± 0.05
N^+/H^+ (10^6)	12.0 ± 1.2	20.7 ± 3.7	8.5 ± 1.3	10.6 ± 1.5	15.6 ± 2.7	9.2 ± 1.3	8.6 ± 1.0
N ICF	1.9 ± 0.4	1.1 ± 0.6	2.7 ± 0.7	1.9 ± 0.3	1.4 ± 0.3	2.0 ± 0.5	1.7 ± 0.3
$\log(\text{N/H})$	7.36 ± 0.09	7.35 ± 0.19	7.36 ± 0.11	7.31 ± 0.08	7.33 ± 0.10	7.26 ± 0.10	7.16 ± 0.09
$\log(\text{N/O})$	-1.09 ± 0.04	-1.04 ± 0.05	-1.11 ± 0.06	-1.14 ± 0.06	-1.19 ± 0.07	-1.32 ± 0.06	-1.26 ± 0.05
S^+/H^+ (10^7)	12.9 ± 1.0	28.8 ± 4.6	9.5 ± 1.0	11.8 ± 0.8	14.0 ± 1.1	11.9 ± 1.2	12.4 ± 1.1
S^{+2}/H^+ (10^7)	47.7 ± 4.4	45.0 ± 12.2	59.3 ± 8.8	53.6 ± 4.2	85.2 ± 8.3	95.9 ± 12.2	85.0 ± 9.2
S ICF	1.43 ± 0.14	1.08 ± 0.56	1.36 ± 0.14	1.43 ± 0.14	1.36 ± 0.27	1.42 ± 0.14	1.66 ± 0.34
$\log(\text{S/H})$	6.94 ± 0.05	6.90 ± 0.19	6.97 ± 0.07	6.97 ± 0.05	7.13 ± 0.09	7.18 ± 0.06	7.21 ± 0.09
$\log(\text{S/O})$	-1.51 ± 0.07	-1.48 ± 0.22	-1.50 ± 0.09	-1.48 ± 0.06	-1.39 ± 0.10	-1.39 ± 0.08	-1.21 ± 0.10

Table A2
(Continued)

Property	-14+42	-38+51	+7+37	+88-18	-97+39	-84-0	-3-71
$\text{Ne}^{+2}/\text{H}^+ (10^6)$	18.1 ± 5.2	...	23.7 ± 5.5	20.8 ± 2.1	7.1 ± 1.3	33.3 ± 6.8	18.3 ± 2.9
Ne ICF	2.1 ± 0.6	...	1.6 ± 0.4	2.1 ± 0.2	3.8 ± 0.8	2.0 ± 0.5	2.5 ± 0.5
$\log(\text{Ne}/\text{H})$	7.58 ± 0.15	...	7.58 ± 0.13	7.64 ± 0.06	7.43 ± 0.10	7.83 ± 0.12	7.66 ± 0.10
$\log(\text{Ne}/\text{O})$	-0.87 ± 0.04	...	-0.89 ± 0.05	-0.82 ± 0.02	-1.10 ± 0.05	-0.75 ± 0.05	-0.76 ± 0.05
$\text{Ar}^{+2}/\text{H}^+ (10^7)$	10.8 ± 1.1	5.1 ± 1.6	11.7 ± 2.0	10.2 ± 0.9	12.9 ± 1.4	15.3 ± 2.2	13.0 ± 1.6
Ar ICF	1.11 ± 0.11	1.29 ± 0.13	1.07 ± 0.11	1.11 ± 0.11	1.20 ± 0.12	1.11 ± 0.11	1.14 ± 0.11
$\log(\text{Ar}/\text{H})$	6.08 ± 0.06	5.82 ± 0.12	6.10 ± 0.08	6.05 ± 0.05	6.19 ± 0.06	6.23 ± 0.07	6.17 ± 0.06
$\log(\text{Ar}/\text{O})$	-2.37 ± 0.08	-2.57 ± 0.17	-2.37 ± 0.09	-2.40 ± 0.06	-2.33 ± 0.08	-2.35 ± 0.09	-2.25 ± 0.08
Property	-190+116	+174-24	-99-59	-196+58	-194+165	-89+171	-146-38
$T_e[\text{SII}] (\text{K})$	9200 ± 800	10400 ± 900	8400 ± 400	9400 ± 600	...	10800 ± 1500	8800 ± 1500
$T_e[\text{NII}] (\text{K})$	8900 ± 500	8900 ± 1000	8600 ± 500	8400 ± 400	7900 ± 800
$T_e[\text{OII}] (\text{K})$	10600 ± 300	10200 ± 400	9900 ± 400	10000 ± 300	11400 ± 700	9200 ± 400	8700 ± 400
$T_e[\text{SIII}] (\text{K})$	9300 ± 300	7900 ± 400	8700 ± 300	8800 ± 300	8900 ± 500	9000 ± 400	9100 ± 1000
$T_e[\text{O III}] (\text{K})$	8300 ± 200	8900 ± 200	8900 ± 500	8200 ± 200
$n_e (\text{cm}^{-3})$	70 ± 70	40 ± 60	40 ± 60	50 ± 60	70 ± 70	30 ± 80	...
$T_{e,\text{low}} (\text{K})$	9000 ± 300	8300 ± 300	8700 ± 300	8700 ± 200	8900 ± 400	9000 ± 300	8500 ± 700
$T_{e,\text{int.}} (\text{K})$	9200 ± 300	8000 ± 400	8700 ± 300	8700 ± 300	8900 ± 500	9000 ± 400	8300 ± 1000
$T_{e,\text{high}} (\text{K})$	8500 ± 200	8900 ± 200	9000 ± 500	8300 ± 200	9300 ± 900	9400 ± 800	8800 ± 1000
$\text{O}^+/\text{H}^+ (10^5)$	10.6 ± 1.5	18.2 ± 3.6	22.2 ± 3.6	13.3 ± 1.9	13.3 ± 2.7	12.3 ± 2.2	20.7 ± 8.8
$\text{O}^{+2}/\text{H}^+ (10^5)$	16.3 ± 1.9	15.3 ± 1.7	9.0 ± 2.0	15.3 ± 1.6	7.2 ± 2.5	9.1 ± 3.0	2.4 ± 1.1
$12 + \log(\text{O}/\text{H})$	8.43 ± 0.04	8.53 ± 0.05	8.49 ± 0.05	8.46 ± 0.04	8.31 ± 0.07	8.33 ± 0.07	8.36 ± 0.14
$\text{N}^+/\text{H}^+ (10^6)$	7.9 ± 1.4	8.5 ± 1.1	14.6 ± 1.4	9.6 ± 1.1	10.7 ± 2.0	8.4 ± 1.0	16.4 ± 3.2
N ICF	2.5 ± 0.4	1.8 ± 0.4	1.4 ± 0.3	2.2 ± 0.4	1.5 ± 0.4	1.7 ± 0.4	1.1 ± 0.6
$\log(\text{N}/\text{H})$	7.30 ± 0.09	7.19 ± 0.10	7.31 ± 0.09	7.32 ± 0.08	7.22 ± 0.12	7.16 ± 0.11	7.26 ± 0.21
$\log(\text{N}/\text{O})$	-1.12 ± 0.07	-1.33 ± 0.04	-1.18 ± 0.04	-1.14 ± 0.04	-1.09 ± 0.07	-1.17 ± 0.05	-1.07 ± 0.06
$\text{S}^+/\text{H}^+ (10^7)$	7.4 ± 0.5	11.6 ± 1.0	21.1 ± 1.5	9.5 ± 0.7	11.5 ± 1.1	9.8 ± 0.8	15.8 ± 2.8
$\text{S}^{+2}/\text{H}^+ (10^7)$	43.1 ± 3.5	88.1 ± 11.4	58.1 ± 5.7	49.7 ± 4.0	50.2 ± 6.8	41.8 ± 5.0	34.7 ± 10.2
S ICF	1.36 ± 0.14	1.45 ± 0.15	1.41 ± 0.29	1.39 ± 0.14	1.54 ± 0.42	1.49 ± 0.15	1.12 ± 0.64
$\log(\text{S}/\text{H})$	6.84 ± 0.05	7.16 ± 0.06	7.05 ± 0.09	6.92 ± 0.05	6.98 ± 0.11	6.89 ± 0.06	6.75 ± 0.21
$\log(\text{S}/\text{O})$	-1.59 ± 0.06	-1.36 ± 0.08	-1.45 ± 0.10	-1.54 ± 0.06	-1.33 ± 0.13	-1.44 ± 0.09	-1.61 ± 0.24
$\text{Ne}^{+2}/\text{H}^+ (10^6)$	23.0 ± 3.2	29.5 ± 3.8	13.1 ± 3.5	19.3 ± 2.5	5.7 ± 2.5	12.7 ± 5.1	2.8 ± 1.8
Ne ICF	1.7 ± 0.2	2.2 ± 0.4	3.5 ± 0.9	1.9 ± 0.3	2.8 ± 1.1	2.3 ± 0.9	9.7 ± 5.7
$\log(\text{Ne}/\text{H})$	7.58 ± 0.08	7.81 ± 0.08	7.66 ± 0.14	7.56 ± 0.07	7.21 ± 0.20	7.47 ± 0.19	7.43 ± 0.27
$\log(\text{Ne}/\text{O})$	-0.85 ± 0.02	-0.72 ± 0.03	-0.84 ± 0.04	-0.90 ± 0.03	-1.10 ± 0.07	-0.85 ± 0.05	-0.93 ± 0.13
$\text{Ar}^{+2}/\text{H}^+ (10^7)$	9.4 ± 0.9	14.9 ± 2.2	10.9 ± 1.2	10.2 ± 0.9	9.2 ± 1.4	9.3 ± 1.2	5.0 ± 1.7
Ar ICF	1.07 ± 0.11	1.12 ± 0.11	1.19 ± 0.12	1.09 ± 0.11	1.16 ± 0.12	1.13 ± 0.11	1.27 ± 0.13
$\log(\text{Ar}/\text{H})$	6.00 ± 0.06	6.22 ± 0.07	6.11 ± 0.06	6.05 ± 0.06	6.03 ± 0.07	6.02 ± 0.07	5.80 ± 0.13
$\log(\text{Ar}/\text{O})$	-2.43 ± 0.07	-2.30 ± 0.08	-2.38 ± 0.08	-2.41 ± 0.06	-2.28 ± 0.10	-2.31 ± 0.09	-2.56 ± 0.18
Property	+178-210	-22-162	+92-210	+43-200	-14+192	+160-251	-18+224
$T_e[\text{SII}] (\text{K})$	11500 ± 1600	10400 ± 1100	8900 ± 600	12500 ± 3500	11300 ± 800	11800 ± 1100	11300 ± 1200
$T_e[\text{NII}] (\text{K})$...	9700 ± 1300	9900 ± 1000	...	9600 ± 800	9800 ± 1300	10400 ± 1100
$T_e[\text{OII}] (\text{K})$	12100 ± 900	9300 ± 300	10400 ± 600	9100 ± 600	10600 ± 400	10900 ± 600	10100 ± 300
$T_e[\text{SIII}] (\text{K})$	8200 ± 400	10100 ± 600	9300 ± 800	9800 ± 800	10300 ± 300	9000 ± 400	10900 ± 700
$T_e[\text{O III}] (\text{K})$	8700 ± 500	9400 ± 700	...	9700 ± 800	9700 ± 300	10800 ± 400	9800 ± 300
$n_e (\text{cm}^{-3})$	60 ± 90	50 ± 80	40 ± 80	30 ± 100	30 ± 60	30 ± 90	20 ± 50
$T_{e,\text{low}} (\text{K})$	8400 ± 300	9600 ± 500	9400 ± 600	9500 ± 600	9700 ± 300	9200 ± 300	10000 ± 500
$T_{e,\text{int.}} (\text{K})$	8200 ± 400	10000 ± 600	9600 ± 800	9800 ± 800	10200 ± 300	9200 ± 400	10600 ± 700
$T_{e,\text{high}} (\text{K})$	8700 ± 500	9700 ± 700	9800 ± 1000	9800 ± 800	9700 ± 300	10500 ± 400	9900 ± 300
$\text{O}^+/\text{H}^+ (10^5)$	16.4 ± 3.2	16.0 ± 3.5	14.8 ± 4.2	13.9 ± 4.0	11.7 ± 1.6	15.2 ± 2.6	9.5 ± 2.0
$\text{O}^{+2}/\text{H}^+ (10^5)$	12.8 ± 2.8	7.2 ± 1.7	4.2 ± 1.5	8.5 ± 2.6	10.6 ± 1.1	9.6 ± 1.5	11.0 ± 1.4

Table A2
(Continued)

Property	-190+116	+174-24	-99-59	-196+58	-194+165	-89+171	-146-38
12 + log(O/H)	8.47 \pm 0.06	8.37 \pm 0.07	8.28 \pm 0.09	8.35 \pm 0.08	8.35 \pm 0.04	8.40 \pm 0.05	8.31 \pm 0.05
N ⁺ /H ⁺ (10 ⁶)	6.7 \pm 1.2	9.2 \pm 1.3	8.9 \pm 1.6	6.3 \pm 1.2	5.9 \pm 0.6	5.3 \pm 0.9	4.3 \pm 0.6
N ICF	1.8 \pm 0.4	1.4 \pm 0.4	1.3 \pm 0.5	1.6 \pm 0.6	1.9 \pm 0.3	1.6 \pm 0.3	2.2 \pm 0.5
log(N/H)	7.08 \pm 0.12	7.12 \pm 0.12	7.06 \pm 0.15	7.01 \pm 0.15	7.05 \pm 0.07	6.94 \pm 0.10	6.97 \pm 0.11
log(N/O)	-1.39 \pm 0.08	-1.24 \pm 0.05	-1.22 \pm 0.06	-1.34 \pm 0.06	-1.30 \pm 0.04	-1.46 \pm 0.07	-1.34 \pm 0.04
S ⁺ /H ⁺ (10 ⁷)	8.8 \pm 0.8	16.1 \pm 1.6	24.9 \pm 3.1	9.3 \pm 1.2	9.4 \pm 0.6	10.8 \pm 0.9	8.5 \pm 0.8
S ⁺² /H ⁺ (10 ⁷)	69.6 \pm 9.0	34.9 \pm 5.0	30.9 \pm 5.9	37.5 \pm 7.2	31.8 \pm 2.6	56.7 \pm 6.2	24.5 \pm 3.3
S ICF	1.48 \pm 0.15	1.45 \pm 0.40	1.29 \pm 0.48	1.61 \pm 0.58	1.43 \pm 0.14	1.63 \pm 0.34	1.39 \pm 0.14
log(S/H)	7.06 \pm 0.06	6.87 \pm 0.11	6.86 \pm 0.14	6.88 \pm 0.14	6.77 \pm 0.05	7.04 \pm 0.09	6.66 \pm 0.06
log(S/O)	-1.40 \pm 0.08	-1.50 \pm 0.13	-1.42 \pm 0.16	-1.47 \pm 0.16	-1.58 \pm 0.06	-1.35 \pm 0.10	-1.65 \pm 0.08
Ne ⁺² /H ⁺ (10 ⁶)	20.8 \pm 5.3	16.4 \pm 4.8	6.3 \pm 2.6	14.9 \pm 5.5	19.5 \pm 2.3	20.8 \pm 3.6	22.9 \pm 3.5
Ne ICF	2.3 \pm 0.6	3.2 \pm 1.0	4.5 \pm 1.9	2.6 \pm 1.0	2.1 \pm 0.3	2.6 \pm 0.5	1.9 \pm 0.3
log(Ne/H)	7.68 \pm 0.14	7.72 \pm 0.15	7.45 \pm 0.20	7.60 \pm 0.18	7.61 \pm 0.07	7.73 \pm 0.10	7.63 \pm 0.09
log(Ne/O)	-0.79 \pm 0.05	-0.64 \pm 0.04	-0.83 \pm 0.05	-0.75 \pm 0.06	-0.74 \pm 0.03	-0.67 \pm 0.05	-0.68 \pm 0.03
Ar ⁺² /H ⁺ (10 ⁷)	12.0 \pm 1.8	6.5 \pm 1.1	4.8 \pm 1.1	7.7 \pm 1.7	6.3 \pm 0.6	8.7 \pm 1.0	5.6 \pm 0.9
Ar ICF	1.13 \pm 0.11	1.18 \pm 0.12	1.22 \pm 0.12	1.15 \pm 0.12	1.11 \pm 0.11	1.15 \pm 0.11	1.09 \pm 0.11
log(Ar/H)	6.13 \pm 0.07	5.89 \pm 0.08	5.77 \pm 0.09	5.95 \pm 0.09	5.85 \pm 0.06	6.00 \pm 0.06	5.79 \pm 0.07
log(Ar/O)	-2.34 \pm 0.09	-2.48 \pm 0.10	-2.51 \pm 0.13	-2.40 \pm 0.12	-2.50 \pm 0.06	-2.39 \pm 0.08	-2.52 \pm 0.09

Note. Electron temperatures and ionic abundances in the H II regions of NGC 2403. All regions contain at least one detection of the [N II], [S III], or [O III] auroral lines. The temperatures in each ionization zone are calculated using the weighted average of the available direct temperatures and the T_e – T_e relations of Section 3.2.

Appendix B Ionization-based and Weighted-average Temperature Prioritizations

Berg et al. (2020) use ionization-based temperature prioritizations to determine the electron temperature in an ionization zone. These prioritizations are constructed to make use of electron temperatures from dominant ionization zones within a H II region. Here, we compare the ionization-based temperature prioritizations to the weighted-average temperatures within the ionization zones described in Section 4.

The temperatures prioritized in the ionization-based approach are dependent on the $O_{32} = \frac{I(5007)}{I(3727)}$ parameter within a region. The schematic for the ionization-based prioritizations is provided in Figure B1, where the equations are the T_e – T_e relations discussed in Section 3.2 (this figure has been modified from Figure 5 in Berg et al. 2020). The low-ionization prioritizations are the same for a region with high or low average ionization. A direct [S III] temperature is prioritized in the intermediate-ionization zone when available, independent of the average ionization. If [S III] $\lambda 6312$ is not detected, then the temperature from either [O III] or [N II] is used, depending on the ionization of the region.

However, there are substantial differences in the prioritization of electron temperatures for the high-ionization zone. In H II regions characterized by high average ionization, the direct temperature from [O III] is used because the detection is coming from an ionization zone that is dominant in the region. If the low-ionization zone is dominant, then a direct [O III] temperature is deprioritized in favor of a [S III] or [N II] temperature. There are two potential issues with this approach that can manifest as discrepancies in the abundances. First, the updated T_e – T_e relations now include larger uncertainties (see Equation (8)). In a region characterized by low ionization emission, applying the T_e [O III]– T_e [S III] relation instead of

Ionization-Based Temperature Priorities:			
Criteria:	Ionization Zone:		
	Low	Intermediate	High
If $O_{32} > 1.25$	1. T_e [N II]	1. T_e [S III]	1. T_e [O III]
	2. T_e [S III] + Eqn. 3	2. T_e [O III] + Eqn. 4	2. T_e [S III] + Eqn. 5
	3. T_e [O III] + Eqn. 6	3. T_e [N II] + Eqn. 2	3. T_e [N II] + Eqn. 7
If $O_{32} < 1.25$	1. T_e [N II]	1. T_e [S III]	1. T_e [S III] + Eqn. 5
	2. T_e [S III] + Eqn. 3	2. T_e [N II] + Eqn. 2	2. T_e [N II] + Eqn. 7
	3. T_e [O III] + Eqn. 6	3. T_e [O III] + Eqn. 4	3. T_e [O III]

Figure B1. The ionization-based temperature prioritizations adopted by Berg et al. (2020) and updated to include the equations listed in Section 3.2. This designates which temperatures are to be used first (if available) for each ionization zone. The O_{32} value used to decide if the temperatures are calculated for a high- or low-ionization region is 1.25. This figure is modified from Figure 5 in Berg et al. (2020).

using the direct [O III] temperature will set the minimum uncertainty on the inferred temperature to be ~ 800 K. Such an increase in the uncertainty will result in an abundance with high uncertainty, which will deweight that region in abundance gradient determinations. The second issue is that this prioritization arrangement can reject high S/N [O III] $\lambda 4363$ measurements in favor of more uncertain [S III] or [N II] detections. Not only will the choice of poorly measured lines further affect the uncertainties on the resulting abundances, but it could result in large, nonphysical scatter in the abundances.

The possible shortcomings of the ionization-based prioritizations necessitate a comparison to other temperature prioritizations. The weighted-average approach in each ionization zone utilizes the complete temperature information within a H II region. Unlike the ionization-based prioritization, this method is not as susceptible to low-S/N detections unless there is a single temperature-sensitive auroral line detected in the region. Alternatively, a weighted average can be biased to the strongest auroral line detection and relies on the accuracy of the T_e – T_e relations applied.

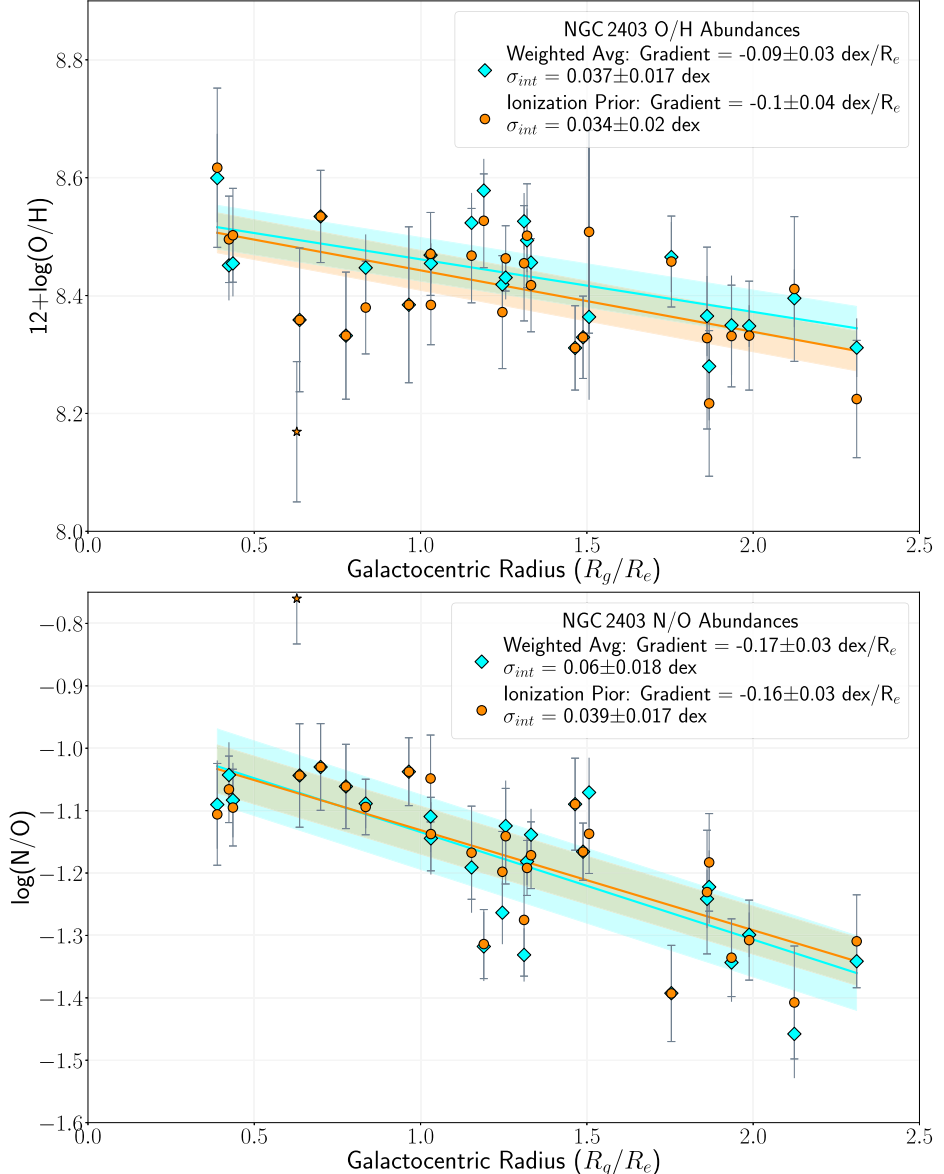


Figure B2. Top panel: CHAOS oxygen abundances in NGC 2403 plotted vs. R_g/R_e . Cyan diamonds are abundances obtained using the weighted-average ionization zone temperatures, while orange circles are the same H II regions using the ionization-based temperature prioritizations of Figure B1. The capped error bars are the errors on the abundances resulting from the ionization-based method. The gradients and intrinsic dispersions are shown in the legend of the plot. The intrinsic dispersions about each gradient are represented as the shaded region around the gradients. Bottom panel: same as the top panel but with N/O abundances.

Table B1
Ionization-based Temperature Prioritization Abundance Fits

y	x	Galaxy	# Reg.	Equation	$\sigma_{int.}$	$\sigma_{tot.}$
$12 + \log(\text{O/H})$ (dex)	$R_g (R_e^{-1})$	NGC 0628	45	$y = (8.62 \pm 0.05) - (0.08 \pm 0.03) \times x$	0.091 ± 0.018	0.111
		NGC 5194	28	$y = (8.59 \pm 0.10) - (0.02 \pm 0.05) \times x$	0.05 ± 0.03	0.08
		NGC 5457	71	$y = (8.71 \pm 0.04) - (0.179 \pm 0.017) \times x$	0.087 ± 0.013	0.108
		NGC 3184	30	$y = (8.57 \pm 0.17) - (0.09 \pm 0.12) \times x$	0.08 ± 0.04	0.14
		NGC 2403	27	$y = (8.55 \pm 0.05) - (0.10 \pm 0.04) \times x$	0.03 ± 0.02	0.069
$\log(\text{N/O})$ (dex)	$R_g (R_e^{-1})$	NGC 0628	45	$y = (-0.48 \pm 0.04) - (0.29 \pm 0.02) \times x$	0.076 ± 0.011	0.081
		NGC 5194	28	$y = (-0.31 \pm 0.06) - (0.14 \pm 0.03) \times x$	0.075 ± 0.016	0.079
		NGC 5457	71	$y = (-0.72 \pm 0.03) - (0.186 \pm 0.016) \times x$	0.100 ± 0.012	0.112
		NGC 3184	30	$y = (-0.32 \pm 0.09) - (0.36 \pm 0.06) \times x$	0.059 ± 0.019	0.081
		NGC 2403	27	$y = (-0.97 \pm 0.04) - (0.16 \pm 0.03) \times x$	0.039 ± 0.017	0.066

Note. Best-fit equations for the O/H and N/O abundance gradients observed in the CHAOS galaxies when using ionization-based temperature prioritizations. The first and second columns are the dependent and independent variables, respectively, used for the Equation listed in the fifth column. The galaxy and the number of regions used for the fit are given in the third and fourth columns. The intrinsic and total scatter, both in dex, are listed in the sixth and seventh columns, respectively.

Table B2
Difference between the Weighted-average and Ionization-based Temperature Prioritization Gradient Parameters

Galaxy	Δ Central O/H	Δ Gradient O/H	$\Delta\sigma_{\text{int}}$ around O/H	$\Delta\sigma_{\text{tot}}$ around O/H
NGC 0628	0.02 ± 0.07	-0.00 ± 0.04	-0.01 ± 0.02	-0.012
NGC 5194	-0.11 ± 0.14	0.04 ± 0.07	-0.01 ± 0.03	-0.014
NGC 5457	-0.02 ± 0.05	0.01 ± 0.02	0.010 ± 0.018	0.005
NGC 3184	0.1 ± 0.2	-0.05 ± 0.16	0.01 ± 0.05	-0.023
NGC 2403	0.00 ± 0.06	0.01 ± 0.05	0.01 ± 0.03	-0.006
Galaxy	Δ Central N/O	Δ Gradient N/O	$\Delta\sigma_{\text{int}}$ around N/O	$\Delta\sigma_{\text{tot}}$ around N/O
NGC 0628	-0.01 ± 0.05	0.00 ± 0.03	-0.004 ± 0.015	-0.006
NGC 5194	0.03 ± 0.09	-0.01 ± 0.05	-0.003 ± 0.019	-0.004
NGC 5457	0.02 ± 0.05	-0.01 ± 0.02	0.010 ± 0.017	0.008
NGC 3184	-0.02 ± 0.12	0.01 ± 0.08	0.00 ± 0.03	-0.005
NGC 2403	0.01 ± 0.06	-0.01 ± 0.04	0.021 ± 0.025	0.009

Note. The difference between the best-fit parameters provided in Table 3 for the weighted-average temperature prioritizations and in Table B1 for the ionization-based temperature prioritizations. The name of the galaxy is given in the first column, the second column provides the difference in the central abundance values, the third provides the difference between the gradients, and the difference between the intrinsic and total dispersion about the gradient are provided in the fourth and fifth columns, respectively. All units are in dex. The first five rows provide the differences between the oxygen abundance gradients, while the last five rows are the differences between the N/O gradients.

Figure B2 plots the O/H and N/O abundances measured in the H II regions of NGC 2403 versus R_g/R_e when using the weighted-average method (cyan diamonds) and ionization-based prioritizations (orange circles) described in Figure B1. Additionally, the best-fit parameters for the O/H and N/O gradients in all CHAOS galaxies when using the ionization-based prioritizations are provided in Table B1. All but three H II regions in NGC 2403 have $O_{32} < 1.25$, so the majority of the regions have $T_e[\text{O III}]$ deprioritized in the high-ionization zone. From the O/H abundances, one can see that the uncertainties are significantly larger when using the ionization-based method due to the use of $T_e - T_e$ relations to infer the high-ionization zone temperature. There are instances where only one auroral line is detected, in which case the O/H abundances and uncertainties as calculated by the ionization prioritization and the weighted-average methods are the same. That being said, the oxygen abundances as calculated by the two different methods are consistent within each H II region in NGC 2403.

Table B2 provides the difference between the best-fit parameters obtained via the weighted-average approach (from Table 3) and the parameters from the ionization-based method (from Table B1). The differences are all consistent with zero within statistical uncertainty, including the intrinsic dispersions about the gradients. The reason for this is a combination of two factors. First, while the temperatures obtained via the ionization-based prioritizations are prone to the issues discussed above, these temperatures also have large uncertainties. The large uncertainties on the resulting abundances yield intrinsic dispersions about the gradient that are generally smaller. The second factor is the small oxygen abundance uncertainty produced by the weighted-average approach. Even if the total scatter is smaller about the gradient (see the difference in σ_{tot} in Table B2), the reduced uncertainties result in more of the scatter being attributed to intrinsic variations rather than observational uncertainties. Given the agreement between the two methods, we conclude that the weighted-average approach is at least consistent with the approach used in Berg et al. (2020) and could be used as an alternative approach to determining the electron temperature within each ionization zone.

ORCID iDs

Noah S. J. Rogers <https://orcid.org/0000-0002-0361-8223>
 Evan D. Skillman <https://orcid.org/0000-0003-0605-8732>
 Richard W. Pogge <https://orcid.org/0000-0003-1435-3053>
 Danielle A. Berg <https://orcid.org/0000-0002-4153-053X>
 John Moustakas <https://orcid.org/0000-0002-2733-4559>
 Kevin V. Croxall <https://orcid.org/0000-0002-5258-7224>
 Jiayi Sun <https://orcid.org/0000-0003-0378-4667>

References

Andrews, B. H., & Martini, P. 2013, *ApJ*, **765**, 140
 Arellano-Córdova, K. Z., & Rodríguez, M. 2020, *MNRAS*, **497**, 672
 Arellano-Córdova, K. Z., Rodríguez, M., Mayya, Y. D., et al. 2016, *MNRAS*, **455**, 2627
 Asplund, M., Grevesse, N., Sauval, A. J., et al. 2009, *ARA&A*, **47**, 481
 Aver, E., Berg, D. A., Olive, K. A., et al. 2021, *JCAP*, **2021**, 027
 Aver, E., Olive, K. A., & Skillman, E. D. 2011, *JCAP*, **1103**, 043
 Bedregal, A. G., Aragón-Salamanca, A., & Merrifield, A. R. 2006, *MNRAS*, **373**, 1125
 Berg, D. A., Croxall, K. V., Skillman, E. D., et al. 2015, *ApJ*, **806**, 16
 Berg, D. A., Pogge, R. W., Skillman, E. D., et al. 2020, *ApJ*, **893**, 96b
 Berg, D. A., Skillman, E. D., Garnett, D. R., et al. 2013, *ApJ*, **775**, 128
 Bohlin, R. C., Gordon, K. D., & Tremblay, P. E. 2014, *PASP*, **126**, 711
 Bresolin, F. 2007, *ApJ*, **656**, 186
 Brown, J. S., Martini, P., & Andrews, B. H. 2016, *MNRAS*, **458**, 1529
 Bruzual, G., & Charlot, S. 2003, *MNRAS*, **344**, 1000
 Campbell, A., Terlevich, R., & Melnick, J. 1986, *MNRAS*, **223**, 811
 Cardelli, J. A., Clayton, G. C., & Mathis, J. S. 1989, *ApJ*, **345**, 245
 Cid Fernandes, R., Mateus, A., Sodré, L., et al. 2005, *MNRAS*, **358**, 363
 Crockett, N. R., Garnett, D. R., Massey, P., et al. 2006, *ApJ*, **637**, 741
 Croxall, K. V., Pogge, R. W., Berg, D. A., Skillman, E. D., & Moustakas, J. 2015, *ApJ*, **808**, 42
 Croxall, K. V., Pogge, R. W., Berg, D. A., Skillman, E. D., & Moustakas, J. 2016, *ApJ*, **830**, 4
 Curti, M., Cresci, G., Mannucci, F., et al. 2017, *MNRAS*, **465**, 1384
 de Blok, W. J. G., Walter, F., Brinks, E., et al. 2008, *AJ*, **136**, 2648
 De Robertis, M. M., Dufour, R. J., & Hunt, R. W. 1987, *JRASC*, **81**, 195
 Dinerstein, H. L. 1990, in *The Interstellar Medium in Galaxies*, ed. H. A. Thronson, Jr. & J. M. Shull (Dordrecht: Kluwer), 257
 Eldridge, J. J., & Stanway, E. R. 2009, *MNRAS*, **400**, 1019
 Eldridge, J. J., Stanway, E. R., Xiao, L., et al. 2017, *PASA*, **334**, e058
 Esteban, C., Bresolin, F., García-Rojas, J., et al. 2020, *MNRAS*, **491**, 2137
 Esteban, C., Bresolin, F., Peimbert, M., et al. 2009, *ApJ*, **700**, 654
 Filippenko, A. V. 1982, *PASP*, **94**, 715
 García-Rojas, J., Peña, M., Morisset, C., et al. 2013, *A&A*, **558**, A122
 Garnett, D. R. 1992, *AJ*, **103**, 1330

Garnett, D. R., Shields, G. A., Skillman, E. D., et al. 1997, *ApJ*, **489**, 63

Henry, R. B. C., Edmunds, M. G., & Köppen, J. 2000, *ApJ*, **541**, 660

Hill, J. M. 2010, *ApOpt*, **49**, D115

Ho, I.-T., Kreckel, K., Meidt, S. E., et al. 2019, *ApJL*, **885**, L31

Izotov, Y. I., Stasińska, G., Meynet, M., Guseva, N. G., & Thuan, T. X. 2006, *A&A*, **448**, 996

Jenkins, C. R. 1987, *MNRAS*, **226**, 341

Kelly, B. C. 2007, *ApJ*, **665**, 1489

Kendall, S., Kennicutt, R. C., & Clarke, C. 2011, *MNRAS*, **414**, 538

Kennicutt, R. C., Armus, L., Bendo, G., et al. 2003a, *PASP*, **115**, 928

Kennicutt, R. C., Bresolin, F., & Garnett, D. R. 2003b, *ApJ*, **591**, 801

Kewley, L. J., & Dopita, M. A. 2002, *ApJS*, **142**, 35

Kewley, L. J., & Ellison, S. L. 2008, *ApJ*, **681**, 1183

Kobulnicky, H. A., Kennicutt, R. C., & Pizango, J. L. 1999, *ApJ*, **514**, 544

Kreckel, K., Ho, I.-T., Blanc, G. A., et al. 2019, *ApJ*, **887**, 80

Lequeux, J., Peimbert, M., Rayo, J. F., et al. 1979, *A&A*, **80**, 155

Leroy, A. K., Sandstrom, K. M., Lang, D., et al. 2019, *ApJS*, **244**, 24

Liang, Y. C., Hammer, F., Yin, Y. S., et al. 2007, *A&A*, **473**, 411

Liu, X.-W., Luo, S.-G., Barlow, M. J., et al. 2001, *MNRAS*, **327**, 121

López-Sánchez, Á R., Dopita, M. A., Kelwey, L. J., et al. 2012, *MNRAS*, **426**, 2630

López-Sánchez, Á R., & Esteban, C. 2010, *A&A*, **516**, A104

Luridiana, V., Morisset, C., & Shaw, R. A. 2012, in IAU Symp. 283, Planetary Nebulae: An Eye to the Future (Cambridge: Cambridge Univ. Press), 422

Luridiana, V., Morisset, C., & Shaw, R. A. 2015, *A&A*, **573**, A42

Mao, Y.-W., Lin, L., & Kong, X. 2018, *ApJ*, **853**, 151

Marino, R. A., Rosales-Ortega, F. F., Sánchez, S. F., et al. 2013, *A&A*, **559**, A114

McGaugh, S. S. 1991, *ApJ*, **380**, 140

Moustakas, J., Kennicutt, R. C., Tremonti, C. A., et al. 2010, *ApJS*, **190**, 233

Nava, A., Casebeer, D., Henry, R. B. C., et al. 2006, *ApJ*, **645**, 1076

Nicholls, D. C., Dopita, M. A., Sutherland, R. S., et al. 2014, *ApJ*, **786**, 155

Oke, J. B. 1990, *AJ*, **99**, 1621

Olive, K. A., & Skillman, E. D. 2001, *NewA*, **6**, 119

Pagel, B. E. J., Edmunds, M. G., Blackwell, D. E., et al. 1979, *MNRAS*, **189**, 95

Pagel, B. E. J., Simonson, E. A., Terlevich, R. J., et al. 1992, *MNRAS*, **255**, 325

Peimbert, A., & Peimbert, M. 2010, *ApJ*, **724**, 791

Peimbert, M., & Costero, R. 1969, *BOTT*, **5**, 3

Peña-Guerrero, M. A., Peimbert, A., & Peimbert, M. 2012, *ApJL*, **756**, L14

Pettini, M., & Pagel, B. E. J. 2004, *MNRAS*, **348**, L59

Pilyugin, L. S., & Grebel, E. K. 2016, *MNRAS*, **457**, 3678

Pilyugin, L. S., Mattsson, L., Vilchez, J. M., et al. 2009, *MNRAS*, **398**, 485

Pogge, R. W., Atwood, B., Brewer, D. F., et al. 2010, *Proc. SPIE*, **7735**, 77350A

Rosolowsky, E., & Simon, J. D. 2008, *ApJ*, **675**, 1213

Roy, J.-R., & Kunth, D. 1995, *A&A*, **294**, 432

Rubin, R. H. 1986, *ApJ*, **309**, 334

Sánchez, S. F., Rosales-Ortega, F. F., Iglesias-Páramo, J., et al. 2014, *A&A*, **563**, A49

Sánchez-Menguiano, L., Sánchez, S. F., Pérez, I., et al. 2016, *A&A*, **587**, A70

Sánchez-Menguiano, L., Sánchez, S. F., Pérez, I., et al. 2018, *A&A*, **609**, A119

Sánchez-Menguiano, L., Sánchez, S. F., Pérez, I., et al. 2020, *MNRAS*, **492**, 4149

Sandstrom, K. M., Leroy, A. K., Walter, F., et al. 2013, *ApJ*, **777**, 5

Skillman, E. D., Berg, D. A., Pogge, R. W., et al. 2020, *ApJ*, **894**, 138

Skillman, E. D., Côté, S., & Miller, B. M. 2003, *AJ*, **125**, 610

Stasińska, G. 1990, *A&AS*, **83**, 501S

Storey, P. J., & Hummer, D. G. 1995, *MNRAS*, **272**, 41

Thuan, T. X., Izotov, Y. I., & Lipovetsky, V. A. 1995, *ApJ*, **445**, 108

Torres-Peimbert, S., & Peimbert, M. 1977, *RMxAA*, **2**, 181

Tremonti, C. A., Heckman, T. M., Kauffmann, G., et al. 2004, *ApJ*, **613**, 898

Tully, R. B., Courtois, H. M., Dolphin, A. E., et al. 2013, *AJ*, **146**, 86

Yates, R. M., Schady, P., Chen, T.-W., et al. 2020, *A&A*, **634**, A107